SAPIENZA
UNIVERSITÀ DI ROMA

FACOLTÀ DI SCIENZE MATEMATICHE, FISICHE E NATURALI
Corso di Laurea in Fisica

PROBING ECLIPSE MECHANISMS IN BLACK WIDOW PULSARS AND REDBACKS: DEVELOPMENT OF A CODE AND ITS APPLICATIONS

Tesi di Laurea Magistrale

Advisor:
Prof. Valeria Ferrari

Student:
Alessandro Ridolfi

Supervisor:
Dott. Andrea Possenti

Academic Year 2011/2012

Contents

Introduction

Pulsars are fast spinning, highly magnetized neutron stars which are commonly visible in the radio band of the electromagnetic spectrum. Over the decades after their discovery, the number of different phenomenological features of these objects have been constantly increasing, naturally leading to a more and more diversified classification.

In particular, two main classes of pulsars are nowadays recognized. The first is that of the so-called *ordinary pulsars*, relatively young objects (aged $\sim 10^7$ yr) which exhibit spin periods of the order of a second as well as strong magnetic fields of $\sim 10^{12}$ G. To the second class belong the so-called *millisecond* (or *recycled*) *pulsars*, older sources (the typical age is $\sim 10^9$ yr), whose spin periods are of the order of milliseconds and which show weaker magnetic fields of $\sim 10^8$ G; most importantly, such pulsars are very often found in binary systems, suggesting a different evolutionary path with respect to the previous class. In fact, astronomers now agree in considering recycled pulsars as being spun up by the transfer of mass and angular momentum from the companion star of the binary system.

Among the various sub-categories of recycled pulsars, one has recently experienced a major re-flourishing of interest, both on theoretical and observational grounds: it is the class of the *eclipsing binary millisecond pulsars*. The sources that belong to this class are systems in which the pulsed radio signal released by the neutron star undergoes substantial modifications, or even completely disappears, periodically, at some particular orbital phases.

The first example of this class of objects was discovered in 1988 by Andy Fruchter and his collaborators. The system, named PSR B1957+20, consisted of a millisecond pulsar with a spin period of $\simeq 1.6$ ms (the second fastest known at that time), in a circular orbit with a very low-mass companion of mass $\simeq 0.02$ M$_\odot$ and with a short orbital period of $\simeq 9.17$ h. The pulsar signal resulted eclipsed for about 10% of the orbit, showing pronounced delays in the arrival times of the pulses, soon before and after its complete disappearance.

With this discovery it was thought to have finally detected the link between the so-called low-mass X-ray binaries (LMXBs) and the fully recycled binary radio pulsars. The former were indeed supposed to be the progenitors of the latter. Also, the system suggested a possible explanation for the existence of *isolated* recycled pulsars which, according to the first interpretations, would have resulted from irradiation, ablation and then complete evaporation of the companion by the pulsar energetic flux. However, as long as new observations accumulated, the picture became more and more complicated, for at least two reasons: 1) the observed time scales for the evaporation of the companion appeared

to be too long (longer than the age of the Universe) for allowing one to conclude that these systems are the progenitors of isolated recycled pulsars; 2) two classes of eclipsing pulsars progressively emerged: some of them were similar to PSR B1957+20, displaying very low-mass companions and some evidence of ongoing ablation; others appeared to have heavier companion masses ($\gtrsim 0.1$ M$_\odot$) and showed some clues about spontaneous physical processes (for instance a Roche lobe filling) which could have provoked the outflow of a significant fraction of their mass.

At any rate, it was then realized that, in both classes, a cloud of a presumably highly ionized gas must have formed and with which the pulsar radio signal is now forced to interact in its travel from the neutron star to the observer.

The paucity of known systems (only 3 in the Galactic field until two years ago plus a handful in globular clusters, difficult to study due to the large distance of these systems of stars) left many issues without an adequate justification, among which the three most important are:

- The physical mechanism underlying the observed eclipses.

- The link between eclipsing binaries and the various kinds of X-ray binaries.

- The link between eclipsing binaries and isolated recycled pulsars.

In the last two years various search experiments have led to the multiplication of the number of known systems in the Galactic field by a factor of over three and many additional discoveries are likely underway. This blooming of new eclipsing systems is triggering a new big burst of interest for this class of pulsars, hopefully paving the way to the possibility of finally addressing, in a satisfactory way, the three major aforementioned questions.

Given the framework described above, in this thesis work we developed a code (written in a modern language, like Python is) which allows us to reproduce the main physical processes which are thought to occur in eclipsing binary systems, in the aim of comparing the data with the simulated orbital modulated trends of the various possible observables. The primary goal is to exploit the code in order to put some constraints on the physical parameters of the considered systems and eclipse mechanisms, indicating the direction which has to be followed for potential future observations. As examples of the possible implementations, we applied our code to two systems which differentiate from each other both for their physical properties and for the phenomenological features which they display.

The thesis is organized as follows:

- In Chapter 1 we give a general introduction of pulsars, as well as summarizing their main phenomenological characteristics. We also review the principal theoretical models which have been put forward to explain the latter. The most widely accepted evolutionary scenario, that could explain the birth and the great variety of the observed sources, is then presented, along with a basic classification of the main kinds of binary systems including a pulsar.

- Chapter 2 is about the standard techniques which are used in studying a pulsar at radio frequencies. In particular, the *timing* procedure is the way thanks to which astronomers are able to derive the rotational, positional, kinematic and, if appropriate, orbital parameters of a pulsar to a very high degree of accuracy. Such information

are obviously fundamental for any other successive analysis of the source and its environment.

- Chapter 3 deals with the particular sub-class of systems which we presented above and which we are going to study: the eclipsing pulsars. The standard picture about their formation and evolution is reviewed and a further distinction between *Black Widow Pulsars* and *Redback* is also highlighted. We then discuss in detail the eclipse mechanisms which in principle could be able to account for the observed features. Finally, we draw our attention to the first eclipsing binary pulsar ever discovered, which is also considered the archetype of all the objects belonging to its class; in fact, it manifests most of the phenomenology which we could come across when looking at other similar systems.

- In Chapter 4, we present the code that we developed in the context of this thesis. We show its structure, its capabilities of modeling different physical processes as well as complicated geometrical configurations. In particular, we stress its ability to fit experimental data, by looking for the combination of parameters which best reproduces observations. We then test it on a well-known source which, besides showing features which are typical of eclipsing pulsars, also exhibits a rather high eccentricity in its orbit, thus representing a very good way for validating our code.

- In Chapter 5 and 6 we consider two real systems which, for different reasons, show odd behaviors and pose many questions about their physics and origin. We analyze the data we had and, with the aid of our code, we try to extract precious information about the possible eclipse mechanisms and system parameters. Finally, we suggest, for both of them, the kind of observations that would be useful for further investigations.

Chapter 1

Pulsars: an overview

The name "Pulsar" stands for "Pulsating Radio Source" and refers to the particular class of objects we are about to study in this thesis.

The discovery of pulsars dates back to the late 60s. In 1967 a group of astronomers led by Antony Hewish at the University of Cambridge, UK, were studying scintillation in the interplanetary medium when his student, Jocelyn Bell, found an interesting phenomenon: an extremely stable radio signal showing regular pulses separated by 1.33 seconds.
Even though in the beginning they didn't understand what they were actually observing, they soon realized that it had to be an extremely compact object, spinning very fast about its rotation axis. The picture soon became very clear, as many other similar signals were found over the next few years. Pulsars, as they were then named, were associated with particular neutron stars (that had been in turn theorized many years before) endowed with strong magnetic fields that in a way should be responsible for the observed radio emission.

1.1 The death of a massive star and the birth of a pulsar

As mentioned before, pulsars are essentially a particular kind of neutron stars. They originate from fairly massive stars (of mass $M \gtrsim 8 \ \mathrm{M_\odot}$) which have come to the end of their lives as supergiants.
Once a star runs out of the "fuel" needed to sustain itself against gravity, the collapse is inevitable; it then explodes as a supernova, ejecting its envelope out into space forming a so-called supernova remnant. In fact, it is not by chance that supernova remnants are often seen to surround isolated pulsars. Conversely, the core of the star collapses, getting much smaller and denser. Atoms are compressed so much that the inverse β-decay process,

$$p^+ + e^- \rightarrow n + \nu_e$$
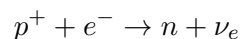
is now favored. While neutrinos leave the star undisturbed, protons and electrons fuse together, bringing about the *neutronization* of matter. Soon gravity is counteracted by a new force of quantum nature, i.e. the pressure of a degenerate fermion gas, in this case made out of neutrons. We now have a very compact but stable object: a neutron star (NS,

in brief) has formed. The structure of neutron stars has not yet been fully understood, but it's very likely to be constituted by an inner core along with other outer shells where matter arranges itself in different ways. If we could take a cross section of a NS, we would probably find [45]:

- An *inner core* where matter can reach densities of as much as $\rho > 10^{15}$ g cm^{-3}. Here strange matter could be found. Models cannot predict its actual content yet, since very few constraints on the equation of state of matter in such conditions are currently known.

- An *outer core* with $\rho \gtrsim 2 \cdot 10^{14}$ g cm^{-3}. It is chiefly made out of superdense and superfluid neutrons, as well as some superfluid protons and electrons.

- An *inner crust*, with $4.3 \cdot 10^{11}$ g cm$^{-3} = \rho_d \lesssim \rho \lesssim \rho_n = 2.4 \cdot 10^{14}$ g cm^{-3}. Here ρ_n is the typical nuclear density and ρ_d the so-called *neutron drip density*, beyond which there are no free bound states available in the nuclei for neutrons and these latter are compelled to leak out. The layer is actually a mixture of two phases: the first one is the Proton Rich Matter (PRM) and the second one is a neutron gas (NG). In addition to them there is an electron gas that guarantees charge neutrality.

- An *outer crust*, with 10^6 g cm$^{-3} \lesssim \rho \lesssim \rho_d = 4.3 \cdot 10^{11}$ g cm^{-3}, where a solid heavy nuclei lattice coexists with a degenerate electron gas (the main source of pressure in this layer) in β-decay equilibrium.

- A *surface*, with $\rho \lesssim 10^6$ g cm^{-3}. Here there is essentially the electron gas and it is a place where the magnetic field can play a role both for the equation of state of the neutron star and for the emission mechanism of a pulsar.

Apart from the equation of state, which is poorly known, we are interested in justifying some of the features pulsars exhibit. For example we would like to give an explanation to the extreme speed at which they spin and to their very intense magnetic fields. These are very easily explained in terms of conservation of angular momentum and magnetic flux after the supernova explosion. Let us call Ω_* and Ω_p the spin angular frequency of the progenitor star and of the pulsar, respectively; I_* and I_p are their moments of inertia, B_* and B_p their surface magnetic fields, R_* and R_p their radii. We can write:

$$I_* \Omega_* = I_p \Omega_p \qquad \Leftrightarrow \qquad \frac{2}{5} M R_*^2 \Omega_* = \frac{2}{5} M R_p^2 \Omega_p \qquad \Rightarrow \qquad \Omega_p = \Omega_* \frac{R_*^2}{R_p^2} \qquad (1.1)$$

where, for the sake of simplicity, we have regarded both the progenitor and the neutron star as uniform spheres of constant mass M. In the same way, if we consider the magnetic flux through the surface and assume it to be constant, we get:

$$B_* \cdot 4\pi R_*^2 = B_p \cdot 4\pi R_p^2 \qquad \Rightarrow \qquad B_p = B_* \frac{R_*^2}{R_p^2} \qquad (1.2)$$

Since $R_p \ll R_*$, this results in $\Omega_p \gg \Omega_*$ and $B_p \gg B_*$, as we actually observe.

1.2 Phenomenological features

In this section we are now going to briefly review the principal characteristics of a typical pulsar, which are evident from observations made through modern radio telescopes.

1.2.1 Pulses

The very regular pulsations visible in the radio band are likely due to the fact that the signal comes from emission beams located along the magnetic axis; since this latter is usually tilted with respect to the spin axis, our line of sight can intercept a beam once per rotation (unless the tilt angle is $\sim 90°$, in which case it can twice) so that we periodically reveal a rapid increase in the flux density, i.e. a pulse. By measuring the periodicity of the occurrence of the pulses one can get the spin period. Pulse intensities vary over a wide range and sometimes pulses are missing. Shapes are quite complex and can exhibit microstructures on timescales as short as 10 ns.

1.2.2 Periods

Pulsars can be split into two main categories, as we will see later, according to their rotational periods, magnetic fields and, indirectly, to their history:

- the *ordinary pulsars* show spin periods of the order of a second ($P \sim 1$ s), belong to a relatively young population (with an age of $\sim 10^7$ yr) and show magnetic fields of the order of $\sim 10^{12}$ G.

- the *short-period pulsars* (also known as *millisecond pulsars* or *recycled pulsars*) are about one thousand times faster ($P \sim 1$ ms) and about 10 to 100 times older (ages of about $10^8 \div 10^9$ yr) than the previous class. On the other hand they exhibit significantly lower magnetic fields of $\sim 10^8 \div 10^9$ G. All of these features are strictly related to their evolution path, which is quite different from that of ordinary pulsars.

Every time very accurate observations have been performed and special bias effects have been removed, in most cases pulsar periods were found to increase in a steady way, as one would expect if the primary source of the electromagnetic emission were, indeed, the rotational kinetic energy. Period derivatives are of the order of $\dot{P} \sim 10^{-15}$ s s^{-1} for ordinary pulsars and $\dot{P} \sim 10^{-18} \div 10^{-20}$ s s^{-1} for millisecond pulsars. The former sometimes also show sudden decreases in their periods (called *glitches*); the reason why millisecond pulsars are far less affected by them is linked to their age and their higher stability (see Section 1.6).

1.2.3 Profiles

It is important to remark that, even if single pulses emerge extremely regularly in time, they look very different from one to another. Nevertheless, if we take a time series of some few hundreds or thousands of pulses and coherently add them together (a procedure called *folding*) we can obtain an integrated pulse profile whose shape is instead very stable.

Thanks to this profile each single pulsar can then be identified univocally. The study of the shape also lets us investigate the size and the structure of the emission beam.

As shown in Figure 1.1, integrated profiles of different pulsars can differ a lot and display peculiar features, such as complex multi-peaked structures as well as multiple components. Integrated profiles can also vary significantly both with time and frequency. A change in the orientation of the beam (for instance because of free precession in isolated neutron stars and geodetic precession in binary systems) can in fact be responsible for the time evolution. The dependance on the observing frequency is more evident and present in almost all pulsars. Specifically, at decreasing frequencies, the pulse shape usually widens and the different components of the profile get farther apart. Such effects are consistent with the idea that the higher frequency emission components are produced closer to the neutron star surface, where the magnetic field lines result almost perpendicular to it, so that the relative beam gets narrower (see Section 1.5).
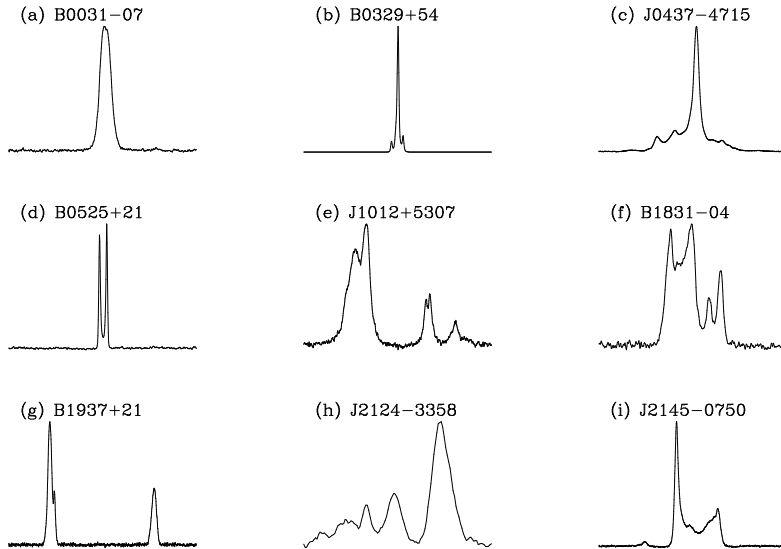
Figure 1.1: Different integrated pulse profiles for different pulsars [35].

1.2.4 Emitted Spectrum

Plotting the observed mean flux density S_{mean} against the observing frequency f, it is easy to note a strong inverse dependance. Approximately we can regard it as a power-law with a certain spectral index, ξ:

$$S_{\mathrm{mean}}(f) \propto f^{\xi} \tag{1.3}$$

Usually, $-4 \leq \xi \leq 0$ with an average observed value of $\xi \simeq -1.8 \pm 0.2$ [35]. Sometimes it can be observed a deviation from a power-law at low frequencies, others the spectrum can be fitted by a double power-law, with different indexes for low ($f \lesssim 1$ GHz) and high ($f \gtrsim 1$ GHz) frequencies. In this case, ordinary and millisecond pulsar do not seem to show substantial differences.

1.2.5 Polarization

By now, it is well-known that pulsars are among the most polarized radio sources that can be find in nature. With the aid of proper instrumentation one can measure the four Stokes parameters of the incoming radiation. Statistical analyses suggest that pulsar radiation is about 20% linearly polarized and about 10% circularly polarized, on average [35]. Moreover, a remarkable feature to inspect is the behavior of the so-called *position angle* of linear polarization. Remembering the definitions of the four components of a Stokes vector,

$$S_0 \equiv I = E_{0,x}^2 + E_{0,y}^2 \tag{1.4}$$

$$S_1 \equiv Q = E_{0,x}^2 - E_{0,y}^2 \tag{1.5}$$

$$S_2 \equiv U = 2E_{0,x}E_{0,y}\cos\delta \tag{1.6}$$

$$S_3 \equiv V = 2E_{0,x}E_{0,y}\sin\delta \tag{1.7}$$

where $E_{0,x}, E_{0,y}$ are the two orthogonal components of the electric field and δ is their relative phase shift, the position angle is defined as follows:

$$\Psi \doteq \frac{1}{2}\arctan\left(\frac{U}{Q}\right) \tag{1.8}$$

The relevant fact is that it usually varies in a smooth and regular fashion along the pulse phase of an integrated pulse profile, indicating that the magnetic field lines probably play a role in determining the linear polarization. This interpretation was due to Radhakrishnan and Cooke, who in 1969 first modeled the phenomenon describing it by their still often invoked *rotating vector model* [41]. The typical S-shape of Ψ along the pulse can be seen in Figure 1.2. Again, millisecond pulsars behave differently, rarely showing regular trends in their position angles.
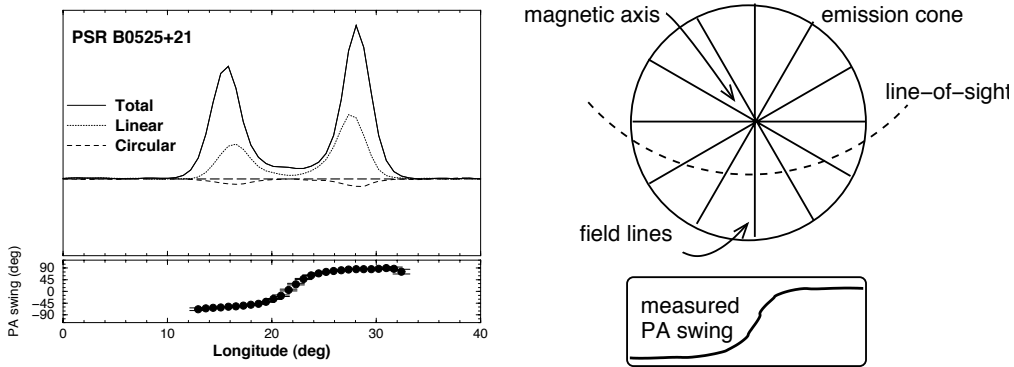
Figure 1.2: *Left*: polarization profile of PSR B0535+21 as observed form the Effelsberg radio telescope. It is clearly visible the characteristic S-like swing of the position angle (PA) of the linear component. *Right*: a representation of the rotating vector model by Radhakrishnan and Cooke, which explains the S-shape in terms of the projection of the magnetic field line direction onto our line-of-sight crossing the emission cone [41].

1.3 Derived physical parameters

One of the most interesting fact about pulsars is that one can get an estimate of many physical parameters just by looking at some easily-observable quantities: the spin period P and its first derivative $\dot{P}$. The second derivative $\ddot{P}$ is seldom measured but can provide us with additional useful information about the emission mechanism.

1.3.1 Dipole radiation, pulsar spin-down and the braking index

In the current most-widely accepted view, pulsars are thought to be fast-rotating stars with strong, approximately dipolar, magnetic fields whose axes are misaligned with respect to their rotation axes. As a result, they must emit some radiation, as first proposed Pacini. In particular, we remind here [29] that a magnetic dipole with a magnetic moment $\vec{m}$, tilted by an angle α with respect to the spin axis about which it rotates at an angular frequency Ω, radiates energy at a rate of:

$$\dot{E}_{\mathrm{dipole}} = \frac{2}{3}\frac{|\vec{m}|^2\Omega^4\sin^2\alpha}{c^3} \tag{1.9}$$

From this equation one can see that, for sources like the Crab pulsar ($P = 33$ ms, $B \simeq 4 \cdot 10^{12}$ G), the released power is almost 100 times that of the Sun. On the other hand, the ultimate source of energy of the pulsar is the kinetic energy due to its rotation, whose rate of loss can be expressed as:

$$\dot{E}_{\mathrm{rot}} \equiv -\frac{d}{dt}\left(\frac{1}{2}I\Omega^2\right) = -I\Omega\dot{\Omega} = 4\pi^2 I\frac{\dot{P}}{P^3} \tag{1.10}$$

where I is the moment of inertia, Ω is the spin angular frequency and we have used the relation $P = 2\pi/\Omega$.

If we assume the dipole emission to be the only mechanism through which the pulsar loses energy, we can equate eq. (1.9) to eq. (1.10), thus getting:

$$\dot{\Omega} = -\left(\frac{2|\vec{m}|^2\sin^2\alpha}{3Ic^3}\right)\Omega^3 \tag{1.11}$$

Using the rotational frequency $\nu = 1/P = \Omega/2\pi$ and expressing it as a power-law, we can rewrite the last equation as:

$$\dot{\nu} = -K\nu^n \tag{1.12}$$

where K is a constant and, more importantly, n is called *braking index* and equals 3 in the pure dipole case. This law is very useful as it allows us to probe the emission mechanisms. In fact, we can differentiate eq. (1.12), use it again to get rid of K, to then obtain:

$$n = \frac{\nu\ddot{\nu}}{\dot{\nu}^2} \tag{1.13}$$

Thus, by measuring the period of the pulsar and their two first derivatives, one can look for deviations from $n = 3$, which would indicate that other mechanisms, as well as the dipolar emission, actually come into play.

1.3.2 Characteristic age

As we said in the previous section, a pulsar usually slows down. By measuring the rate of loss of rotational speed along with its period, we can also infer how old it is, as shown in the following. Let us rewrite eq. (1.12) in terms of the period:

$$\dot{P} = K'P^{2-n} \tag{1.14}$$

where K' is a new constant that includes the previously defined K. We can then integrate it assuming $n \neq 1$:

$$\int_{P_0}^{P} P^{n-2}dP = K' \int_{0}^{\tau_p} dt \tag{1.15}$$

Here τ_p is the real age of the pulsar. We have also introduced P_0 as the spin period at birth. Solving, we find:

$$\tau_p = \frac{P}{(n-1)\dot{P}}\left[1 - \left(\frac{P_0}{P}\right)^{n-1}\right] \tag{1.16}$$

As one can see, the real age will in general depend both on the braking index (that is, on the emission mechanism) and on the spin period at birth. Usually, the latter is not known, but we can be confident of the fact that it had to be much shorter than the current value, so that we can make the approximation $P_0 \ll P$; in addition to this, we can assume the dominant emission process to be the magnetic dipole, by setting $n = 3$. In this way, eq. (1.16) gets far simpler and we can refer to this new particular quantity as the *characteristic age* of the pulsar, in the sense that it only gives us the order of magnitude of the real age:

$$\tau_c = \frac{P}{2\dot{P}} \tag{1.17}$$

Again, by measuring only very simple observables, fundamental information can be obtained. Furthermore, if there exist a way other than measuring the period and its derivative to compute the age of a pulsar (for example by studying the supernova remnant that surrounds it) one can compare it to the characteristic age in order to determine the braking index and thus investigate the energetics of the source.

1.3.3 Characteristic magnetic field

We know that the relationship between the magnetic field magnitude and the magnetic moment in the case of a dipolar field is:

$$B(r) \approx \frac{|\vec{m}|}{r^3} \tag{1.18}$$

where r is the distance from the magnetic axis. Assuming the dipole braking as the only spin-down mechanism, we can take eq. (1.11), solve it for $|\vec{m}|$ and express the magnetic field strength B_S at the surface of the pulsar ($r = R_p$) as a function of measurable quantities:

$$B_S \equiv B(r = R_p) = \sqrt{\frac{3c^3}{8\pi^2}\frac{I}{R_p^6 \sin^2 \alpha}P\dot{P}} \tag{1.19}$$

Obviously, we also need to know the moment of inertia as well as the pulsar radius; good estimates are $R_p \approx 10$ km and $I \approx 10^{45}$ g cm^2. Since we don't even know the tilt angle, we can get a lower limit to the field strength by setting $\alpha = 90°$, so that we can express:

$$B_S \approx 10^{12} \text{ G} \cdot \left(\frac{\dot{P}}{10^{-15}}\right)^{1/2} \cdot \left(\frac{P}{\text{s}}\right)^{1/2} \tag{1.20}$$

This is what we call the *characteristic magnetic field* because, again, it can only provide us with a hint about the order of magnitude of the actual field intensity near the surface.

1.4   The surrounding magnetosphere

Up to now, in trying to explain its emission, we have supposed the pulsar to be in vacuum. In reality, it was pointed out that, if we regard the neutron star as a highly magnetized, rotating, superconducting sphere, this hypothesis cannot stand. The strong electric fields which form, inevitably lead to the extraction of charged particles from the surface, generating a dense plasma all around the star, that is what we call the *pulsar magnetosphere*.

The model of magnetosphere we present here is due to Goldreich and Julian [23] and it is known as the *aligned-rotator model*, since the basic assumption is that the magnetic axis is parallel to the rotation axis. Despite this and other features resulting faulty in the case of magnetized neutron stars, is worth reviewing the Goldreich-Julian model not only because it embodies the basics on which all the other models are built, but also because it adapts perfectly to black-hole electrodynamics, for which all the defects of the model do not apply.

Let us first suppose the pulsar to have an external dipolar magnetic field that is aligned to the rotation axis about which the pulsar is spinning at an angular frequency Ω in vacuum. At a distance $\vec{r}$ from its center, we have:

$$\vec{B}^{(out)} = B_p R^3 \left(\frac{\cos\theta}{r^3}\hat{e}_r + \frac{\sin\theta}{2r^3}\hat{e}_\theta\right) \tag{1.21}$$

where (r, θ) are the usual polar coordinates in a frame centered on the star and B_p the field strength at the magnetic pole. We want to estimate the forces acting on the surface charges and understand whether the vacuum condition can be maintained or not.

Since the neutron star is very similar to a conducting sphere, we expect the charges to move in a way such that, inside the star, the net force acting on them vanishes. Formally, this results in:

$$\vec{F}_{tot} = \vec{E}^{(in)} + \frac{\vec{v}}{c} \times \vec{B}^{(in)} = 0 \qquad \text{with} \quad \vec{v} = \vec{\Omega} \times \vec{r} \tag{1.22}$$

Eq. (1.22) says that, underneath the surface, a non-vanishing electric field is present, namely:

$$\vec{E}^{(in)} = \frac{R\Omega B_p \sin\theta}{c}\left(\frac{\sin\theta}{2}\hat{e}_r - \cos\theta\,\hat{e}_\theta\right) \tag{1.23}$$

It is also well-known that the tangential component of the electric field, E_θ, is continuous across the surface of a conductor, and thus:

$$\left. E_\theta^{(out)} \right|_{(r=R)} = \left. E_\theta^{(in)} \right|_{(r=R)} = -\frac{R\Omega B_p}{c} \sin\theta \cos\theta \qquad (1.24)$$

We can use the Poisson equation, $\nabla^2 \Phi = 0$, outside the star (with the boundary conditions given by eq. 1.22) and the tangential component of the electric field at the surface (eq. 1.24) in order to get the electrostatic potential Φ:

$$E_\theta = -\frac{1}{r}\left(\frac{\partial \Phi}{\partial \theta}\right) \qquad \Rightarrow \qquad \Phi = -\frac{\Omega B_p R^5}{3cr^3} P_2(\cos\theta) \qquad (1.25)$$

where $P_2(\cos\theta) = (3\cos^2\theta - 1)/2$ is the 2nd-order Legendre polynomial. It can be shown that this potential generates a quadrupolar electric field configuration outside the neutron star.

Now we can calculate the component of the electric field parallel to the magnetic field at the surface, $\vec{E} \cdot \vec{B}$. The reason why we consider this latter rather than simply the radial component, E_r, is related to the typical order of magnitude of $\vec{B}$. In fact, in the case of very strong magnetic fields, the motion of charged particles perpendicularly to the field lines is strongly suppressed. The Larmor radius in the non-relativistic case gives us an estimate of the length scale of this motion:

$$r_L = \frac{m_e v c}{eB} = 3 \cdot 10^{-11} \text{ cm} \cdot \left(\frac{T}{10^6 \text{ K}}\right)^{1/2} \cdot \frac{10^{12} \text{ G}}{B} \qquad (1.26)$$

where m_e is the electron mass, e its charge. It is easy to see how tiny it is even in the cases of "weak" magnetic fields, proper to recycled pulsars. The force exerted by B perpendicularly to the field line is so intense that makes the electric field component in that direction completely negligible. The relevant component is instead:

$$\vec{E} \cdot \vec{B} = -\frac{\Omega R}{c}\left(\frac{R}{r}\right)^7 B_p^2 \cos^3\theta \qquad (1.27)$$

Then it must be computed at the surface, to get the electric force F_e, and also be compared to the gravitational pull F_g:

$$\frac{F_e}{F_g} \sim \frac{eR\Omega B_p/c}{GM_p m/R^2} \qquad (1.28)$$

If one calculates the ratio for proton ($m = m_p$) and for electrons ($m = m_e$) the result will be huge ($> 10^6$) in both cases for the typical parameters of a pulsar. Hence, charged particles are inevitably ripped off the surface and start filling the surrounding vacuum. A plasma magnetosphere builds up and a new non-vacuum state is soon attained thanks to the extracted particles that are forced to rigidly co-rotate with the field lines. However, the co-rotation can be maintained only up to the distance R_{LC} at which the particle tangential velocity reaches the speed of light, namely:

$$R_{LC} = \frac{c}{\Omega} \simeq 4.77 \times 10^4 \text{ km} \cdot \left(\frac{P}{s}\right) \qquad (1.29)$$

This distance is called *light-cylinder radius* and defines a region, cylindrical in shape, which divides the magnetosphere into two main regions:

- The *closed magnetosphere*, where the field lines close inside the light cylinder and particles can rigidly rotate with them, making the whole region a perfect conductor just like the interior of the star, and hence $\vec{E} \cdot \vec{B} = 0$ still holds.

- The *open magnetosphere* where the field lines should close beyond the light cylinder but cannot because of the aforementioned reasons. Particles are free to escape and thus $\vec{E} \cdot \vec{B} \neq 0$. Here, in this open region, it is believed to originate the radio emission of pulsars.

1.5   Emission mechanism

In the light of the picture drawn so far, we can try to give a theoretical explanation for the observed signals coming from pulsars at the different wavelengths. Remember that the pulsed radio emission (which, still, we do have to take into account) represents only a minuscule fraction of the total rotational energy converted into radiation.

Considering this, a simple emission mechanism that fits the requirements is the *Cone Beam* model, capable of justifying at least the following features:

- Focused emission.

- Constancy of the emitting region size.

- Strong linear polarization independent of frequency.

According to this model, the extracted particles at the surface undergo such a strong acceleration along the magnetic field lines that they rapidly become relativistic. The $\vec{B}$-field geometry gives rise to the emission of curvature radiation, with photons γ whose energy E_γ exceeds the rest mass of two electrons; therefore they soon decay in $e^+ e^-$ pairs which are accelerated again in an upper layer of the magnetosphere. New photons, which soon after decay in pairs, are then produced and so on, until the energy of single photons is enough to sustain the process (that is $E_\gamma > 2m_e c^2$). The radiation is in this way directed tangentially to the field line at the point of the emission, resulting in extremely collimated and linearly polarized beams. Successive generations of $e^+ e^-$ pairs and subsequent photons are less and less energetic and are produced farther and farther away from the surface, where the tangents to the field are less parallel to the magnetic axis. This represents a way to explain the narrower pulses observed at higher radio frequencies as well as the large bandwidth of the radio signal itself. Other possible theories for the radio emission have been proposed, locating the region of acceleration of the emitting particles also in other portions of the magnetosphere.

The recent results from the new γ-ray satellites like AGILE and Fermi seem to indicate that the gamma-ray emission (which is seen in more than a hundred radio pulsars) more frequently originates from the so-called *outer gap* region, a part of the magnetosphere in the neighborhood of the light cylinder. In fact, particles at distance $\sim R_{LC}$ in the equatorial plane approach the speed of light; thus, they must be highly relativistic and produce high-frequency radiation.
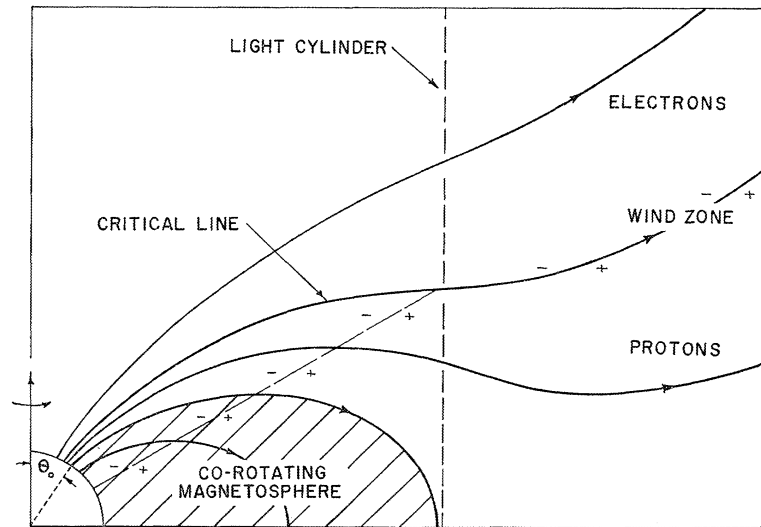
Figure 1.3: Sketch of the Goldreich-Julian model of the magnetosphere of a pulsar, in the picture of an aligned magnetic field axis.
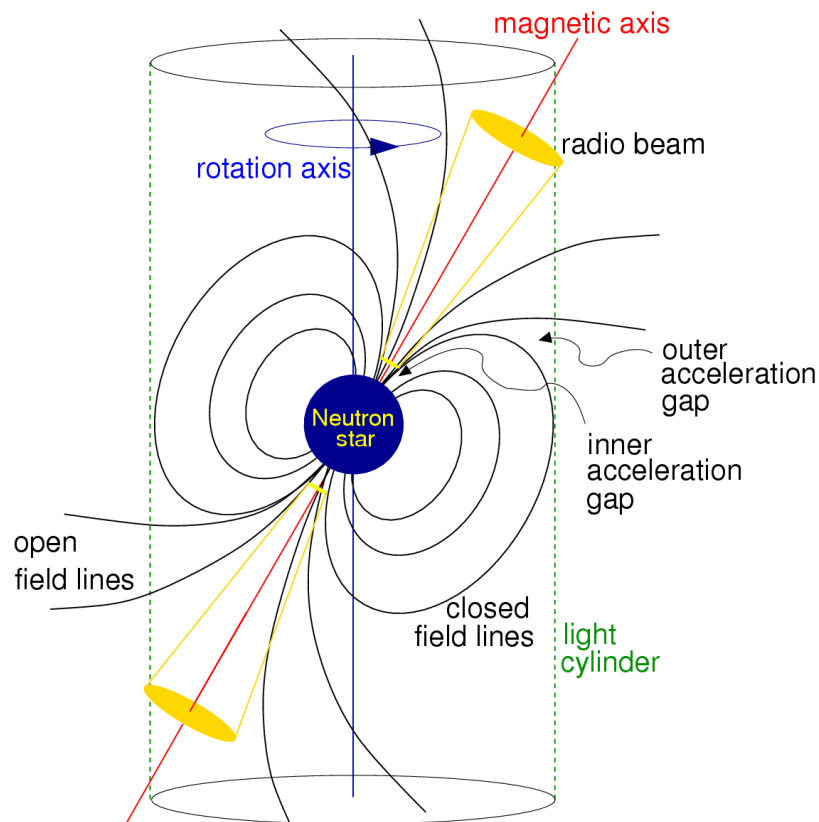
Figure 1.4: Sketch of the basic geometrical model of the magnetosphere of a pulsar.

1.6   Evolution and classification

Once we have depicted the principal aspects of the physics governing a pulsar, we are ready to predict its evolution over time; it is a common practice to represent it on a $P - \dot{P}$ (or, equivalently, $P - B$) diagram, like that of Figure 1.5.
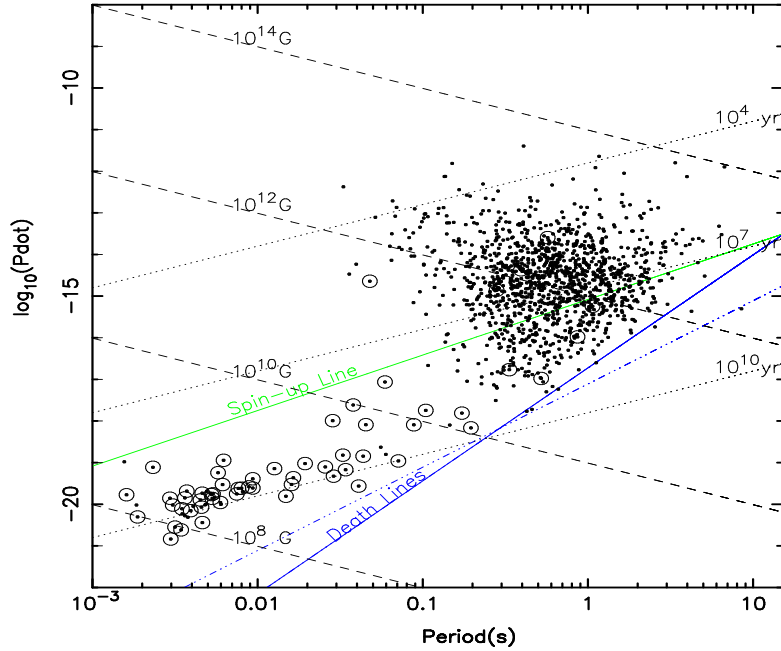
Figure 1.5: In a $P - \dot{P}$ diagram, the two populations of ordinary and millisecond pulsar distinctively separate into different regions.

When a pulsar is first generated from the explosion of a supernova, it is placed on the upper-left part of the graph, having quite a strong magnetic field (and hence, a high $\dot{P}$) as well as a spin period of the order of tens of milliseconds. Being its rotation the only source of energy, a pulsar can only slow down. In fact eq. (1.12) tells us that, no matter the actual emission mechanism, its period P must increase, corresponding to a horizontal rightward shift on the diagram. The shift continues until the magnetic field and rotational speed are not able to sustain the pulsed radio emission any more; when this happens the pulsar crosses the so-called *death line*, beyond which, even if still emitting, the source cannot be observed because of its faintness. It is important to note that this line strongly depends on the assumed emission mechanism, even if most models are substantially in accord in describing it. The fact that most of the observed pulsar (as one can see in Figure 1.5) cluster in the vicinity of the death line is related to the fact that the horizontal shift normally occurs over very short time scales; young pulsars boast very strong magnetic fields and short periods, so that the spin-down is quite rapid. Consequently, the probability of spotting new-born sources is rather low and that explains the issue. Moreover, young pulsars are also fairly unstable and often show sudden decreases in their periods (the above-cited phenomena known as *glitches*) whose origin is very likely linked to "star-quakes", namely re-arrangements of the neutron star crust which abruptly change the moment of inertia and, thus, the spin frequency.

1.6.1 Spin-up to millisecond periods

It is well-know that, in general, stars tend to couple. Almost half of the observed stars turn out to be in a binary system with a companion. Analogously, it is very common to have pulsars that were formed in a binary system, previously composed by two main-sequence stars. The evolution of such sources basically depend on the initial masses of the two components. When one of the two stars explodes as a supernova, two main paths can then be followed:

- **Disruption** From considerations related to the Virial Theorem it can be proved that, in ideal conditions, if more than half the total mass of the whole system is ejected out of the binary, this latter will be disrupted. If the explosion is slightly asymmetric (as usually occurs), a "kick" to the pulsar will be imparted, flinging it away at high velocity ($10 \div 1000$ km/s). The source will be later observed as an isolated ordinary pulsar, evolving in the previously explained standard fashion.

- **Survival** If the new-born pulsar and the main-sequence star remain tied to each other, the system will initially show a high eccentricity due to the effect of the explosion. For a while the pulsar may be visible as an ordinary one, with the usual characteristics we have already discussed. But, later, the main-sequence star evolves itself becoming, for instance, a giant; such a star, in the vicinity of a compact object, will likely transfer part of its mass to the neutron star, either via its strong wind or by filling its Roche-lobe, allowing the outflowing of matter through the inner Lagrangian point L2. The accretion makes the pulsar acquire spin angular momentum at the expense of the orbital one, in a process that is called *pulsar recycling*. While accretion is ongoing, the system can be observed as an X-ray binary, whose name is obviously due to the fact that they are primarily detectable at X-rays, since most of the emission occurs in that band of the electromagnetic spectrum. The in-falling matter on the neutron star provokes both an acceleration in its rotation and a decay in its magnetic field. For this reason the source will progressively move toward the bottom-left part of the $P - \dot{P}$ diagram, where indeed most of the observed millisecond pulsars can be found.

1.6.2 X-ray binaries

Let us focus on the new class we have just introduced, i.e. X-ray binaries. Such accretion-powered systems are further divided into subcategories, according to the mass of the donor star.

- High-Mass X-ray Binaries (HMXBs) are characterized by companions of mass $M_c \gtrsim 10$ M$_\odot$ belonging to the O-B-Be spectral type and hence they are very young systems (age $< 10^7$ yr). The spin-up of the pulsar occurs by wind-driven accretion or through a Roche lobe overflow of the companion atmosphere. They usually have rather long orbital periods (tens or hundreds of days) with fairly eccentric orbits. The typical end product, in the case of survival of such a system after the supernova explosion of the donor star, is a double neutron star binary (Figure 1.7, case D).

- Intermediate-Mass X-ray Binaries (IMXBs) are those system in which 1 M$_\odot \lesssim M_c \lesssim 10$ M$_\odot$ [56]. The typical spin periods of pulsars coming from such systems are of the

order of tens of milliseconds, suggesting that in IMXBs the recycling process lasts less than in the next category [47]. These sources are called *mildly-recycled* pulsars.

- Low-Mass X-ray Binaries (LMXBs) have faint optical companions with 0.1 M$_\odot$ $\lesssim$ $M_c \lesssim 1$ M$_\odot$ associated with old population II, G-K spectral type, stars. This feature makes these systems much older than HMXBs, with ages of over 10^9 yr, allowing their pulsars to be recycled for a far longer time and to be spun-up to millisecond periods. Consequently, the typical measured magnetic fields are weak, $\sim 10^8 \div 10^9$ G. Since the small mass prevents the donor from developing a strong equatorial wind, the principal accretion mechanism is the Roche lobe overflow. Tidal forces and magnetic torques during accretion have enough time to circularize the orbit and make the system lose additional angular momentum. Hence, LMXBs usually have much shorter orbital periods (~ 1 d) and very small eccentricities. Once the recycling is complete, the donor has lost its outer shells and has become a He or C-O white dwarf, depending on the initial mass.

- Very Low-Mass X-ray Binaries (VLXBs) exhibit companions of mass $M_c \lesssim 0.1$ M$_\odot$ which probably powered accretion of matter for even longer periods of time. This class thus includes the progenitors of the most heavily recycled pulsars ever discovered; this statement is confirmed by the observed spin periods of the pulsars hosted in such systems, which are at most $\simeq 5$ ms [20]. Their extremely tight orbits, with periods of the order of hours, make some of them show radio signal eclipses while the pulsar passes behind the companion, indicating that the latter is bloated or is evaporating because of the pulsar radiation [47].

At the end of the accretion process, each of these kind of binaries will stop emitting X-rays and will turn on again its radio emission, becoming visible as a recycled pulsar.

1.7 Population distributions

As of 2012, more than 2000 pulsars are known[1], with more than a half spotted in the last 10 years, especially thanks to the recent all-sky surveys, such as that performed at Parkes. All the pulsars discovered so far (with the exception of a handful of objects spotted in the Magellanic Clouds) have turned out to be of Galactic origin and this is proved both because most of them are crowded in the plane of the Milky Way and because their dispersion measures nicely fit the current models of the Galactic ionized matter distribution. The two populations of ordinary and millisecond pulsars, have substantially different spatial distributions. The former are concentrated in the Galactic plane, mimicking the distribution of the most massive O-B stars and, thus, confirming their supposed origin from supernova explosions. The latter instead spread out across higher Galactic latitudes, supporting the hypothesis of the "supernova kicks" which, during the long life of such sources, have let them go away to greater distances. Many of the binary millisecond pulsars have also been found in globular clusters. As we will see, they play a significant role in the formation of Very Low-Mass Systems, those from which most of the eclipsing pulsars originate.

---

[1]http://www.atnf.csiro.au/people/pulsar/psrcat/
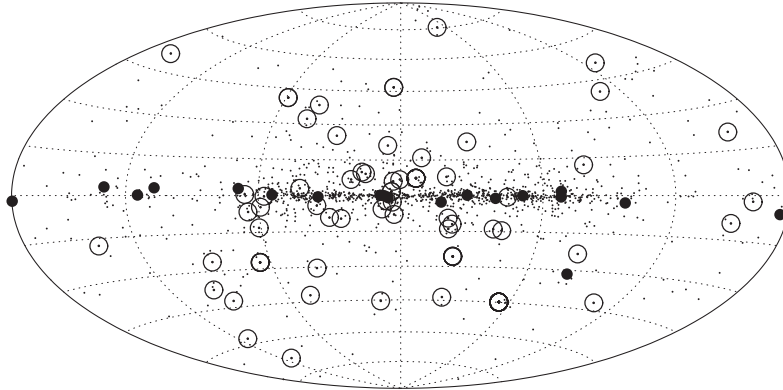
Figure 1.6: The distribution of pulsars in Galactic coordinates. Pulsar–Supernova Remnant associations and millisecond pulsars are represented by the filled and open circles, respectively. Ordinary pulsars are shown as simple dots.
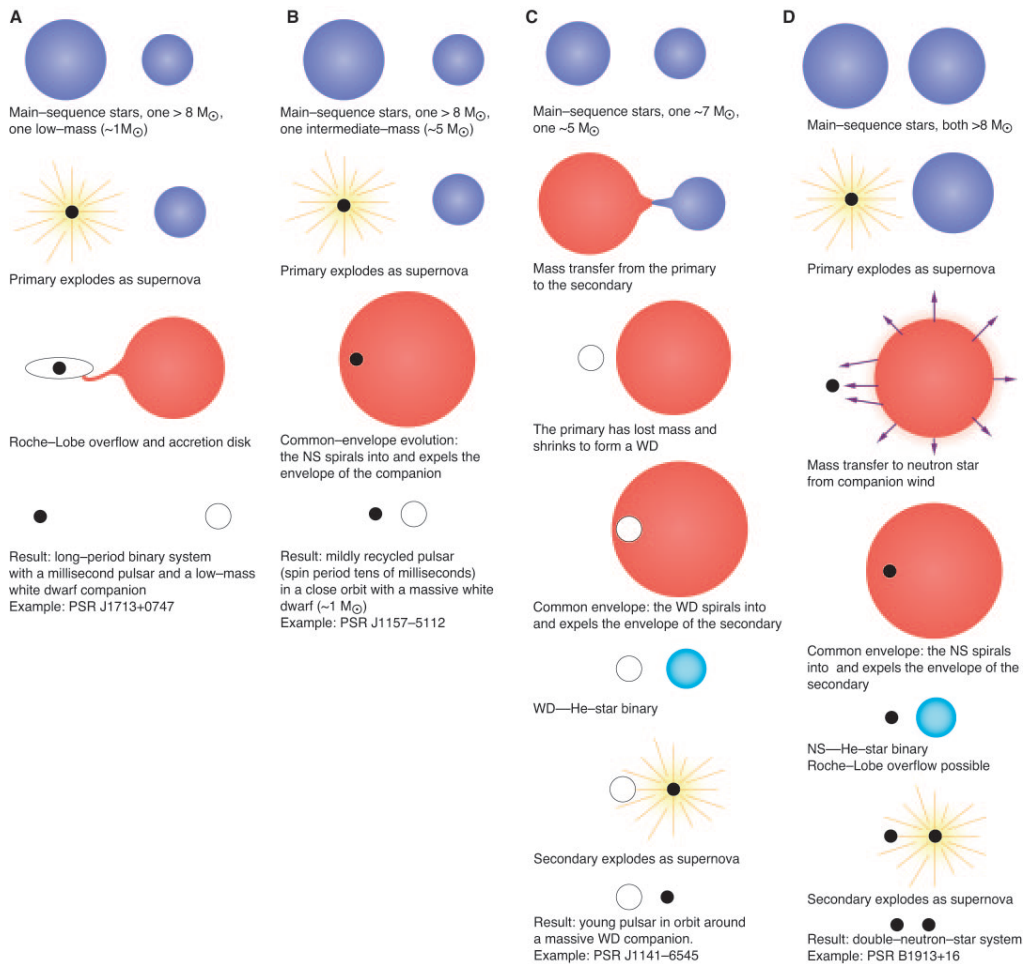
Figure 1.7: Schematic representation of some possible evolutionary paths of binary systems. Credits: [47].

Chapter 2

Observing a pulsar

All the information we can get about a pulsar comes from its pulsating signal at various radio frequencies. It is then straightforward to understand the relevance of properly handling these data. In all cases the raw signal we receive is not suitable for a direct analysis and must be pre-processed (an operation that we call *data reduction*) in order to make it usable. In this chapter we will review the principal effects that influence the pulsar radiation and that one must take into account when dealing with data. We will then explain the basic concepts of *timing*, the primary way by which astronomers study pulsars and determine their physical and orbital parameters.

2.1 Plasma effects on propagating waves

Before reaching the observer, the radio wave emitted by a pulsar must travel a very long distance, often of the order of kiloparsecs or more. Along its path it comes across the interstellar medium (ISM), which is present all over the Galaxy. The ionized component of the ISM influences the propagation of the signal, modifying its shape and flux. The Galactic magnetic field also makes the ISM slightly magnetized and this causes changes in polarization of traveling electromagnetic waves. The most relevant effects are thus the following:

1. Dispersion

2. Faraday Rotation

3. Scattering

4. Scintillation

While effects (1) and (2) are effective in a homogeneous plasma, effects (3) and (4) require the plasma to be inhomogeneous and/or turbulent.

2.1.1 Dispersion

Let us consider a cold homogeneous medium made of charged particles, i.e. electrons and nuclei. In the presence of an electromagnetic wave, the electrons will undergo a net force $\vec{F} = -e\vec{E}$. Calling ω the pulsation of the radiation, k the wavenumber, the electric field can be expressed as $\vec{E}(t) = \vec{E}_0 e^{i(\vec{k}\cdot\vec{x} - \omega t)}$. Being m_e the electron mass, we can find the velocity $\vec{v}$ of the electron as a function of time by a simple integration:

$$\vec{F} = m_e \frac{d\vec{v}}{dt} = -e\vec{E} \quad \Rightarrow \quad m_e \int d\vec{v} = -e \int \vec{E}_0 e^{i(\vec{k}\cdot\vec{x}-\omega t)} dt$$
$$\Rightarrow \quad \vec{v}(t) = -\frac{ie}{\omega m_e}\vec{E}(t) \tag{2.1}$$

Now, using eq. (2.1) and comparing the two definitions of the current density $\vec{J}$, we can solve for the electric conductivity σ of the medium:

$$\begin{cases} \vec{J} = -n_e e\vec{v} \\ \vec{J} = \sigma\vec{E} \end{cases} \quad \Rightarrow \quad \begin{cases} \vec{J} = \frac{in_e e^2}{\omega m_e}\vec{E} \\ \vec{J} = \sigma\vec{E} \end{cases} \quad \Rightarrow \quad \sigma = \frac{in_e e^2}{\omega m_e} \tag{2.2}$$

where n_e is the electron number density. On the other hand, we can recall the continuity equation and express it in the Fourier domain:

$$\frac{\partial\rho(t)}{\partial t} + \vec{\nabla}\cdot\vec{J} = 0 \quad \xrightarrow{\text{Fourier}} \quad -i\omega\rho(t) + i\vec{k}\cdot\vec{J} = 0 \tag{2.3}$$

where $\rho(t)$ is the charge density. Remembering that $\vec{J} = \sigma\vec{E}$, we obtain:

$$\rho(t) = \frac{1}{\omega}\sigma\vec{k}\cdot\vec{E} \tag{2.4}$$

Now that we have expressions for $\vec{J}$ and ρ, i.e. the sources of the electromagnetic field, we can substitute them in Maxwell's equations in the frequency domain. The result is:

$$\begin{cases} i\vec{k}\cdot(\epsilon\vec{E}) = 0 \\ i\vec{k}\cdot\vec{B} = 0 \\ i\vec{k}\times\vec{E} = \frac{i\omega}{c}\vec{B} \\ i\vec{k}\times\vec{B} = -\frac{i\omega}{c}(\epsilon\vec{E}) \end{cases} \tag{2.5}$$

The relevant fact is that the so-obtained Maxwell's equations are formally identical to the case of propagating in vacuum, except for the presence of a multiplicative factor ϵ, defined as:

$$\epsilon = 1 - \frac{4\pi\sigma}{i\omega} = 1 - \frac{4\pi n_e e^2}{m_e\omega^2} = 1 - \frac{\omega_p^2}{\omega^2} \tag{2.6}$$

where we have also defined the *plasma pulsation* ω_p as:

$$\omega_p \doteq \sqrt{\frac{4\pi n_e e^2}{m_e}} \tag{2.7}$$

Consequently, the *plasma frequency* is trivially $f_p = \omega_p/2\pi$. We also know that, in general, the following relation between the wavelength λ, the frequency f and propagation velocity v of an electromagnetic wave, holds:

$$\lambda f = v \quad \Leftrightarrow \quad \frac{\omega}{k} = v \tag{2.8}$$

In addition to this, from Maxwell's equations, we have $v = \frac{c}{\sqrt{\epsilon}}$, so that:

$$\frac{\omega}{k} = v = \frac{c}{\sqrt{\epsilon}} \qquad \Rightarrow \qquad \frac{\omega^2}{k^2} = \frac{c^2}{\epsilon} \qquad \Rightarrow \qquad k^2 c^2 = \omega^2 \epsilon \qquad (2.9)$$

and thus, straightforwardly:

$$k^2 = \frac{1}{c^2}(\omega^2 - \omega_p^2) \qquad (2.10)$$

The first thing that can be noticed is that, depending on whether the radiation pulsation ω is higher of lower than the plasma pulsation, eq. (2.10) does have solutions or not. Indeed:

$$\omega < \omega_p \qquad \Rightarrow \qquad k^2 < 0 \qquad \Rightarrow \qquad \text{no solutions}$$
$$\omega > \omega_p \qquad \Rightarrow \qquad k^2 > 0 \qquad \Rightarrow \qquad \text{two solutions}$$

The first corresponds to the case in which radiation is absorbed by the ionized medium, whilst the second one indicates an effective propagation. To see at which speed the signal will then travel, we recall the definition of group velocity v_g of an electromagnetic wave and, by first reversing eq. (2.10), we calculate its expression as a function of the frequency f (or, equivalently, of the pulsation ω):

$$v_g = \frac{\partial \omega}{\partial k} = \frac{\partial}{\partial k}(k^2 c^2 + \omega_p^2)^{1/2} \qquad (2.11)$$

from which we get:

$$v_g = c\sqrt{1 - \frac{\omega_p^2}{\omega^2}} = c\sqrt{1 - \frac{f_p^2}{f^2}} \qquad (2.12)$$

As we can see in Figure 2.1a, the group velocity is an increasing function of frequency, asymptotically tending to c for $f \to \infty$.

The measurement of distance

We can exploit the dispersion effect in order to guess how far a pulsar is. We saw that the refraction index of the medium as seen by an electromagnetic wave (and the propagation speed of this latter) actually depends on the wavelength. It is easy to calculate the delay $\Delta t_{(f,\infty)}$ with which the signal emitted by a pulsar would reach the Earth, from a distance d, with respect to an infinite-frequency wave (or, equivalently, in the absence of plasma):

$$\Delta t_{(f,\infty)} = \left(\int_0^d \frac{dl}{v_g} \right) - \frac{d}{c} \qquad (2.13)$$

where the integral is performed along the optical path, from the source to the observer. Since the standard observing frequencies are by far higher than the typical plasma frequency ($f \gg f_p$) we can expand the dispersion relation (2.12) as a Taylor series to first order and substitute it in eq. (2.13), so that:

$$\Delta t_{(f,\infty)} \simeq \frac{1}{c} \int_0^d \left[1 + \frac{1}{2} \frac{f_p^2}{f^2} \right] dl - \frac{d}{c} = \frac{e^2}{2\pi m_e c} \frac{1}{f^2} \int_0^d n_e dl \equiv \mathcal{D} \times \frac{\mathrm{DM}}{f^2} \qquad (2.14)$$
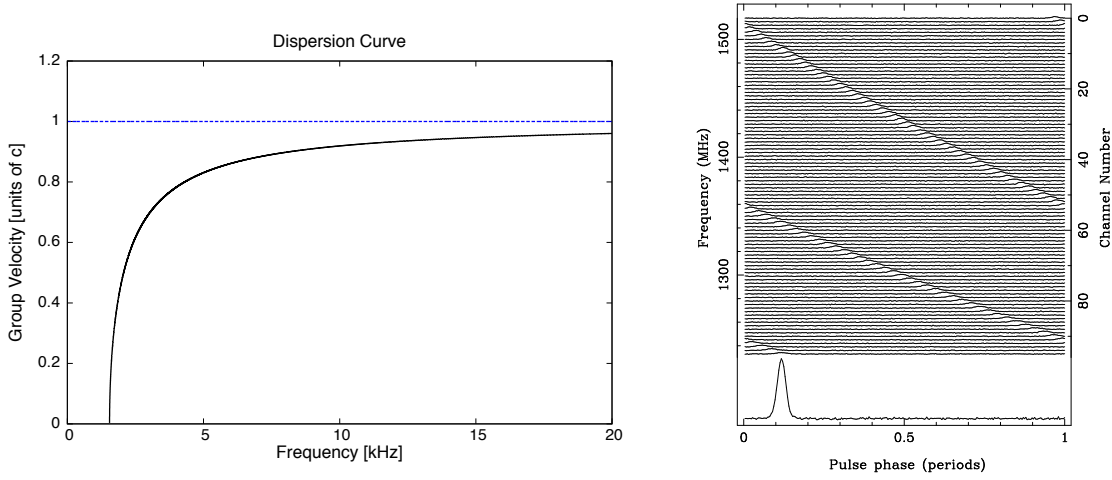
(a) An example of the dispersion relation with $f_p \simeq 1.55$ kHz. This value is typical in the case of the Galactic ISM [35]. Radio waves at frequencies below this threshold would be absorbed by the propagation medium.

(b) Effect of dispersion on the signal of PSR B1356-60. On the top panel of the picture is visible the anticipation of the pulse at higher frequencies. On the bottom is the de-dispersed pulse profile. Credits: Andrew Lyne.

Figure 2.1

Here two quantities have been introduced. $\mathcal{D}$ is called the *dispersion constant* and it is a numerical factor that depends only on constants:

$$\mathcal{D} = \frac{e^2}{2\pi m_e c} \simeq 4.15 \times 10^3 \text{ MHz}^2 \text{ pc}^{-1} \text{ cm}^3 \text{ s} \tag{2.15}$$

More importantly, DM is said to be the *dispersion measure*:

$$\text{DM} = \int_0^d n_e dl \tag{2.16}$$

As we will see, it turns out to be one the most relevant quantities in all pulsar observational techniques.

Since the electron density is in general a function of the point, if we know the electron distribution along our line of sight, we can evaluate the distance of the source by measuring the delays in the arrival times of the pulses. We can do so by observing at two different frequencies, f_1 and f_2, and then measuring the delay between the arrival times of the two signals, that will be:

$$\Delta t_{(f_1, f_2)} = \frac{e^2}{2\pi m_e c} \cdot \left(\frac{1}{f_1^2} - \frac{1}{f_2^2} \right) \cdot \text{DM} \tag{2.17}$$

Once we compute the DM we can integrate eq. (2.16) to then obtain the distance of the pulsar, d. It is worth noticing that also the converse is true: if we know the distance, we can infer the average electron density distribution along the line of sight.

2.1.2 Faraday rotation

The same frequency dependance of the propagation velocity that is responsible for the dispersion also causes a phase shift between the right-handed and left-handed circular polarization components, in the presence of a cold, magnetized plasma. Let us consider a uniform magnetic field, namely $\vec{B} = B_0\hat{z}$ (where $\hat{z}$ is the unit vector of our z-axis), and a circularly polarized electromagnetic wave propagating along the direction of $\vec{B}$; its electric field is:

$$\vec{E}(t) = E_0(\hat{\epsilon}_1 \pm \hat{\epsilon}_2)e^{i(\vec{k}\cdot\vec{x}-\omega t)} \tag{2.18}$$

Here we have expressed the electric field with the orthogonal unit vectors of the two linear polarizations, $\hat{\epsilon}_1, \hat{\epsilon}_2$, since any circular polarization can be seen as a linear combination of them. The '+' and '−' signs are for left- and right-handed circularly polarized waves, respectively. The same Maxwell's equations as those of the previous section still hold, but now we must add the Lorentz force in the equation of motion (2.1) of the charge:

$$\vec{F} = -e\vec{E} - e\frac{\vec{v}}{c} \times \vec{B} \qquad \Rightarrow \qquad \vec{v}(t) = -\frac{ie}{(\omega \pm \omega_c)m_e}\vec{E}(t) \tag{2.19}$$

where we have introduced the *Larmor* (or *cyclotron*) *pulsation*, $\omega_c = eB_0/m_e c$. Again, the *Larmor frequency* is simply $f_c = \omega_c/2\pi$.

It is evident from eq. (2.19) that there is a difference between the two left-handed and right-handed circular components of the wave, because the electron has its own direction of rotation in the magnetized medium. By analogous considerations to the case of dispersion, it is straightforward to prove that the propagation velocities of the two circular components are different. As a result, in a distance d, a radiation of frequency f undergoes a relative phase shift of:

$$\Delta\Phi = -k(f)d \tag{2.20}$$

where the wave numbers for the two polarizations are:

$$k(f)_{\pm} = \frac{2\pi}{c}f\sqrt{1 - \frac{f_p^2}{f^2} \mp \frac{f_p^2 f_c}{f^3}} \tag{2.21}$$

Considering the reasonable approximations induced by the conditions $f \gg f_p$ and $f \gg f_c$, it is straightforward to find the general expression of the difference between the rotations undergone by the two circular components, that is:

$$\Delta\Psi_F = \int_0^d (k_+ - k_-)dl \simeq \frac{e^3}{\pi m_e^2 c^2 f^2}\int_0^d n_e B_{\parallel}dl \tag{2.22}$$

where $B_{\parallel}$ is the projection of the magnetic field along the propagation direction of the wave. The observable effect is the rotation of the position angle (defined in eq. 1.8) of the linear polarization, by the amount of half the angle above calculated:

$$\Delta\Psi = \frac{1}{2}\Delta\Psi_F \equiv \lambda^2 \times \mathrm{RM} \tag{2.23}$$

where we have introduced the *rotation measure*, RM:

$$\mathrm{RM} \doteq \frac{e^3}{2\pi m_e^2 c^4}\int_0^d n_e B_{\parallel}dl \tag{2.24}$$

2.1.3 Scintillation

Not only is the ISM magnetized and ionized, but also turbulent and inhomogeneous. This cause the observed intensity to significantly vary on different timescales and frequency bands. This phenomenon is called *scintillation*. We can think of the ISM scintillation as the Galactic counterpart of what happens on Earth: as stars twinkle because of the atmosphere turbulences, so do pulsars because of ISM turbulences.

2.1.4 Scattering

The inhomogeneity of the ISM produces another important effect. Density irregularities in the medium make rays scatter, letting them reach the observer after a longer optical paths, which translate in delays in the times of arrival of those rays. For simple statistical reasons, most of the rays will travel to the observer in fairly straight optical paths, whereas some others will be first scattered once or more times before getting to destination. The pulse will thus appear broadened by a tail that can approximately be fitted by an exponential with a time constant, τ_s, called *scattering time*. Obviously, the more distant the pulsar, the more evident the phenomenon. Since it is a scattering process, it also strongly depends on the frequency, as can be seen in Figure 2.2. It is a common practice that of measuring τ_s at various wavelengths in order to obtain precious information about the ISM itself and its turbulent structure.
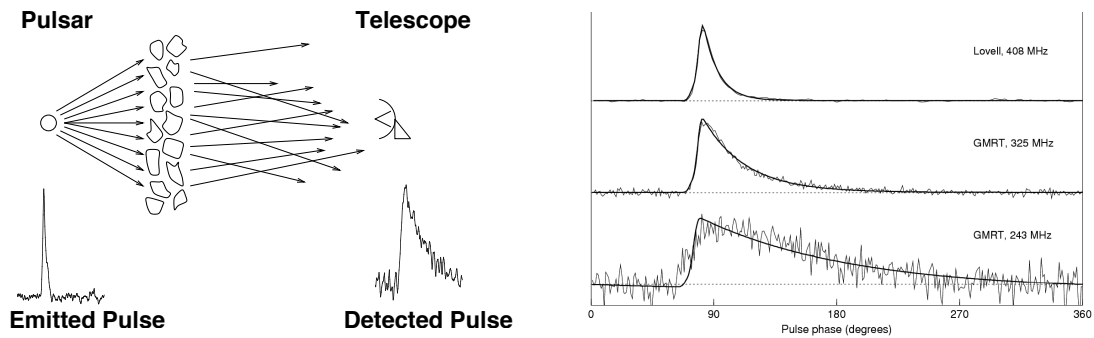
(a) Schematic representation of the scattering effect due to the ISM. Credits: [34].

(b) Frequency dependance of the scattering effect.

Figure 2.2

2.2 Timing

Basically, the idea behind timing is simple: exploit the high rotational rate and stability of pulsars to measure the times of arrival of their pulses and then satisfactorily match them to the expected values given by a theoretical "model". The parameters on which this model is based give insights on the properties of pulsars and its environment. However, in doing so, a lot complications emerge, both theoretical and practical.

We can first summarize the logical steps necessary to perform timing.

- Signal detection and dedispersion.

- Folding.

- Cross correlation and TOA extraction.

- Fit of TOA residuals and parameters estimations.
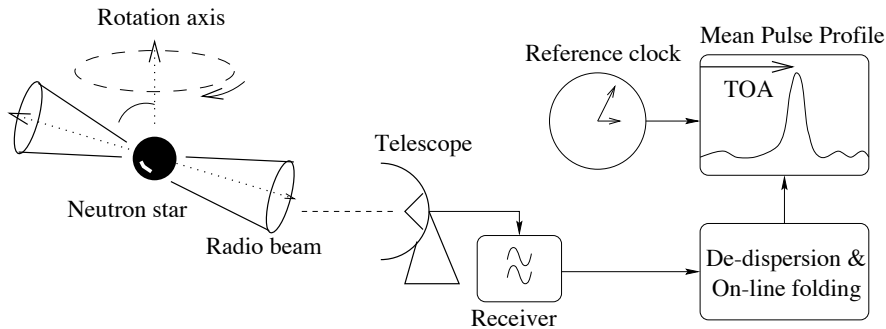
Figure 2.3: Summarizing scheme of the timing procedure. Credits: [35].

2.2.1 Signal detection and dedispersion

A radio telescope, like the 64-meter single dish in Parkes or the upcoming Sardinia Radio Telescope (SRT), is capable of tracking a source and collecting its radiation for a certain time, T_{obs}. Depending on the receiver and the back-end used, the telescope has its own sensitive band. Normally this latter is divided into many different sub-channels; for example it is common to have a 256-MHz band divided into 512 channels, each 0.5-MHz wide. From each of them one gets a *time series* of the source signal, i.e. the radio flux density at the central frequency of the channel as a function of time. For the reasons we treated in Section 2.1.1, the signals in the different channels have different propagation velocities through the ISM and that results in delays in the times of arrival of the pulses at decreasing frequencies (Figure 2.4).
This effect is clearly visible when a new pulsar is discovered; the pulse shift is evident throughout the band (Figure 2.1b). We also remarked the fact that pulsars are weak sources so that it could be a good idea to sum all the channels and obtain a unique time series with a higher S/N. If we did so without caring about dispersion, we would get a time series in which the pulses are much broader than they were in the single channels; this
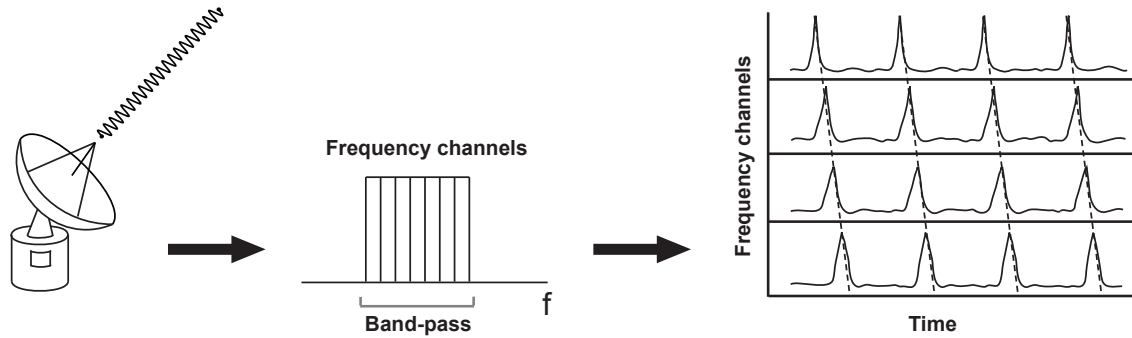
Figure 2.4: A radio telescope collects the pulsar radiation over a wide band, which is in turn split into a number of channels. From each of them, one gets a time series. This allows to drastically reduce the effects of dispersion in every single channel, since the electromagnetic wave looks quasi-monochromatic.

happens because the original signals in the different channels are not aligned in time. The solution is the so-called *dedispersion*, i.e. a procedure (nowadays carried out via software) by which appropriate time delays are applied to each channel in order to compensate the anticipation of the higher-frequency time series.

Note that this process, even if in theory able to remove the dispersion effect completely, is intrinsically limited by the width of the individual frequency channels, in which a small dispersion delay is retained. Other technical approaches (i.e. *coherent dedispersion*, in which the dispersion effect is removed before the detection) can solve this issue completely.

2.2.2   Folding

The main goals of this step are essentially two:

- Increasing the signal-to-noise ratio.

- Getting an integrated profile, which is stable in time and represents the very finger-print of the specific pulsar.

Once the data is dedispersed with a proper DM guess, we have got rid of any inconvenient possible future pulse smearing when summing different channels. The following step is to split the time series of each channel into many "single" pulses of the width of the guessed spin period P and then sum them together. If the period guess is correct, we will finally have an "averaged" or "integrated" profile, boasting a higher S/N, that represents the average emission of the pulsar over the time interval in which the folding has been done (Figure 2.5) at the particular central frequency of the considered channel. If it is not, similarly to the case of dispersion, the single summed pulses will drift along the period linearly with time. In particular, when the period guess is slightly longer than the real one, we will see an anticipation of the pulse over the next rotations (Figure 2.6). Conversely, a shorter period guess will lead to a delay of the pulse along the period over time. In both cases the resulting integrated profile will look broader and the S/N lower than expected.

Clearly, in order to perform the folding, we need to know the precise value of P; however, we know that for various reasons (spin-down, orbital motion ecc.) it varies all along. Thus, we would certainly have a broadening of the pulse also if we folded a long time series with a constant period, even if the value of this latter was exactly the real one at the considered epoch. The remedy to this issue is to not do the folding over the whole time series, but rather in much shorter portions (called *sub-integrations*) of it, where we are allowed to regard P as constant with a high degree of accuracy.
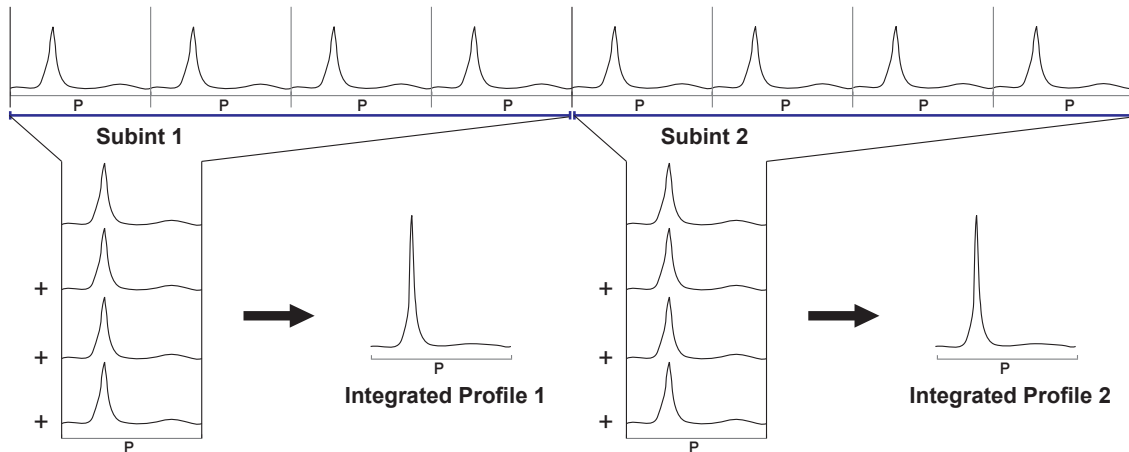
Figure 2.5: When the folding is done properly, the resulting integrated profile shows a very sharp pulse, which is stable in phase in all the sub-integrations. The S/N is much higher than that of a pulse.
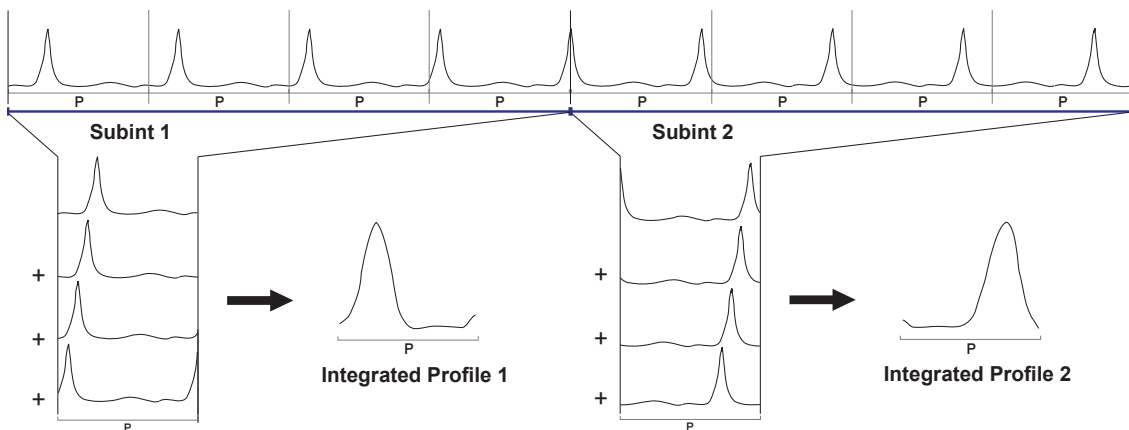
Figure 2.6: The result of folding a time series with a wrong (in this case, longer) period guess. The integrated profiles get broader and the pulse itself shifts along the period from a sub-integration to another.
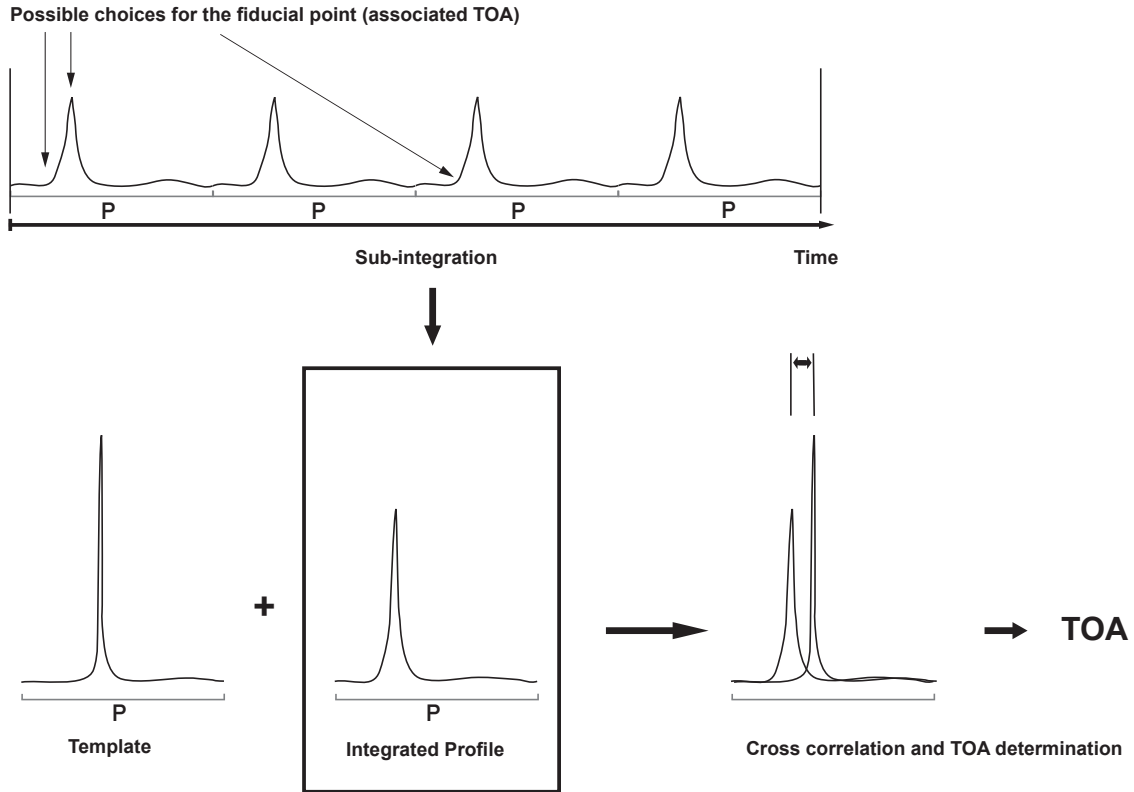
Figure 2.7: Determination of the time of arrival (TOA) associated with an integrated (folded) pulse profile. The latter is cross-correlated with a very high-S/N reference profile and from that the TOA is then extracted.

2.2.3   Cross correlation and TOA extraction

For the integrated profiles of each sub-integration, we would like to associate a time of arrival (TOA) which we can define as the arrival time of some fiducial point on the integrated profile with respect to either the start or the midpoint of the observation. In order to do that, we perform the *cross-correlation*, i.e. a convolution between the integrated pulse profile and a "template" profile, which is a very high S/N profile obtained from the addition of many observations at the particular observing frequency.
Thanks to the cross-correlation operation, which is carried out with the help of some reference atomic clock, the uncertainty associated with the TOA is much smaller than the sampling period.

2.2.4   The timing formula and determination of the TOA residuals

We know that the pulsar period, even if mostly stable, actually changes over time. Since we do not know the real mechanisms which drive its variation and, in addition, this latter is normally very small, the best thing we can do is expanding[1] the spin period P (or, as

---

[1]Note that in this form the expansion does not take into account possible period glitches.

we are going to do, the spin frequency $\nu = 1/P$) as a Taylor series:

$$\nu(t) = \nu_0 + \dot{\nu}_0(t - t_0) + \frac{1}{2}\ddot{\nu}_0(t - t_0)^2 + \dots \tag{2.25}$$

Here t_0 is a certain reference epoch, and $\nu_0, \dot{\nu}_0, \ddot{\nu}_0$ are the spin frequency, its first[2] and second derivative, respectively, as measured at that time. Normally, $\ddot{\nu}_0$ is extremely small and only in a very few pulsar we are able to observe it. Eq. (2.25) represents our theoretical model with which we would like to make predictions. In its explicit expression, a lot of physical parameters are present; if we knew all such parameters with infinite precision, we could count the number of pulses $N(t)$ we expect to observe after any time t. Indeed, integrating, we have:

$$N(t) = N_0 + \nu_0(t - t_0) + \frac{1}{2}\dot{\nu}_0(t - t_0)^2 + \frac{1}{6}\ddot{\nu}_0(t - t_0)^3 + \dots \tag{2.26}$$

where now N_0 is the pulse number at the reference epoch.

It is important to remark that these formulas are referred to the inertial rest frame of the pulsar. It is well known, however, that our observing frame of reference (topocentric reference) is not inertial. This is primarily caused by the rotation of the Earth about its spin-axis and its motion along its orbit around the Solar System barycenter. On the contrary, despite its revolution motion around the center of the Galaxy, we can consider the Solar System Barycenter (SSB) as an inertial frame to a very good approximation, at least for our initial purposes. Deviations effects due to the fault of this assumption, could instead be visible in some finer observables.

For the above reasons, it is far simpler to study the arrival times in the SSB instead of the topocentric reference, i.e. instead of our laboratory. We thus need to make a transformation from one frame to the other, which we can express by the following equation:

$$t_{\text{SSB}} = t_{\text{obs}} - \Delta_{\text{DM}} + \Delta_{\text{R}\odot} - \Delta_{\text{S}\odot} + \Delta_{\text{E}\odot} \tag{2.27}$$

To better understand its meaning, we explain each term. Here t_{obs} is simply the arrival time as revealed by the telescope, whereas Δ_{DM} is the delay induced by dispersion. The last three terms are instead called *barycentric corrections* for they are actually the ones responsible for the transformation from the topocentric frame to the SSB.

Dispersion delay: Δ_{DM} From what we have learnt from Section 2.1.1 we know that the presence of plasma in the ISM makes the light travel slower at decreasing frequencies. We then include this effect straightforwardly, remembering the inverse-square dependance on the frequency.

$$\Delta_{\text{DM}} = \mathcal{D} \cdot \frac{\text{DM}}{f^2} \tag{2.28}$$

Even if here we do not concern about the actual stability of the dispersion measure, it has been observed in several cases that it could actually be a function of time and the correction would need some modification to take it into account, including the first DM derivatives. The reasons can be related either to ISM turbulences or to the presence of a gas cloud in the vicinity of the pulsar, like in the systems we are going to introduce in the next chapter.

---

[2]The first derivative is also often referred to as the pulsar *spin-down*.

Römer delay: $\Delta_{\mathbf{R}\odot}$ It is the correction that takes into account the additional travel time of light between the position of the telescope and the SSB. The different optical path that light must travel with respect to the barycenter during the revolution of the Earth around the Sun, implies a changes in the time taken to reach the observer, i.e. the phase center of the telescope. We denote by $\hat{s}$ the unit vector pointing from the SSB to the pulsar, and by $\vec{r}$ the vector from the former to the observer, which in turn we can write as $\vec{r} = \vec{r}_{\mathrm{SSB}} + \vec{r}_{EO}$, where the first connects the SSB to the center of the Earth and the second connects this latter to the observer. In this way, we can write:

$$\Delta_{\mathrm{R}\odot} = -\frac{1}{c}\vec{r} \cdot \vec{s} = -\frac{1}{c}(\vec{r}_{\mathrm{SSB}} + \vec{r}_{\mathrm{EO}}) \cdot \vec{s} \tag{2.29}$$

Just to have an idea of the expected trend and periodicity of the time residuals due to this effect, we can ignore the linear dimensions of the Earth (which play a much smaller role) and consider only the first scalar product of the right-hand side of eq. (2.29). Explicitly, we can express it as:

$$\frac{1}{c}\vec{r}_{\mathrm{SSB}} \cdot \vec{s} = \frac{d_{\oplus}}{c}\cos\beta\cos(\Omega_{\mathrm{r}}t - \lambda) \tag{2.30}$$

where $d_{\oplus} = 1$ AU is the average distance of the Earth from the Sun, β and λ are the ecliptic latitude and longitude, respectively, and Ω_{r} is the average revolution angular velocity[3]. Under this assumptions, it is straightforward to understand that the expected modulation in the residuals has a period of 1 year, its magnitude is maximum if the pulsar is in the ecliptic plane, $\beta = 0$, and vanishes if $\beta = \pm 90°$.

Note also that the Römer delay is a completely classical effect.

Shapiro delay: $\Delta_{\mathbf{S}\odot}$ It accounts for the general relativistic corrections due to the curvature of space-time. We know that every massive body causes space-time to warp. This makes the light travel a longer optical path with respect to a perfectly flat space-time. The most important contributors, in our case, are the Sun and Jupiter but, to be precise, we must sum over all the celestial bodies of the Solar System. Starting from the general relativistic metric in the weak-field approximation, one can show that it is possible to write the delay as:

$$\Delta_{\mathrm{S}\odot} = -2\sum_i \frac{GM_i}{c^3}\ln\left(\frac{\hat{s}\cdot\vec{r}_i^{\oplus} + |\vec{r}_i^{\oplus}|}{\hat{s}\cdot\vec{r}_i^{P} + |\vec{r}_i^{P}|}\right) \tag{2.31}$$

where G is the universal gravitational constant, M_i is the mass of the i-th body, $\vec{r}_i^{P}$ is the pulsar position with respect to it and $\vec{r}_i^{\oplus}$ is the vector that connects the observatory to the i-th body when the photon is at its minimum distance from the latter.

Einstein delay: $\Delta_{\mathbf{E}\odot}$ It embodies both the effect of gravitational redshift due to the presence of massive bodies in the Solar System and the effect of time dilation due to the relative motion of the Earth with respect to the pulsar. Römer and Shapiro are delays that acts in the *coordinate time*, t, though the measures are made in the

---

[3]It is clear that in cosidering the Earth's orbit as circular (which implies $d_{\oplus} = $ const, $\Omega_{\mathrm{r}} = $ const) we have made another approximation. The non-zero eccentricity of the orbit would, in reality, give rise to an additional modulation of the signal even if of tiny magnitude.

rest frame of the observatory, whose clock has its own proper time, τ. Again it can be shown [13], by simple general relativistic calculation in a Schwarzschild metric, that the Einstein delay is:

$$\Delta_{\mathrm{E}\odot} = t - \tau = \int^t dt' \left[\sum_{i \neq \mathrm{Earth}} \frac{GM_i}{c^2 |\vec{r}_i^{\oplus}|} + \frac{v_{\oplus}^2}{2c^2} \right] \tag{2.32}$$

This time the sum is performed over all the bodies but the Earth, whose velocity relative to Sun is $v_{\oplus}^2$ and its magnitude is a function of time if we take into account the eccentricity of the orbit.

There are some other minor effects that should be included in the timing formula, but we will neglect them (at least in explaining them theoretically) for brevity.

2.2.5 Best-fit of TOA residuals and parameters estimation

What we need to perform the transformation from the topocentric to the barycentric reference, as well as to correct for the pulse period variations over time and so on, is included in the *ephemeris* of the particular source. This is essentially a "table" containing all the positional, rotational, kinetic and (possibly) orbital information we know about the considered object; in other words, the ephemeris contains all the parameters involved in our timing model.

From the observational data of our source, we get the times of arrival of its pulses. Finding a timing solution means "connecting" all the pulses of the source with a definite phase-coherent timing model, whose parameters have to be found. If the model is actually correct, it will allow us to count all the pulses occurring in any specific interval of time. More importantly, we will also have a very accurate estimate for the physical parameters that were involved in that timing model.

The way by which the timing solution can be found is through a least-squares fit to the TOA residuals. Formally, what we have to do is minimizing the following variable:

$$\chi^2 = \sum_i \left(\frac{N(t_i) - n_i}{\sigma_i} \right)^2 \tag{2.33}$$

where n_i is the nearest integer to the pulse number $N(t_i)$ predicted by the model at the time t_i of a given TOA, and σ_i is the TOA uncertainty in units of the pulse period.

If the fit is done correctly accounting for all the involved parameters, the post-fit TOA residuals will be Gaussian-distributed around zero, with a root mean square of the order of the TOA uncertainties (Figure 2.8). The uncertainties on the estimated parameters will depend on the fitting algorithm and will in general decrease with the length of the data span, as well as with the orbital coverage in the case of binary systems.
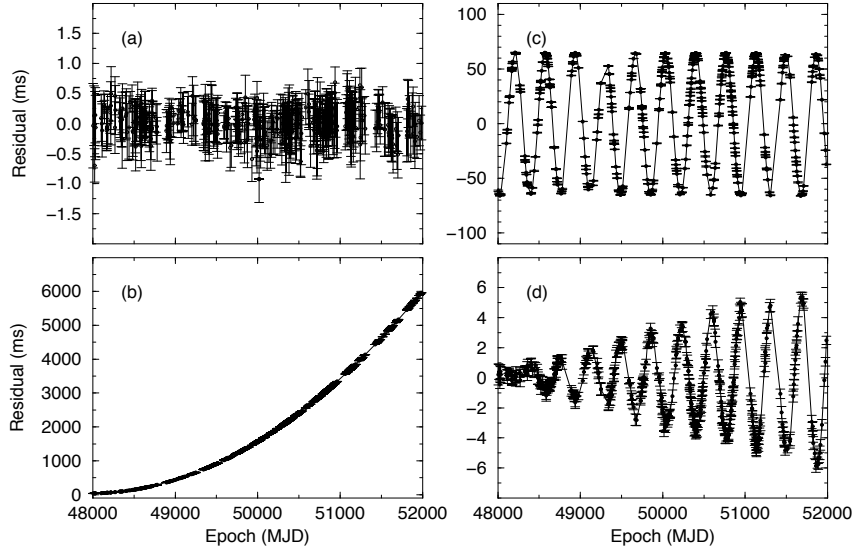
Figure 2.8: Post-fit residuals in the case of: a) a correct estimation of all the involved parameters; b) an underestimated spin period derivative; c) an error in the estimation of the position; d) neglecting the proper motion of the source. Credits: Michael Kramer.

2.3   Timing binary systems

When studying a binary system, a number of other effects must be included. The motion of the two star around their common center of mass induces new modulations to the arrival times of the pulses and thus to the TOA residuals. Formally, we need to add four new contributions to eq. (2.27), which becomes:

$$t_{\mathrm{SSB}} = t_{\mathrm{obs}} - \Delta_{\mathrm{DM}} + \Delta_{\mathrm{R}\odot} - \Delta_{\mathrm{S}\odot} + \Delta_{\mathrm{E}\odot} + [\Delta_{\mathrm{RB}} + \Delta_{\mathrm{SB}} + \Delta_{\mathrm{EB}} + \Delta_{\mathrm{AB}}] \qquad (2.34)$$

The first three terms in the square brackets are just the same Römer, Shapiro and Einstein delays as above, with the only difference that they are applied to the binary system. The last term, instead, takes into account aberration effects due to the orbital motion.

2.3.1   Keplerian orbits

Even though we are including relativistic effects in calculating the delays, there is often no need to describe the orbits of a binary system in a general-relativistic picture. For non-relativistic binaries, like those we will study in the next chapters, we can simply treat the orbits as Keplerian. That means, for example, that they are actually closed and we only need seven parameters to completely describe the dynamics of the binary. Such parameters are:

- P_b: the orbital period.

- a_p: the semi-major axis of the orbit of the pulsar.

- i: the inclination of the system, i.e. the angle between the line of sight and the normal to the orbital plane.
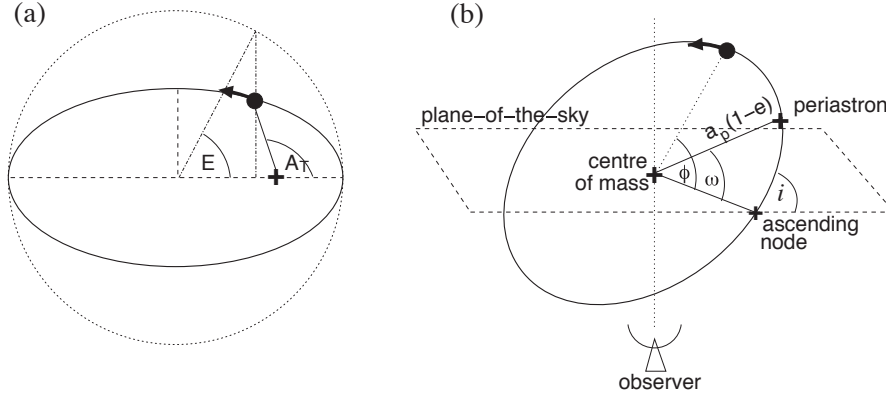
Figure 2.9: Principal parameters used to describe the position of a body in a general elliptic orbit in a binary system. Credits: [35].

- e: the orbital eccentricity.

- Ω_{asc}: the angle between the line of nodes of the orbit and an assumed direction in the sky.

- ω: the periastron longitude, as measured from the ascending node.

- T_0: the epoch of periastron passage.

In the case of pulsar timing we are only able to measure 5 parameters, namely P_b, e, ω, T_0 and the combination $a_p \sin i$, that is the projection of the semi-major axis of the pulsar orbit along the line of sight. A visual representation of the above quantities can be seen in Figure 2.9b.

Recall now that the motion of a body in an elliptical orbit can be described by three different angles, namely the *true anomaly* A_T, the *eccentric anomaly* E and the *mean anomaly* $\mathcal{M}$.
The first is determined by the line connecting one focus to the position on the orbit. The second one is instead specified by the line connecting the geometrical center of the ellipse to the intersection of the auxiliary circle of radius the semi-major axis of the ellipse with the line normal to this latter and passing through the real position of the massive body (Figure 2.9a). The third one is a sort of average of the two based on the fact that equal areas are swept at the focus in equal intervals of time (2nd Kepler's law); for this reason, the mean anomaly has the important property of growing linearly with time in non-relativistic orbits, no matter the value of their eccentricity. The main relations among the three are the following:

$$\mathcal{M} = E - e \sin E \tag{2.35}$$

$$E = \arccos\left(\frac{\cos A_T - e}{1 - e \cos A_T}\right) \tag{2.36}$$

While the passage from the true anomaly to the mean anomaly can be achieved straightforwardly, the opposite has no closed-form solutions and must be performed numerically.

Let us call $a = a_p + a_c$ the *orbital separation* of the system (where a_c is the semi-major axis of the companion's orbit), and M_p, M_c the mass of the pulsar and of the companion, respectively. By definition of center of mass, we know that $M_c\,a_c = M_p\,a_p$ and the semi-major axes of the two orbits can be computed as follows:

$$a_p = a\,\frac{M_c}{M_p + M_c} \tag{2.37}$$

$$a_c = a\,\frac{M_p}{M_p + M_c} \tag{2.38}$$

Now, combining Kepler's third law, $P_b^2 = 4\pi^2 a^3 / G(M_p + M_c)$ and the definition of projected semi-major axis of the pulsar orbit, $x \doteq a_p \sin i$, one can define the so-called *mass function* of the pulsar:

$$f(M_p) = \frac{4\pi^2}{G}\,\frac{x^3}{P_b^2} = \frac{(M_c \sin i)^3}{(M_p + M_c)^2} \tag{2.39}$$

The importance of such a function resides in the fact that it is an easily-measurable quantity, for it depends only on the orbital period and the projected semi-major axis of the pulsar orbit. From the mass function one can estimate the companion's mass, once the pulsar mass and the inclination are set. While the former has a quite narrow range ($M_p = 1 \div 2.5\ \mathrm{M_\odot}$), the latter is more difficult to infer. Usually one has to settle for an estimated companion mass and orbital separation as a function of the inclination (normally after conventionally setting $M_p = 1.4\ \mathrm{M_\odot}$). Formally, from the three equations:

$$\begin{cases} f(M_p) = (M_c \sin i)^3 / (M_p + M_c)^2 \\ M_c\,a_c = M_p\,a_p \\ x = a_p \sin i \end{cases} \tag{2.40}$$

we get:

$$a(i) = a_c(i) + a_p(i) = \left(\frac{M_p}{M_c(i)} + 1\right)\frac{x}{\sin i} \tag{2.41}$$

Even without knowing the inclination, the mass function is also helpful to give a lower limit to the mass of the companion:

$$f(M_p) = \frac{M_c}{\left(\frac{M_p}{M_c} + 1\right)^2}\sin^3 i < M_c \sin^3 i \qquad \Rightarrow \qquad M_c > \frac{f(M_p)}{\sin^3 i} \tag{2.42}$$

The value obtained for $i = 90°$ represents the lower limit for M_c.

Chapter 3

Eclipsing binary pulsars

After reviewing the main characteristics of pulsars, we now move to the particular kind we are going to focus on.

We have seen that all millisecond pulsars must stem from binary systems, in which main sequence companions let them accrete matter and then spin up. A remarkable fact is that some of them show long regular eclipses in their signal that last for a relatively large fraction of their orbital period. At first one could be induced to justify it by saying that they are due to the size of the companion which hides the pulsar once per revolution. Nonetheless, for many of them, that could not be the case: looking at data one soon realizes that the occultation area is by far larger than the Roche lobe of the companion star. So, it cannot be the star itself to keep the pulsar out of sight. There must be another explanation.

Another piece of the puzzle is represented by the observation of isolated millisecond pulsars which, in the simple evolutionary scenario described in the previous chapters, should not exist. Hence, this kind of objects were likely binary systems in origin and some mechanism must have come into play to make the companion disappear.

The very beginning of the study of eclipsing binary systems was the discovery of PSR B1957+20, in 1987. After that, another handful of similar sources have been spotted [20] and what came out is the topic of this chapter.

3.1 Black Widow Pulsars and Redbacks: an overview

The first two parts of Table 3.1 (labelled "Old BWPs" and "New BWPs") and the first part of Table 3.2, list a series of pulsars. Some common traits emerge from the observations that have been made for such objects:

- They tend to show radio eclipses[1] with the same repetition period as the orbital one. The duration of the eclipses depends on the frequency, often following a power-law.

- They all have very tight, nearly circular orbits with orbital periods of a few hours.

---

[1]Note also that, whether a system does show eclipses or not, strongly depends on the inclination angle.

- They have very small mass functions. In almost all cases, the companion mass is very likely less than a tenth of a solar mass ($M_c \lesssim 0.1$ M$_\odot$).

- They show spin periods of the order of milliseconds, thus belonging to the class of *fully-recycled* pulsars.

- Most of them were initially found in globular clusters (now the situation is rapidly changing), and that gave some clues about their possible formation. The panorama is going to get more complicated as a wealth of discoveries of eclipsing binaries in the Galactic plane are now occurring.

The features described above are very similar to those we presented in the case of VLXBs. Clearly, this is not by chance. All the eclipsing binary pulsars belong to the class of Very Low-Mass Binary Pulsars (VLMBPs) or "Black Widow Pulsars" (BWPs)[20], a term by which we denote the next evolutionary phase of VLXBs, once the accretion has stopped. Black Widow Pulsars are so called because of their main feature, i.e. the ongoing ablation of the companion: just like female black widow spiders kill their partner after mating, so do such pulsars with their companions after being spun up through recycling. It is worth remarking that not all VLMBPs actually show eclipses. Those which do not, exhibit mass functions as low as $f(M_p) = 10^{-5}$ M$_\odot$ while eclipsing binaries (ELMBPs) always have $f(M_p) \gtrsim 3 \cdot 10^{-4}$ M$_\odot$. Since many other characteristics (like short orbital periods, millisecond spin periods etc.) are common to both subclasses, it has been proposed [20] that the correlation between very small mass functions and the lack of eclipses could be explained in terms of the inclination. In fact, the most-widely accepted picture is that of a gas cloud spilling off the companion provoking the signal obscuration. Hence, at high values of the inclination ($i \simeq 90°$) the system is seen nearly edge-on and thus eclipses are very likely to be visible; conversely, lower i's translate into looking at the system nearly face-one, making the interception of the cloud by our line of sight less probable. On the other hand, we can recall eq. (2.39) and see that the mass function is proportional to $\sin^3 i$: the lower values of $f(M_p)$ observed in the latter class of systems are thus compatible with the explanation we gave above.

In the lower parts of Table 3.1 and Table 3.2 we instead have other sources which differentiate from the previous ones for some features among which the most important are:

- Higher values for the mass functions and, hence, for the most probable masses of the companions, namely $M_c \gtrsim 0.1 \div 0.2$ M$_\odot$.

- Longer orbital periods with values of ~ 8.8 h on average.

Table 3.1: List of known Black Widow Pulsars and Redbacks in the Galactic Field as of 2012. The "F" indicates that the pulsar is also a γ-ray Fermi source. Credits: [27].

	Name	P_0 [ms]	$L_p[10^{34}$ erg/s]	d (NE2001) [kpc]	P_b [hrs]	Minimum M_c [M$_\odot$]	Category
Old BWPs	B1957+20 F	1.61	11	2.5	9.2	0.021	BWP
	J0610-2100 F	3.86	0.23	3.5	6.9	0.025	BWP
	J2051-0827	4.51	0.53	1.0	2.4	0.027	BWP
New BWPs	J2241-5236 F	2.19	2.5	0.5	3.4	0.012	BWP
	J2214+3000 F	3.12	1.9	3.6	10.0	0.014	BWP
	J1745+1017 F	2.65	1.3	1.3	17.5	0.014	BWP
	J2234+0944 F	3.63	1.6	1.0	10	0.015	BWP
	J0023+0923 F	3.05	1.6	0.7	3.3	0.016	BWP
	J1544+4937 F	2.16	1.2	1.2	2.8	0.018	BWP
	J1446-4701 F	2.19	3.8	1.5	6.7	0.0019	BWP
	J1301+08 F	1.84	6.7	0.7	6.5	0.024	BWP
	J1124-3653 F	2.41	1.6	1.7	5.4	0.027	BWP
	J2256-1024 F	2.29	5.2	0.6	5.1	0.034	BWP
	J2047+10 F	4.29	1.0	2.0	3.0	0.035	BWP
	J1731-1847	2.34	7.6	2.5	7.5	0.04	BWP
	J1810+1744 F	1.66	3.9	2.0	3.6	0.044	BWP
New Redbacks	J1628-32 F	3.21	1.8	1.2	5.0	0.16	Redback
	J1816+4510 F	3.19	5.2	2.4	8.7	0.16	Redback
	J1023+0038 F	1.69	~ 5	1.3	4.8	0.24	Redback
	J2215+5135 F	2.61	6.2	3.0	4.2	0.22	Redback
	J1723-28	1.86	?	0.75	14.8	0.24	Redback
	J2129-0429 F	7.61	3.9	0.9	15.2	0.37	Redback

Table 3.2: List of known Black Widow Pulsars and Redbacks in globular clusters as of 2012.

Name	GC, letter	P_0 (ms)	P_b (h)	M_c $(M_\odot)^\dagger$	Date of Discovery	Category
J0023-7203J	47 Tuc J	2.10	2.9	0.024	2000	BWP
J0024-7204O	47 Tuc O	2.64	3.3	0.025	2000	BWP
J0024-7204R	47 Tuc R	3.48	1.5	0.030	2000	BWP
J1518+0204C	NGC 5904	2.48	2.09	0.038	2007	BWP
J1641+3627E	NGC 6205	2.49	2.81	0.02	2007	BWP
J1701-3006E	NGC 6266 E	3.23	3.8	0.035	2003	BWP
J1748-2446O	Ter 5 O	1.68	6.23	0.04	2005	BWP
J1953+1846A	NGC 6838 A	4.89	4.24	0.032	2007	BWP
J1823-3021F	NGC 6624 F	4.85	*	*	2008	-
J0024-7204V	47 Tuc V	4.81	4.8	*	2000	-
J0024-7204W	47 Tuc W	2.35	3.2	0.14	2000	Redback
J1701-3006B	NGC 6266 C	3.59	3.47	0.14	2003	Redback
B1718-19	NGC 6342	1004.04	6.2	0.13	1993	Redback
J1740-5340	NGC 6397	3.5	32.5	0.22	2001	Redback
J1748-2446A^a	Ter 5 A	11.56	1.81	0.10	1990	Redback
J1748-2446P	Ter 5 P	1.73	8.70	0.44	2005	Redback
J1748-2446ad	Ter 5 ad	1.40	26.3	0.16	2006	Redback
J1748-2021D	NGC 6440 D	13.50	6.87	0.14	2008	Redback
J1824-2452H	NGC 6626 H	4.63	10.44	0.20	2008	Redback
J1824-2452I	NGC 6626 I	3.93	11.03	0.20	2008	Redback
J2140-2310A	NGC 7099 A	11.02	4.18	0.11	2004	Redback

^{a} More commonly known as B1744-24A.

† Calculated assuming a pulsar mass of $M_p = 1.35$ $M_\odot$ and an inclination $i = 60°$.

* Parameter is still not well determined: this indicates that there is still no published timing/orbital solution.

3.2 The origin of Black Widow Pulsars and Redbacks

The question about the birth of BWPs has not yet been completely answered. The same is true for isolated millisecond pulsars (like PSR 1937+21) and, as already stated, the two are probably in some way correlated.

As we explained in the previous sections, if a neutron star accretes enough matter to be spun up to frequencies of hundreds of Hz and it may turn on some radio emission, then we have a MSP. If it also has a companion with suitable physical parameters for allowing the process of ablation, we can regard it as a BWP. A lot of ideas have been suggested to justify the very small mass functions of BWPs and, related to that, to guess the nature of their companions. In general we know that, if a pulsar accretes matter, it cannot emit in the radio band, because the radio emission is inhibited by the in-falling matter itself. An accelerated neutron star can appear to us as a radio pulsar only when the process of accretion has stopped; that means, in the case of low-mass systems, that the companion must not be filling its Roche lobe anymore. Thus, the initial thought was that the companion would finally detach from its lobe once its whole envelope has been completely lost and only the core would then remain, so that the star would turn into a white dwarf (WD) made of helium or carbon-oxygen, depending on the initial mass. Though, the hypothesis of WDs as companions is not compatible with the third ingredient needed to make BWPs, i.e. the possibility of being ablated: the surface gravity (GM/c^2R) would be too high and the surface too small to be irradiated enough so that the object could effectively evaporate. As an additional proof in support of this hypothesis, there has never been evidence of any ablation in all the MSP-WD systems so far.

3.2.1 The onset of widowhood

The awkward issue explained above probably had a way out in the occurrence of many more BWPs in globular clusters (GCs, hereafter) rather than in the Galactic field. In fact, until a few years ago, almost all ELMBPs were observed in globulars; that nicely fitted the idea by which such systems should not have formed according to the classical evolutionary scenarios, typical of LMBPs and VLMBPs, which in fact are spotted both in globulars and in the field. Hence, the hypothesis was that there had to be a way through which GCs could produce BWPs. The most straightforward thinking went directly to one of the peculiar features of globular cluster, i.e. dynamical events.

As we know, close encounters are very likely in such crowded systems of stars, and so are gravitational captures and partner exchanges in binaries. The typical scenario that can be seen in any globular cluster is indeed the following: many of the large number of massive main sequence (MS) stars came to the end of their lives very early with respect to the current age of the cluster; after the supernova explosion, most of high-speed isolated neutron stars left the cluster. Some of the lower speed neutron stars instead remained gravitationally bound to the cluster and progressively sank to the center of the cluster due to the mass segregation effect. Finally, in the cluster core, dynamical events could have yoked them with another MS star; this could have in turn filled its Roche lobe and made the system visible as a LMXBs, thanks to accretion processes. The observational incidence of such systems is indeed much higher in globulars rather than in the field, where they can

instead form in this way only from primordial binary systems. In fact, when accretion has stopped and the pulsar has been spun up, the MS star has been by now turned into a white dwarf, so that we have a MSP-WD binary system. Also this system are more abundant in globular clusters than in the Galactic disk (after normalizing to the total mass of the two stellar systems, $\gtrsim 10^3$ times larger for the Galactic disk). Davies & Hansen [12] have also shown that exchange encounters in GCs tend to leave the most massive stars within the binaries, independently of the initial composition of the system. More precisely, when an isolated star (or a component of a binary system) approaches up to less than four times the orbital separation of another binary system, the gravitational forces compel the two to heavily interact. Usually, from a double system, a neutron star encounter will make the less massive star be thrown away and a new binary made of the neutron star and the more massive main sequence star then forms. As the latter evolves and fills its own Roche lobe, the neutron star accretes matter and thus speeds up. According to the mass of the companion, the destiny of the system will then be different [5]. Especially binaries made of a MSP along with a low-mass (i.e. helium) WD are very likely to exchange the latter with a more massive main sequence star, since there are plenty of them in GCs and, as already outlined, it is the less massive object of the system to be flung.

At this point, we can trace the two possible channels [20] through which eclipsing binary pulsars (BWPs) can most likely form in a GC:

- The first one is the case in which previously recycled pulsars (like those of MSP-WDs) set in orbit around a new MS star via companion exchange.

- The second channel is that of an isolated neutron star impinging on a primordial MS binary system.

At birth, the new system will probably be quite eccentric, due to the way it formed. However, tidal forces ensure the final orbit to be almost perfectly circular (i.e. with negligible eccentricity) and this is true both for initially wide ($a \sim 100$ R$_\odot$) and tight ($a \sim 1 \div 10$ R$_\odot$) systems.
The most probable initial mass for the new companion is in between the turn-off mass of the globular cluster (since the probability of capture is an increasing function of mass) and the mass of the most abundant main sequence stars, typically 0.4 M$_\odot$. The turn-off mass of globular clusters is, at present, ~ 0.7 M$_\odot$ on average. Under this picture, we expect the population of rapidly spinning neutron stars in GCs to be hosted in tightly bound, circular binary systems, with companions between ~ 0.4 M$_\odot$ and ~ 0.7 M$_\odot$.

When the millisecond pulsar has a sufficiently strong spin-down radiation it can heat the low mass main sequence companion and generate an induced stellar wind. This holds true especially if the short orbital separation and the relatively large radius of a MS star companion compensate for the usually weak magnetic field of the millisecond pulsar. If the mass-loss rate $\dot{M_c}$ is sufficiently high, the companion can eventually completely evaporate, over a timescale of $\tau_{evap} \sim M_c/\dot{M_c}$, leaving behind an isolated millisecond pulsar. This could represent the connection we cited at the beginning of the section between isolated MSPs and BWPs.

It worth noticing that, from a statistical point of view, anytime there is evidence of ablation, the companion mass turns out to be far lower than the aforementioned turn-off value (Table 3.1). Some calculations [5] show that BWPs are seen as such only when
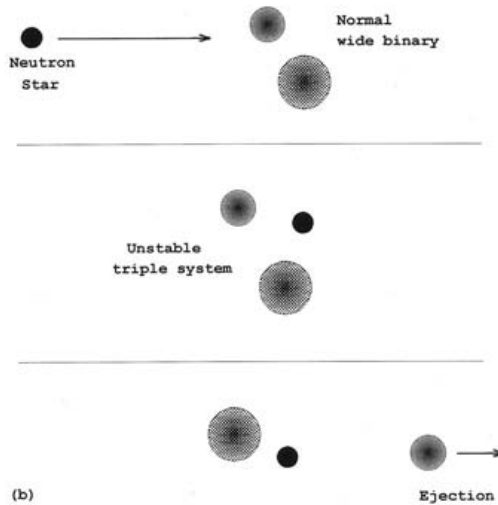
Figure 3.1: Companion exchange for a binary system in a dynamical event.

the mass loss due to the evaporation of the companion is quite low; in fact, in the cases of a strong accretion from the irradiation-driven stellar wind, the pulsar can be totally obscured by the spilled mass itself. For most of the systems, the mass loss is sufficiently slow to make the pulsar visible only when $M_c \lesssim 0.1$ M$_\odot$.

3.2.2   The distinct case of Redbacks

Contrary to what reported above, when the orbital period is not very short, the effect of the ablation by the pulsar flux is strongly reduced and may be even negligible. This holds true for most of the objects belonging to the class of the Redbacks. In fact a new distinction among eclipsing binary pulsars has been recently introduced, according to the mass function (and hence to the companion's mass). Those systems whose companions are of a few hundredths of solar masses must feature low mass-loss rates and are regarded as the very *Black Widow Pulsars*. On the other hand, other systems show more massive companions of a few tenths of solar masses which, whenever an optical identification of them was possible, also resulted to be non-degenerate. Thus, they must experience heavier mass loss, and for this reason, they are interpreted as systems where the nuclear evolution drives the mass transfer. We refer to this new subclass of eclipsing binary pulsars [42] as *Redbacks*, after the Australian "brothers" of Black Widow spiders. The first of such objects was PSR J1740-5340 [38] discovered in 2001 in the globular cluster NGC 6397.

3.2.3   Eclipsing binaries in the field: new discoveries complicate the panorama

The outlined picture of the formation and evolution of black widow pulsars was the most widely accepted in the scientific community.
In support of their production in GCs there were, until 2007, only three BWPs found in the Galactic field, namely PSR B1957+20, PSR J2051-0827 and PSR J0610-2100 (Table

3.1). Given that the probability of close encounters in the field is significantly small, these system were thought to be formed in globulars and, for some reason, then ejected. For instance, a dynamical event could have thrown them away, or their cluster might have disrupted; this was the argumentation given for explaining such unlike cases.

However, in the very recent years, new Galactic surveys made with the 100-meter dish of the Green Bank Telescope (West Virginia) and the 64-meter dish of the Parkes radio telescope (New South Wales, Australia) have been carried out. Their extreme sensitivity (particularly important for systems with short orbital periods, see Section 3.4) has led to the discovery of many new sources in the Galactic field. In addition to this, γ-ray surveys with the Fermi Gamma-ray Space Telescope with its LAT (Large Area Telescope) instrument, contributed to the discovery of a handful of new ones [42]. Thanks to all these discoveries, new studies have flourished in recent years focusing on the evolution of low-mass and very-low-mass binary pulsars (VLMBPs) [49], while a new class of systems (dubbed *ultra low-mass binary pulsars*) is also emerging [25] with companions of ~ 0.001 M$_\odot$, typically an order of magnitude less massive than the companions of VLMBPs.

3.3 Pulsar/stellar wind interaction

A fundamental role in our comprehension of the underlying causes of the eclipses is played by the interaction between the pulsar relativistic wind, powered by the pulsar spin-down energy, and the stellar wind (induced by the pulsar flux or due to the nuclear evolution) coming from the companion. Under the picture by which it is the outflowing matter to be responsible for the partial or total disappearance of the pulsed radio signal, it becomes crucial to try to understand what effects on the evaporating plasma such a process can have. The reciprocal interaction highly influences the properties of the resulting gas cloud which surrounds the star: both the shape and and density profile of the outflow will be in some way affected, and that will in turn reflect on the observed features.

A lot of authors tried to give answers in this regard with analytical or numerical models. Many of them also agree on the basic properties of the resulting physical situation and it is worth reviewing here the most significant proposals.

Rasio et al. [18] first attempted to explain the observational data of PSR 1957+20 with the aid of a simple numerical model. Special care were taken in trying to retrieve the evident asymmetry in the excess time delays at ingress and egress (see Section 3.7 and Figure 3.6). They realized that the only way to get such a behavior was to take into account all the forces present in the system, i.e. gravitational, centrifugal, Coriolis and that of the radiation pressure. In particular the latter two cause the plasma flow to assume a "cometary" shape along the orbit, as their simulations actually show. The shape was obtained treating the particles as following ballistic trajectories after a large number of them had been ejected isotropically from the surface of the companion (whose radius was set to $R_c = 0.15$ R$_\odot$) at a constant rate. The density profile was also calculated numerically point by point by binning the particles. In their work, they remark the fact that, in such a model, the only free parameters were the ejection velocity v_{ejec} at the surface of the star and the constant ratio between the radiation and gravitational forces F_{rad}/F_g acting

on each particle[2]. The result of the simulations for PSR 1957+20 is shown in Figure 3.2a, where a sharp contact discontinuity at the boundary of the cloud is clearly visible. The same method was used by the author to model the eclipses of another important black widow pulsar, PSR 1744-24A, with the parameters adjusted in order to match its observational properties [19]. In this case, the main difference with respect to the previous one was the fact that the ejection of the particles was made occur only from the heated side of the companion. The resulting outflow shape is highly asymmetric and can be seen in Figure 3.2b.
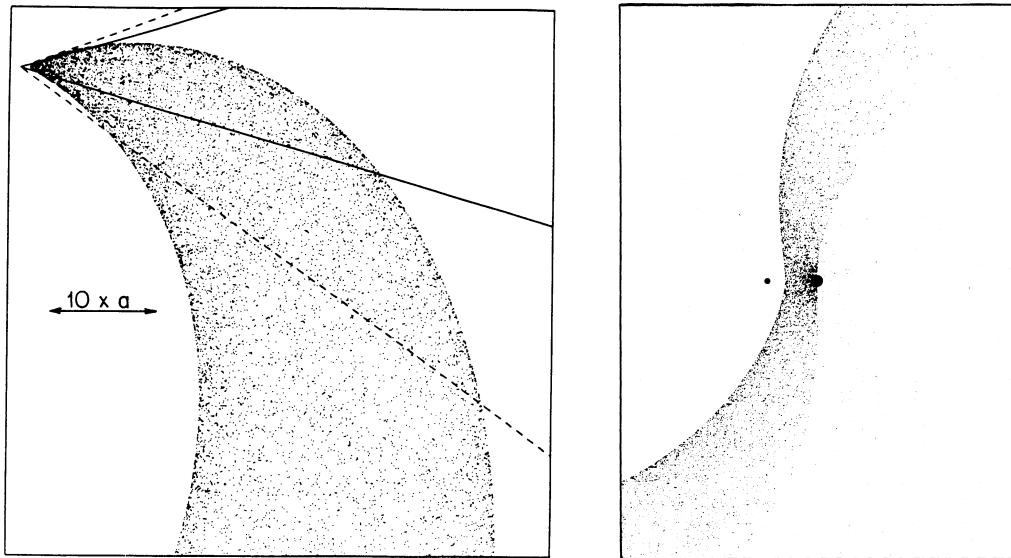
(a) Gas cloud shape as resulted from numerical simulations performed by Rasio et al. [18]. Each dot represents a test particle whose ballistic trajectory has been computed numerically. The two solid lines show the observed positions of the radio eclipses at 430 Mhz in PSR 1957+20. The dashed lines indicate instead the appearance and disappearance of the excess time delays in the same source (see also Figure 3.6).

(b) Similar to (a) but with different parameters values in order to agree with observational data of PSR 1744-24A and with only the heated side of the companion ejecting test particles [19].

Figure 3.2

Bosch-Ramon et al. [53] instead performed relativistic hydrodynamical simulations in two dimensions to study the evolution of shocked stellar and pulsar winds on time scales in which the orbital motion (especially through the Coriolis force) plays an important role. Their results, despite obtained by means of a totally different approach and with many more effects (such mass, momentum and energy exchanges between the pulsar and the stellar wind) taken into account, substantially agree with the approximate bow-shaped shock structure also found by Rasio.

Analytical techniques were rather used by Lipunov and Prokhorov [33] to model the interaction of an *ejecting* pulsar with the matter by which it is surrounded. As explained in their article, a pulsar experiences its *ejector* phase during its lifetime when it is observ-

---

[2]Note that this ratio does not depend on the distance from the center of the companion since both forces scale as r^{-2}.

able in the radio wavelengths also emitting a strong relativistic wind. Even though the ejector phase was introduced for young pulsars, we can investigate the hypothesis that a black widow pulsar is in such a phase. They assumed the principal emission mechanism of the pulsar to be the magneto-dipole radiation (Section 1.3.1), whose produced energy is carried away in the form of low-frequency radiation and relativistic particles with an associated luminosity L_p. In this way, at a distance r, the experienced radiation pressure is $P_{rad} = L_p/4\pi r^2 c$. This latter acts on the surrounding plasma and a surface of pressure balance can then be determined. They found an analytical expression for its boundaries by equating the pressure of the relativistic pulsar wind with the ram pressure of the matter spilling off the companion. In the case of spherical accretion this latter is $P_g = \dot{M}_c v_w/4\pi a^2$, where a is the orbital separation, $\dot{M}_c$ is the mass loss rate of the companion and v_w is the stellar wind speed. In particular, they showed that an open or closed cavern around either the companion or the pulsar, depending on the relative "strength" of the two winds (Figure 3.3a), must form. In the case of black widow pulsars, the stellar wind is induced by the pulsar radiation and thereby we expect its strength to be much lower than that of the pulsar. The cavern will thus form around the companion: if open, the shape of its boundary resembles a paraboloid; if closed, it is very similar to an ellipsoid where the star approximately occupies one focus (Figure 3.3b). Keeping in mind all the limitations of all such simple models, they will anyway be very useful for our successive modeling of the gas cloud shape and density.
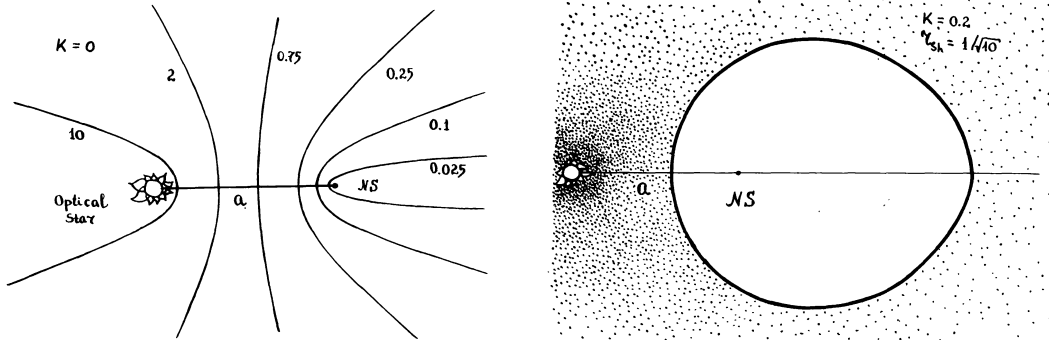
(a) Different boundaries for an open cavern for different values of the *Shvartman radius*, a parameter dependent on both the pulsar luminosity and the stellar wind intensity [33]. Formally, it is defined as $r_{Sh} = \sqrt{L_p/\dot{M}_c v_w}\, c$ with the same meaning for the variables as explained in the text.

(b) Geometry of a closed cavern formed around the NS [33]. A symmetrical situation occurs, with the closed cavern built up around the companion, in the case of a pulsar wind much stronger than that of the star, that is the typical situation occurring in black widow pulsars.

Figure 3.3

3.4 Timing in the presence of eclipses

Particular care must be taken when dealing with data of eclipsing binary pulsars. Soon after the discovery of one of them, the first timing solution is probably very rough. If one, as normally happens, wants to refine the solution, must pay attention to the procedure he follows.

If one proceeds as usual, trying to find a finer timing solution from all the available data

(that is, at all orbital phases) the result will probably be very bad and the timing solution quite far from the real one.

The remedy is to extract the finer timing solution only from residuals relative to off-eclipse pulse TOAs, excluding all the pulse profiles which could probably be affected by the gas cloud. Once the best timing solution has been found, one can use the new ephemeris so obtained to calculate the TOA residuals at *all* the orbital phases where a signal is significantly detected. By convention, the orbital phase is defined to be zero at the pulsar's ascending node. In this way the eclipses are most often centered around the phase of about $\phi = 0.25$, corresponding to the phase at which the pulsar is at the farthermost position with respect to us.

Also, of crucial importance, for eclipsing binaries, is the pulsar signal strength. The more time resolution one has, the more TOA residuals around the eclipse can extract, which in turn allow one to better constrain the physical parameters of the eclipse process. On the other hand, in order to have reliable values for the residuals, the pulse profiles must have a high S/N ratio, which can be increased by folding longer sub-integrations, thus losing time resolution. If a pulsar is intrinsically faint, the only option is to make repeated observations and derive an average behavior of the system during the eclipse event. Obviously, this approach may hide effects occurring only rarely in the succession of the eclipses, but it is often the only possible way of studying these processes.

3.5 Optical counterparts studies

Another powerful tool is the study of the optical light curve. Optical data can tell us precious information about the nature of both the companion and the interaction between the latter and the pulsar. The shape of the curve allows us to make considerations of great relevance only through simple reasoning. For example, a peak at the pulsar inferior conjunction ($\phi = 0.75$, i.e. when the companion's side that faces the pulsar points toward the observer) would suggest that the pulsar is indeed illuminating the star and, thus, probably ablating it. Alternatively, we could see a double peak at the two orbit quadratures ($\phi = 0.0, 0.5$), which can be explained easily if the companion is being deformed by tidal interactions with the neutron star. The ellipsoidal shape would also make the star overflow its Roche lobe, provoking a matter spill; in such a case, irradiation effects could be reasonably negligible. Other physical properties, such as temperature, radius etc. can be retrieved by comparing the color-magnitude diagrams with the observed optical properties.

3.6   Eclipse mechanisms

In this section we review the most commonly invoked mechanisms that can account for the periodic disappearance of the pulsed signal in eclipsing binaries, namely:

- Free-Free Absorption

- Raman Scattering

- Plasma frequency cut-off

- DM Pulse Smearing

All the models are based on the hypothesis that the responsible for such processes is a low-density highly-ionized gas cloud spilling off the companion, which can be released as a stellar wind. The effects can also be classified in different categories: The first three are actually *absorption processes* by which part or all of the radiation is intercepted by the cloud, resulting in a decrease or in the disappearance of the total flux density. The pulse smearing is instead different in nature, since it is an effect that is linked to the way pulses are revealed: in this case, as we will see, the signal is still present but it does not come out because of a varying dispersion measure.

3.6.1   Absorption effects

Let us start off with the well-known radiative transfer equation:

$$\frac{dI_\nu}{dl} = -\kappa_\nu I_\nu + j_\nu \tag{3.1}$$

where I_ν is the *specific intensity*, ($[I_\nu] = $ erg s^{-1} cm^{-2} ster^{-1} Hz^{-1}), j_ν is the *specific emission coefficient* ($[j_\nu] = $ erg s^{-1} cm^{-3} ster^{-1} Hz^{-1}) and κ_ν is the *specific absorption coefficient* ($[\kappa_\nu] = $ cm^{-1}), representing the variation in intensity of a radiation beam as it travels a distance dl.

For our purposes of studying eclipse mechanisms in the radio band, we can safely assume $j_\nu = 0$, so that eq. (3.1) reduces to:

$$\frac{dI_\nu}{dl} = -\kappa_\nu I_\nu \tag{3.2}$$

whose formal solution is:

$$I(s) = I(0)e^{-\int_0^L \kappa_\nu(l)dl} \tag{3.3}$$

where L is the length of the optical path. It is also common practice to define the dimensionless quantity Γ, called *optical depth*, as follows:

$$\Gamma \doteq \int_0^L \kappa_\nu(l)dl \tag{3.4}$$

This will be very useful for our theoretical analysis. In fact, in order to investigate the physics of BWPs, what we have to do is to find some form for the absorption coefficient κ_ν corresponding to the particular considered physical process; then we have to integrate it along the line of sight to finally get the total optical depth; in this way we will be able to predict the absorbed fraction of the total flux density as a function of the orbital phase, which we can compare, in principle, with observational data.

Free-Free absorption

Also known as *inverse bremsstrahlung*, free-free absorption is the main candidate for explaining the eclipses in most of the systems, since it manages to account for almost all the features usually observed.

In general, we have bremsstrahlung *emission* when free electrons move in the Coulomb fields of other nuclei, by which they are decelerated and thereby forced to emit radiation. In doing that, electrons are not captured and they pass from a free state to another such state; from that the name *free-free emission*. Analogously, we can refer to the process by which an electron, moving in an electrostatic field, absorbs an incoming radiation as *free-free absorption*.

The most widely used implementation is the one in which the involved particles follow a Maxwellian distribution of velocities, i.e. they are in thermal equilibrium. For this reason this case is referred to as *thermal bremsstrahlung*. To get the relative absorption coefficient, it is first convenient to start from the emission coefficient. It can be shown [43] that the total emitted power per unit volume and frequency f at a temperature T is:

$$\frac{dE(T,f)}{df\,dV\,dt} = \frac{2^5 \pi e^6}{3 m_e c^3} \cdot \left(\frac{2\pi}{3 k_B m_e}\right)^{1/2} \cdot \frac{1}{T^{1/2}} Z^2\, n_e\, n_i\, e^{\frac{-hf}{k_B T}} \cdot \bar{g}_{ff} \tag{3.5}$$

where n_i is the ion number density, Ze is their charge, k_B is the Boltzmann constant, m_e is the electron mass. The quantity $\bar{g}_{ff}$ is called the *Gaunt factor* and accounts for corrections of quantum nature.

Now, Kirchhoff's law for thermal emission gives the relation between the emission coefficient and the associated absorption coefficient, namely:

$$j_{ff}(T,f) = \kappa_{ff}(T,f) B(T,f) \tag{3.6}$$

where $B(T,f)$ is the *brightness* of a blackbody. From this we can get the absorption coefficient and express it in the more convenient CGS units:

$$\kappa_{ff}(T,f) = \frac{1}{4\pi} \cdot 6.6 \cdot 10^{-38} \frac{Z^2\, n_e\, n_i}{T^{1/2}} \bar{g}_{ff} \frac{c^3}{2hf} \cdot e^{\frac{-hf}{k_B T}} \ \text{cm}^{-1} \tag{3.7}$$

Since, for pulsars, we are dealing with radio waves, $hf/k_B T \ll 1$ certainly holds, so that we can approximate eq. (3.7) as:

$$\kappa_{ff}(T,f) = 0.173 \left\{ 1 + 0.13 \log\left(\frac{T^{3/2}}{Zf}\right) \right\} \frac{n_e^2}{T^{3/2} f^2} \tag{3.8}$$

Raman scattering

This process belongs to the class of non-linear absorption mechanisms, those in which the non-linear interaction of electromagnetic waves with other waves or electrostatic fluctuations (the so-called *plasmoms*) occur in the considered plasma. The interaction between electromagnetic waves and plasmons can be described according to the *kinetic wave equation* [51], which is in turn split into two parts:

- The interaction of the waves with electrons (e) or ions (i): $t + e(i) \leftrightarrow t + e(i)$

- The interaction of electromagnetic waves with other waves of the same or of different nature: $t \leftrightarrow t + l$, $t \leftrightarrow l + l$, $t \leftrightarrow t + t$

where t is a transverse electromagnetic wave and l is a plasmon. The second category is defined as *three-wave processes*. Gedalin & Eichler [22], in considering such mechanisms as a possible cause for pulsar eclipses, pointed out that only the first of the three-wave processes is actually relevant in the environment of black widow pulsars. Non-linear absorption mechanisms are also said to be *induced*, since their cross sections are proportional to the number of waves. If we suppose to have a turbulent plasma, i.e. with a sufficient number of plasmons (so that the process is favored in one direction, $t \leftarrow t + l$) we can regard it as the *Induced Raman Scattering*.

It can then be shown that the total optical depth of a plasma, due to this phenomenon, can be approximated as [22]:

$$\Gamma \simeq \sqrt{3} \cdot \int dl \, \frac{\omega_p}{4\pi^2 c} \left(\frac{\omega_p}{\omega}\right)^2 \left(\frac{k_B T}{m_e c^2}\right)^2 \left(\frac{m_i}{m_e}\right) \tag{3.9}$$

Plasma frequency cut-off

We have already argued, in Section 2.1.1, that electromagnetic waves passing through an ionized gas, cannot propagate anymore if its wavelength exceeds a certain threshold. This phenomenon, which we call here *plasma frequency cut-off*, can in theory be responsible for the disappearance of the signal under a certain frequency. To have a idea of the orders of magnitude necessary to trigger such a mechanism, we can rewrite eq. (2.7) in a more practical form with respect to the typical values of observing frequencies:

$$f_p = 9.3 \text{ MHz} \cdot \sqrt{\frac{n_e}{10^6 \text{ cm}^{-3}}} \tag{3.10}$$

The only physical quantity on which f_p depends is the electron number density. That means that such a mechanism cannot explain any possible frequency dependance of the typical observables, such as the eclipse duration, the TOA residuals etc. Many eclipsing pulsars do show different behaviors at different wavelengths and the plasma frequency cut-off cannot account for them at all.

In addition to this, it is easy to see that, in order to bring about eclipses at the usual observing frequency magnitudes ($100 \div 1000$ MHz), the electron number density should be of about $10^{9 \div 10}$ cm^{-3} [18]. These figures are at least one or two orders of magnitude higher than the average values of n_e which can be deduced by the analysis of the TOA time delays at the ingress/egress phases of the eclipse, in most of BWPs.

Nonetheless, it has been pointed out [52] that we might not want to consider the *average* density, since the plasma frequency cut-off only depends on the *local* electron density. For this reason, even if the average value is actually $n_e \sim 10^6$ cm^{-3}, we could have a layer of a much higher n_e with respect to the rest of the cloud, where $f_p \gtrsim f_{obs}$; such a situation can actually occur in the presence of a *contact discontinuity*, for instance like those characterizing shock boundaries, which can indeed form from the interaction of the companion's wind with the pulsar's radiation pressure (Section 3.3). All of this must anyway be confronted with the consequent evaporation time scale τ_{evap} that such a scenario

would imply: the high-density gas of the contact discontinuity has to be continuously replenished by new matter coming from the companion, which in turns implies a certain mass loss rate $\dot{M_c}$. From that, one can guess the approximate lifetime of the star, under the hypothesis of a steady mass flow, ($\tau_{evap} = M_c/\dot{M_c}$). The evaporation time scale gives us an indirect measure of the probability of spotting the source during the ablation process: the shorter τ_{evap} the lower the probability of detection.

3.6.2 DM pulse smearing

When we have a fine timing solution for the pulsar, obtained by the data relative to the off-eclipse orbital phases, we are taking into account the effect of dispersion due to the ISM, but we are neglecting any other possible effect that could change the DM. At orbital phases near superior conjunction, given a proper system orientation, the pulsar signal crosses the ionized regions of the companion's atmosphere before reaching the observer. This implies a higher column density with respect to that of the only interstellar medium, and hence the plasma cloud from the ablated companion will give an extra-contribution $\Delta\text{DM}(\phi)$ to the dispersion measure, dependent on the considered orbital phase ϕ.

We can formally express it as:

$$\Delta\text{DM}(\phi) = \int_{\text{cloud}} n_e dl \qquad (3.11)$$

where the integral is performed along the part of the line of sight actually crossing the cloud at the particular orbital phase. This additional dispersion measure has two major observable effects. The first one is that the pulse profile obtained by summing different frequency channels results broadened. More precisely, what happens is that the two extreme frequency channels of frequencies $f_{\min}, f_{\max}$ will experience a relative delay of:

$$\Delta t_{\text{smr}}(\phi) = \mathcal{D} \cdot \Delta\text{DM}(\phi) \cdot \left(\frac{1}{f_{\min}^2} - \frac{1}{f_{\max}^2}\right) \qquad (3.12)$$

for the same reasons as explained in Section 2.1.1. Calling W the total pulse width, it is straightforward to understand that $\Delta t_{\text{smr}} = \Delta W$, as shown in Figure 3.4. If the total pulse width becomes comparable to the pulsar period ($W \sim P$), the smearing due to the ΔDM can make the pulsed signal completely disappear.

It is worth remarking that this effect does *not* cause any decrease in the total received flux density, but only in its pulsed component; this implies that the continuum signal (i.e. the radio signal averaged over a pulsar rotation) remains the same and it is not influenced at all by that. For the above
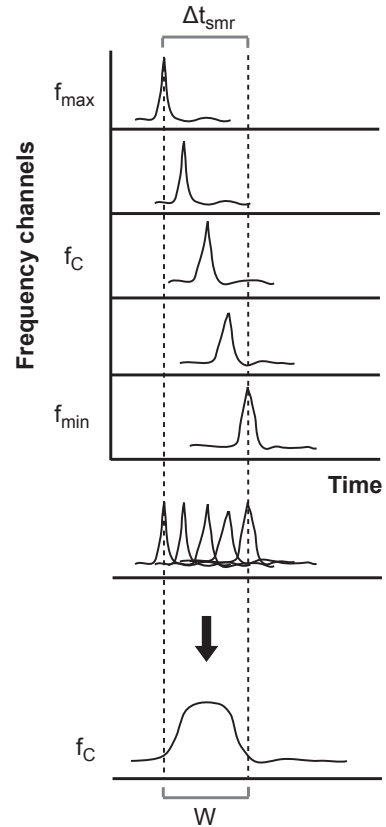

Figure 3.4

reasons it would be of fundamental importance to have both the pulsed and continuum signals of single observations, in order to understand if the DM pulse smearing is the actual mechanism to cause the eclipses. If, corresponding to the *pulsed* signal eclipse, we do not witness any significant decrease of the *continuum* flux, we can be fairly confident that this latter mechanism is the true responsible. Unfortunately, most of back-ends used in modern single-dish radio telescopes discard the profile baseline during the on-line folding procedure, so that it is impossible to retrieve it later. Parallel observations of the continuum component are then necessary with another suitable telescope.

Correlation with time delays

There exists another powerful method to probe whether the actual responsible for the eclipses is the DM smearing or not, that is the strong correlation between the observed excess time delays and pulse widths.

Also after being summed in frequency, the resulting signal at the particular frequency f_c, (which is actually the central frequency of our receiver band) is delayed because of the very same excess dispersion measure ΔDM that caused the pulse broadening. Consequently, the TOA residual relative to the orbital phase ϕ, will be:

$$\Delta t_a(\phi) = \mathcal{D} \cdot \Delta\text{DM}(\phi) \cdot \frac{1}{f_c^2} \tag{3.13}$$

We can thus relate the smearing of a pulse to the delay in its time of arrival. Dividing eq. (3.13) by eq (3.12), we get:

$$\frac{\Delta t_a}{\Delta t_\text{smr}} = \frac{\frac{1}{f_c^2}}{\frac{1}{f_\text{min}^2} - \frac{1}{f_\text{max}^2}} \tag{3.14}$$

Hence:

$$\Delta t_a = \left(\frac{1}{f_c^2} \cdot \frac{f_\text{min}^2 f_\text{max}^2}{f_\text{max}^2 - f_\text{min}^2}\right) \cdot \Delta t_\text{smr} \tag{3.15}$$

We can also express the final pulse width as the sum of the off-eclipse pulse width W_0 (which depends both on the shape of the radio beam and on the single channel bandwidth) and the additional contribution due to the extra DM, ΔW:

$$W = W_0 + \Delta W = W_0 + \left(f_c^2 \cdot \frac{f_\text{max}^2 - f_\text{min}^2}{f_\text{min}^2 f_\text{max}^2}\right) \cdot \Delta t_a \tag{3.16}$$

Solving for Δt_a, we obtain:

$$\Delta t_a = -\frac{W_0}{\left(f_c^2 \cdot \frac{f_\text{max}^2 - f_\text{min}^2}{f_\text{min}^2 f_\text{max}^2}\right)} + \frac{W}{\left(f_c^2 \cdot \frac{f_\text{max}^2 - f_\text{min}^2}{f_\text{min}^2 f_\text{max}^2}\right)} \tag{3.17}$$

From eq. (3.17) we see that, if the eclipses are indeed provoked by an ionized cloud that contributes to increase the DM, we expect a linear correlation between residuals and pulse widths near the eclipse phases. Both the quantities are easily measurable from the only pulsed signal, without any need for a continuum component.

3.6.3 Refractive models

In addition to the previously analyzed absorption and smearing processes, one can also consider another class of possible effects. These are grouped under the definition of *refractive models*; basically, they are either the reflection or the bending of the optical path of the emitted signal and require the plasma frequency inside the ionized cloud to be of the order of the observing frequency ($f_p \sim 1$ GHz).

As for any respectable model, they must in turn account for as many observed characteristics as possible. Refractive models are satisfactory for some of them, but cannot explain some others [19]. Among the features which seem to fit well with such models are the predicted small evaporation time scales, of only $\sim 10^7$ yr. This would perfectly agree with most of the proposed evolutionary scenarios besides justifying a possible disappearance of the companion (thus explaining the existence of isolated millisecond pulsars) and the very small probability of spotting such systems.

However, important faults prevent them from being considered the preferred models, at least for most of the eclipsing systems discovered so far. First of all, they cannot explain the frequency dependance of the eclipse duration: reflection mechanisms would predict no dependance at all whereas refractive bending ones would, but could hardly fit the observed data of the historical eclipsing systems. Another major reason is related to the maximum plasma density at the border of the cloud. By simply requiring total energy conservation [19], it can be shown that, necessarily:

$$\rho(R_E) < \rho_{\max} \equiv \frac{L_p R_c^2}{8\pi a^2 v_f^3 R_E^2} \tag{3.18}$$

Here L_p is the pulsar spin-down power, R_c is the companion radius, a the orbital separation, v_f the mass outflow velocity and R_E the radius of the eclipsing region. Some simplifying assumption have been made: for instance, the mass outflow and, consequently, the eclipsing region were assumed to be spherically symmetric. Using typical values in eq. (3.18), like those of system PSR 1957+20, one soon realizes that $\rho_{\max}$ is at least two orders of magnitude smaller than the value required for refractive effects, even with the most conservative hypotheses.

3.7 PSR 1957+20: the prototype of the BWP

Special attention deserves PSR 1957+20, the first eclipsing binary system ever discovered [21]. It is composed of a millisecond pulsar ($P = 1.61$ ms) along with a very low mass companion showing evidence of ablation. For this reason, at that time, it was believed to be the missing link between LMXBs and the rarely observed isolated millisecond pulsars. The main characteristics are summarized in Table 3.3.

We can notice the extremely low eccentricity, the low spin-down rate and the orbital period of a few hours. Observations of pulses over many orbits revealed the presence of regular eclipses lasting 55 minutes on average (depending on the observing frequency), about 10% of the orbital period. A simple calculation, based on such data, can show that the radius R_E of the eclipsing region (assuming it to be spherical, for the sake of simplicity) is much

PSR B1957+20		
Period, P	[ms]	1.607
Period Derivative, $\dot{P}$		$1.61 \cdot 10^{-20}$
Eccentricity, e		$\lesssim 2 \cdot 10^{-5}$
Companion Mass, M_c	[M$_\odot$]	$\simeq 0.022$ M$_\odot$
Orbital Period, P_b	[h]	$\simeq 9.17$
Dispersion Measure, DM	[pc cm^{-3}]	29.1
Spin-Down Energy, $\dot{E}$	[erg s^{-1}]	$7.48 \cdot 10^{34}$

Table 3.3: Brief summary of the main characteristics of PSR B1957+20, the prototype of all black widow pulsars.

larger than the Roche lobe radius R_L of the companion; in fact we have $R_E \simeq 0.75$ R$_\odot$ whereas $R_L \simeq 0.3$ R$_\odot$. This consideration suggested that the eclipsing medium had to be in some way continuously replenished by the companion's atmosphere; the most probable mechanism, given the absence of heavy accretion which would have obscured the signal, is the evaporation of the companion caused by the pulsar spin-down irradiated power.

Due to its faintness, observations of the source were carried out with the 305-meter wide Arecibo radio telescope in Puerto Rico. The procedure for getting the physical parameters was the classical timing analysis based on the measurements of the times of arrival of the integrated pulse profiles at the off-eclipse orbital phases. We can see in Figure 3.5 some integrated profiles at different frequencies; interpulses, i.e. pulses shifted by 180° in pulse phase with respect to the main pulse, are clearly visible in each of them. From the analysis
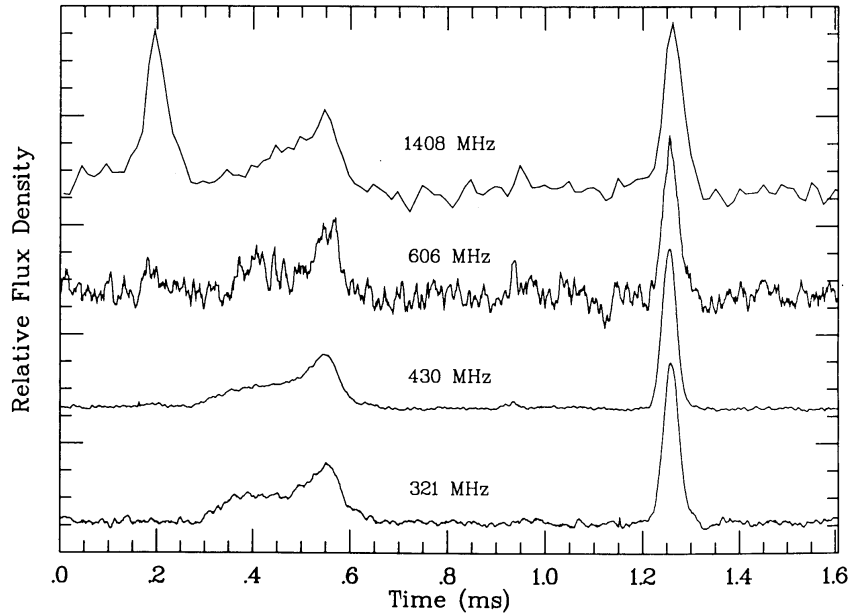

Figure 3.5: Integrated pulse profiles for PSR B1957+20 at different frequencies.

of barycentric TOAs, a plot like that of Figure 3.6a could be obtained. What immediately results evident is the total disappearance of the pulses in a large fraction of the orbit.

Looking at the TOA residuals of Figure 3.6a, we can see that they get larger and larger, showing deviations with respect to the timing solution, as the pulsar approaches the eclipse region; this can be imputed to the presence of the gas cloud itself which, with its additional electron column density, causes the signal to be delayed. The thicker the cloud along the line of sight, the higher the delay. It is also worth noticing the asymmetry between the pre- and post-eclipse delays, the latter being significantly larger than the former. This indicates a possible asymmetry of the eclipsing cloud, possibly due to the combined effects of radiation pressure and Coriolis forces of the orbital motion; we could then expect a cometary-like shape for the cloud, rather than being spherical.
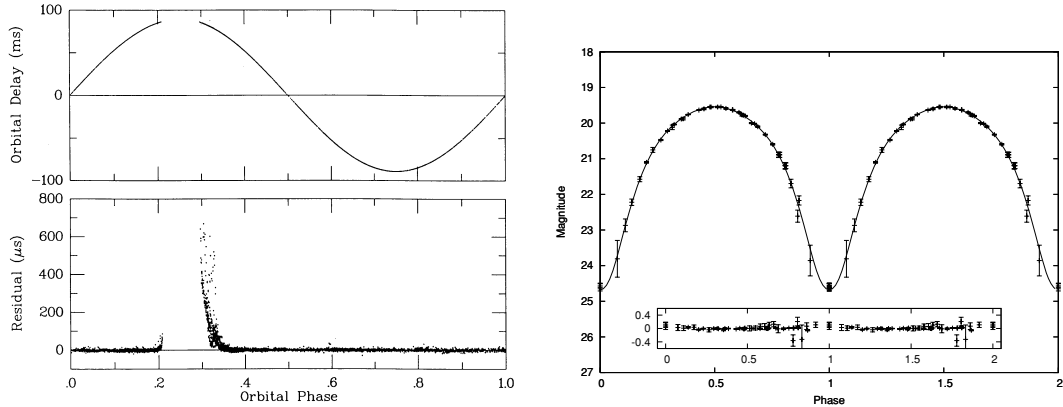
(a) Measured TOA residual as a function of the orbital phase for PSR B1957+20.

(b) Optical light-curve for PSR B1957+20. Note the different convention adopted by optical photometry for the orbital phases.

Figure 3.6

3.7.1 Optical light curve

Optical studies were also carried out in order to reveal the companion. The spin-down luminosity of PSR 1957+20 turned out to be remarkably high ($\dot{E} \simeq 4\pi^2 I \dot{P} P^{-3} \simeq 20 \ \mathrm{L}_\odot$), sufficient to make the other star's surface hot enough to let it evaporate. Moreover, the optical luminosity suggested the companion's radius to be about $R_c \simeq 0.15 \ \mathrm{R}_\odot$, confirming all the previous guesses about the absence of any Roche lobe overflow.

Reynolds et al. [37], in 2005, put new constraints on the physical properties of the companion as well as on the inclination of the system, thanks to new data taken from the Hubble Space Telescope (HST) in optical K_s and R-band. Previous efforts to put constraints from optical data were vane because of the undetectability of the source around minimum of the light curve, a problem which has been overcome by HST. A fit on the data of optical magnitude as a function of the orbital phase was performed, varying the inclination i, the Roche lobe filling fraction f_{RL}, the temperature and bolometric albedo[3] a_{TB} of the companion, as well as the irradiated luminosity of the pulsar, L_p. They looked for the set of parameters which achieved the best fit both on optical data and on the timing residuals. The result is shown in Figure 3.6b. The best agreement is attained with $i = 64.4°$ for a pulsar mass of $M_p = 1.4 \ \mathrm{M}_\odot$. Spanning the latter in the range $1.3 < M_p < 1.9 \ \mathrm{M}_\odot$, the

---

[3]The *bolometric albedo* is defined as the ratio between the reradiated energy to the irradiance energy.

inclination is constrained in the range $63° < i < 67°$ at the 3σ level. More interesting are the values obtained for Roche lobe filling fraction, i.e. $0.81 < f_{RL} < 0.87$, meaning that the companion is quite far from a matter spill through the Lagrangian point L2. This result has to be compared with the considerations made on the eclipsing region size, which turned out to be much larger than R_L, confirming the hypothesis of an ongoing atmosphere evaporation.

The last free parameter that is worth to discuss is the observed temperature of the companion at maximum and minimum, corresponding to the illuminated and unilluminated side, respectively. With the previous range of the pulsar mass, they found an effective temperature of $T_{\max} = 8300 \pm 200$ K and $T_{\min} = 2900 \pm 110$ K at 3σ. Simulations, which also took into account hydrodynamical effects, showed that such a high temperature gradient between the two hemispheres is actually sustainable, no matter if the companion is degenerate or not degenerate.

Regarding the nature of the secondary star, these optical studies are of fundamental value. In fact, the color information let us be sure that the hypothesis of a cool white dwarf must be ruled out: both the $R - I$ magnitudes and the derived radius $R_c \simeq 0.3$ R$_\odot$ are too high for such a case. Rather, their values are in agreement with a possible late M-type dwarf. However, the mass function of the system suggests a value for the companion's mass that is likely well below the threshold of the hydrogen-burning limit ($M > 0.08$ M$_\odot$), making very probable for the star to belong to the class of *brown dwarfs*.

3.7.2 X-ray spectrum

A striking feature to be noticed of the optical light curve is its very high symmetry, in contrast to the visible asymmetry in the TOA residuals. This is a compelling evidence that the modulation in the optical data is given by the emission of the companion's surface, rather then the surrounding gas cloud. Moreover, this indicates that a possible intra-binary shock between the pulsar wind and the evaporating gas is not visible at optical wavelengths but must be searched in other bands.

Recent studies, conducted though a phase-resolved spectral analysis, have shown non-thermal X-ray emission that must necessarily be due to an intra-binary shock, formed by the interaction between the pulsar wind and the ablated gas.

Huang et al. [40] used Chandra observations, covering more than five consecutive orbits, for searching for a modulation in the X-ray flux as a function of the orbital phase. To probe the hypothesis of the intra-binary shock, they analyzed the observed X-ray spectrum separately between the orbital phases $\phi = 0.05 - 0.45$, which covers all the eclipsing process, and the rest of the orbit ($\phi = 0.45 - 1.05$). The phase-resolved spectral analysis revealed an orbital dependance of the spectrum properties; in particular, performing χ^2-tests, they spotted a marginal intra-binary modulation which induces to associate the non-thermal component of the X-ray spectrum with the interface between the pulsar wind and the ablated material.

Chapter 4

A Python code for eclipsing binary pulsars

One of the crucial parts of this thesis work was the development of a powerful code for studying eclipsing binary systems. The code had to be, in the author's intention, highly scalable and adaptable for the many different situations one could come across, especially in the perspective of a more complicated panorama in the years to come. It also had to be able to simulate different eclipse mechanisms, to adjust itself to the various system geometries and to compare theoretical results with experimental data.

4.1   Why Python

The language in which the code was written is Python, and the reasons for this choice are many. First of all, Python is one of the most modern object-oriented, high-level programming languages currently available, for it boasts a number of features which simplify a lot the development of a software; among these we recall the dynamic typization, the variety of flexible data structures (such as dictionaries and lists), the dynamic memory allocation. Moreover, Python is spreading more and more in the scientific and, in particular, in the astronomical community; this guarantees future support and integration with other softwares and libraries. Indeed, literally hundreds (probably thousands) of astrophysics libraries for Python are currently available for the most various purposes, from coordinate transformations to fitting algorithms, to databases of astrophysical sources.

4.2   Why V-Python

The choice of including a 3D visual graphics library was not driven only by aesthetic motivations. V-Python is also a powerful tool that allows to handle tridimensional geometries in a much easier way with respect to standard analytical calculations. Indeed, it includes routines for creating, modifying and animating complex 3D shapes. Each 3D object, or collection of objects, can have its own reference frame that can be oriented differently from the main "scenery frame"; simple built-in functions let the developer pass from one frame

to another in a tremendously easy way, which makes complicated analytical coordinates transformations completely unnecessary.

Moreover, the real-time animation capabilities of V-Python result useful both for a programmer and for an astronomer. For the former they can work as a debugging tool, allowing him to see what the code is doing instantaneously. For the latter they are very useful as an analysis method, since one can see one or more theoretical curves drawing while the binary system visually evolves.

4.3 Code structure and capabilities

In this section we briefly describe the code structure and the tasks it is able to perform.

The code is composed of over 4000 lines of Python instructions, organized in a "main" flow and 65 auxiliary sub-routines. When launched, the code asks the user the effects to take into account during the simulation (Figure 4.1). Then it asks if only one single simulation is needed (for example if one just wants to study a single hypothetical scenario) rather than acquiring data and performing a fit on them. In the latter case, depending on the chosen effect, a file of TOA residuals, DM offsets or flux densities as a function of the orbital phase must be indicated. The program then offers the user the possibility of pre-processing the data, through a binning, in order to have a better statistic for each interval of the orbit, and that can be very useful in the cases of plentifulness of data. The binned data can also be saved as a new, separate file. Once the data is ready to be used for the fit, the ranges of the involved free parameters are asked, while the fixed ones instead come from an ephemeris file which must be given to the code. Then the fitting procedure starts.

At the end of the process the code returns the ten best sets of parameters and allows the user to plot the result of the simulation with each of those sets and, in case, write the outcomes on a file, so that the user can later plot and compare the data with the best-fit curves. In the next subsections we will examine the main features in greater detail.

4.3.1 Data acquisition and pre-processing

Experimental data, against which one wants to compare simulations, can be picked up soon after the choice of the effects to account for. The function responsible for the acquisition accepts file containing TOA residuals, DM offsets or flux densities as a function of the orbital phase, which can be either the fractional mean anomaly or the fractional true anomaly. In the former case a conversion is made (see Section 4.3.6) before performing any simulations. This is because the code natively works on the rest frame of the pulsar, which is then placed on the focus of the companion's elliptical orbit; this implies the true anomaly to be the most natural angle to work with.

The pre-processing consists in re-binning the data in intervals of the orbital phase. The user has to choose the number of bins, then the program searches for all the points falling in each bin and assigns to it the mean value and an associated error. The mean value can be a simple arithmetic average or a weighted mean, whilst the associated error is normally the error on the mean, i.e. the root mean square divided by the number of samples.

Figure 4.1: Initial prompt of the code.

4.3.2 Different geometries and density profiles for the plasma cloud

The asymmetries sometimes seen at the eclipse ingress and egress phases of some black widow pulsars makes it necessary to consider possible shapes, different than spherical, for the eclipsing plasma cloud. In particular, we remarked the realistic hypothesis of some cometary-tail shaped bow-shock clouds around the companion. For this reason, the code contemplates four geometries, three of which can be seen in Figure 4.6; for each of them, various possible density profiles are considered. Here the power of the visual module for Python becomes evident: in fact, we can write each density profile with respect to the most comfortable coordinate system for the considered case, where its expression is the simplest. Its analytical form is indeed given in a cartesian frame of reference (x, y) in which the companion, assumed to be point-like, is placed at the origin. In the same frame, we use r to denote the distance from the origin, θ for the angle between the considered vector (x, y) and the x-axis, so that $\tan \theta = y/x$. The pulsar is assumed to be at $(a, 0)$, where a is the usual orbital separation. To calculate the column density from the pulsar to the observer we just have to integrate the contributions $n_e(l)$ along the line of sight, at the various orbital phases. The advantage is that there is no need to rewrite the expression of the number density as a function of ϕ; rather, for each sampled orbital phase, we can directly use the built-in routines to pass from the "world" coordinates to the "cloud" coordinates, and then use the simple expression of n_e in the latter frame.

Sphere It is the standard geometry for a plasma cloud surrounding the companion. It can represent an isotropically emitted wind on which neither the orbital motion nor the pulsar radiation pressure substantially affects the outflow shape. The simulated curve necessarily suffer from a symmetry around superior conjunction, and cases such as PSR B1957+20 cannot be reproduced. The associated density profile is a simple inverse power law with an index β, which we can write as:

$$n_e(r) = n_e(R_E) \left(\frac{R_E}{r} \right)^{\beta} \tag{4.1}$$

where R_E is the assumed radius of the eclipsing region and $n_e(R_E)$ is the corresponding local density. Both of them can be guessed by simple considerations based on the observed TOA residuals.
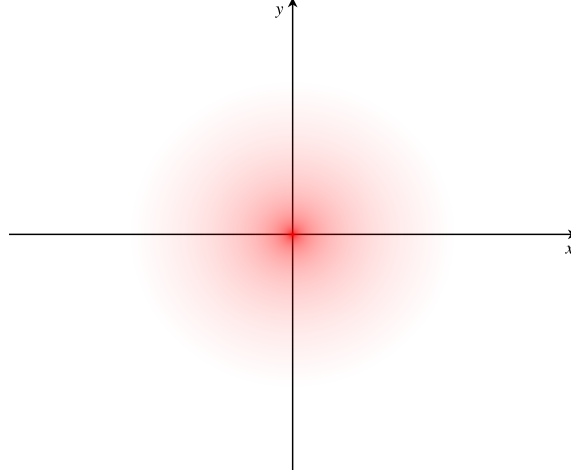

Figure 4.2: Spherical power-law density profile.

Ellipsoid As highlighted by Lipunov [33], under particular conditions, a closed cavern can form around the star from the strong interaction between the pulsar and the stellar wind. Even though having an own analytical expression, we can approximate the boundaries of such a cavern with an ellipsoid and put the companion at one of the foci. This let us treat the possible density profiles in a simpler way. Given its symmetry, it is given the possibility to slightly tilt the major ellipsoid axis with respect to the pulsar-star direction by an angle θ_T (for example because of non-negligible Coriolis forces), allowing the generation of asymmetrical results at ingress and egress. The two possible density profiles are:

$$n_e(x) = \frac{n_e^{max}}{(2s_a)^\beta} \cdot (x - x_f + s_a)^\beta \tag{4.2}$$

$$n_e(x,\theta) = \frac{n_e^{max}}{(2s_a)^\beta} \cdot (x - x_f + s_a)^\beta \cdot \left| \cos\frac{\theta}{2} \right| \tag{4.3}$$

where n_e^{max} is the maximum local density, which occurs at the pulsar-side vertex of the cloud, s_a is the semi-major axis of the ellipse, x_f is the x coordinate of the ellipse focus. All the lengths are expressed in units of solar radii, so that they result dimensionless. The relative scalar fields are shown in Figure 4.3a and 4.3b, respectively. The two can be thought as rough test profiles for shocked closed caverns formed by an isotropically emitted wind. In case a) the wind can be imagined to be uniformly emitted from all over the surface, whilst in case b) we can think it to be emitted from only the illuminated side of the companion. The possible free parameters are n_e^{max}, the index β, the size of the ellipsoid and its eccentricity $\mathcal{E}$, the tilt angle θ_T.

(a)   (b)
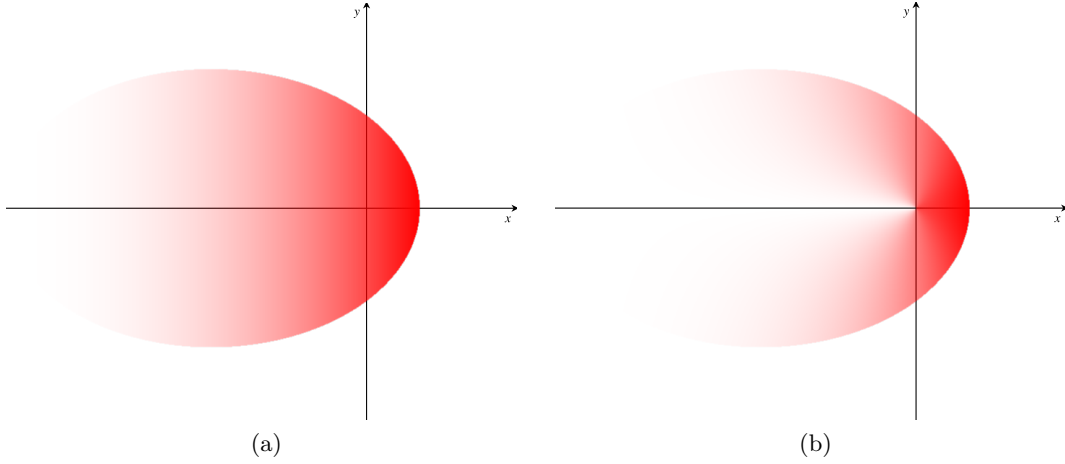
Figure 4.3

Paraboloid In other systems the intra-binary bow-shock between the pulsar wind and
the ablated material forms an open cavern, whose boundaries can be reasonably
approximated by a paraboloidal geometry. As in the previous case the companion is
conventionally located at the focus and it is given the possibility of introducing an
asymmetry, by means of a tilt angle θ_T. The analytical expressions of the density
profiles are:

$$n_e(x) = n_e^{max} \cdot [-(x - x_f - 1)]^{-\beta} \tag{4.4}$$

$$n_e(x, \theta) = n_e^{max} \cdot \left| \cos \frac{\theta}{2} \right| \cdot \left[-(x - x_f) + \left| \cos \frac{\theta}{2} \right|^{-\beta} \right]^{-\beta} \tag{4.5}$$

where all we said in the previous case about notation still holds, but is referred to
a parabolic shape. The adjustable parameters are: the quadratic coefficient of the
parabola on which the paraboloid of revolution is built, n_e^{max}, β, θ_T. The scalar field
of the two profiles can be seen in Figure 4.4.

(a)   (b)

Figure 4.4

Cometary tail It is the case in which the combined effects of orbital motion and pulsar-stellar wind interaction generate a strongly warped tail in the gas cloud. This geometry resembles that used by Rasio (Figure 3.2a, [18]) and is realized using a quadratic expression for the symmetry axis and for the paraboloidal shape of the cloud with respect to the former. That means that the curved symmetry axis has the analytic expression $y = Cx^2$ on the xy-plane whereas the boundaries of the com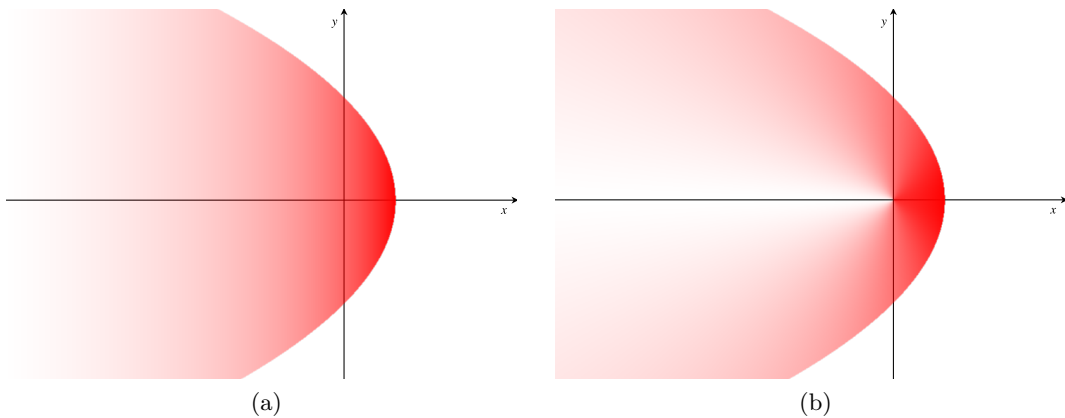et are given by an expression like $d = \sqrt{\xi/A}$, where ξ is the arc length calculated from the vertex (Figure 4.5). The constants C and A are two free parameters which will be made vary in our simulations. To simplify some calculations, in this case the companion is assumed to be on the symmetry axis at the curvilinear coordinate $\xi = 1/4A$. The density profile is identical to that of eq. (4.4), if one replaces x with ξ:

$$n_e(x) = n_e^{max} \cdot [-(\xi - 1)]^{-\beta} \tag{4.6}$$
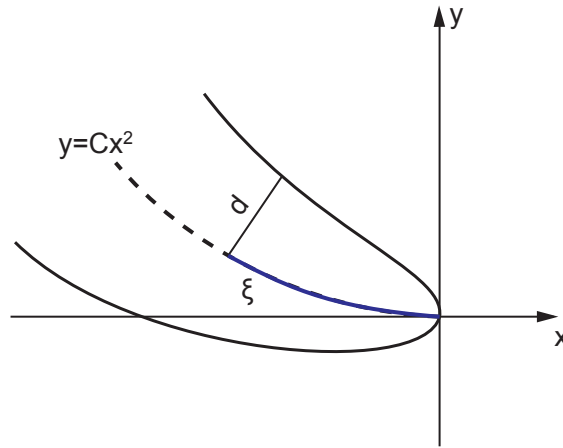
Figure 4.5: Cometary-shaped shaped gas cloud. The arc length ξ of a point on the parabolic symmetry axis and its distance d from the cloud boundary are related by a quadratic expression, namely $\xi = Ad^2$. The density profile is the same as eq. (4.4), provided that one replaces x with ξ.
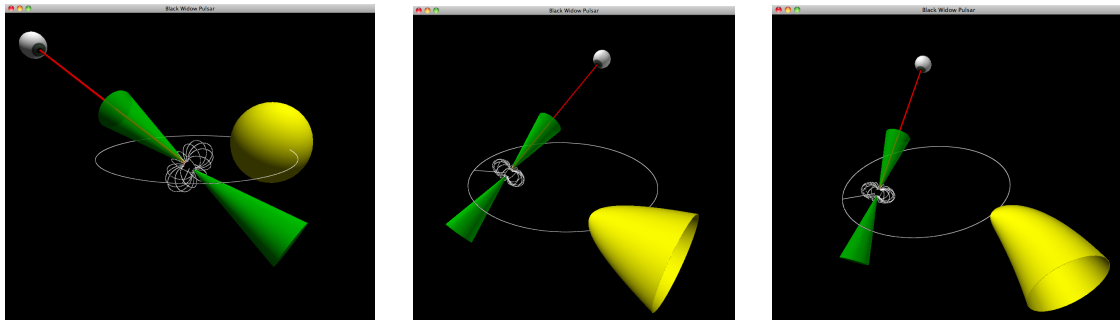
(a) Sphere. (b) Paraboloid. (c) Paraboloidal cometary tail.

Figure 4.6: Three possible shapes for the plasma cloud (in yellow) as seen with the 3D module V-Python. The line of sight is in red and the observer is represented by the eye.

It is important to remark the fact that these density profiles are absolutely artificial and have little or no physical justification. We chose them essentially for their ease of use, since we are interested in their *global* effects. In other words, we first want to understand

whether a particular geometry can roughly reproduce the data and, if so, what are the orders of magnitude of the relative parameters. From that, we might then further speculate about the nature of the system.

Temperature profiles

All of the profiles that were presented above in describing the possible gas density distributions were also used to model the temperature profile of the cloud. In fact, we exploited the fact that $T \propto (n_e)^{\gamma-1}$, where γ is the polytropic index. As for virtually all the relevant astrophysical applications, our code contemplated the two main cases of an isothermal ($\gamma = 1$) and an adiabatic ($\gamma = 5/3$) wind outflow.

4.3.3 Eclipse mechanisms and multi-frequency simulations

On the basis of the systems that we decided to investigate, we included a limited number of effects than can be simulated by the code, namely the ones we have already discussed in presenting black widow pulsars: Plasma Frequency cut-off, Free-Free absorption, Raman scattering, Offsets in DM due to the cloud and the consequent DM smearing in the integrated pulse profiles.

The importance of doing multi-frequency analyses (Section 3.6) is directly linked to the different dependance on the frequency among the possible mechanisms. The code does indeed have the capability of carrying out simulations at different frequencies at the same time; when performing fits on multi-frequency data it is able to take all of them into account and return the set of parameters which best reproduce the data at the various wavelengths on the whole.

The program initially suggests a set composed of four among the most often used central frequencies, namely 430, 820, 1390 and 2600 MHz, along with a bandwidth of 256 MHz. It goes without saying that it also leaves the possibility for the user of modifying such values, as well as of choosing a different number of frequencies to consider. When writing on a file the results of a multi-frequency simulation, the user can select the one he is interested in at that moment.

4.3.4 A basic fitting tool

The main use we can do of the code is comparing experimental data with theoretical models and see which one best reproduces the observations. In this way we can put some constraints on the value of the physical parameters or, at least, try to find the direction toward which we should keep studying the system.

This function is implemented using a classic least-square algorithm on the variable:

$$\chi^2 = \sum_i^N \left(\frac{\mathcal{Y}_i - y_i}{\sigma_i} \right)^2 \tag{4.7}$$

where y_i are the experimental values with associated uncertainties σ_i, and $\mathcal{Y}_i$ are the computed theoretical values. What the program does in this case is taking all the orbital phases ϕ_i at which experimental points were acquired; then it calculates the theoretical points $\mathcal{Y}_i$ at exactly such phases, with the current particular set of parameters, and use them to calculate the reduced chi-square, namely $\tilde{\chi}^2 \equiv \chi^2/N_f$ where N_f are the degrees of freedom, in our case corresponding to the total number of points. Then it looks for the parameter sets which minimize $\tilde{\chi}^2$ and returns them to the user.

Even if there are a lot of efficient algorithms, able to span the parameters space in an intelligent way that translates in a reduced computational time needed, we preferred to initially opt for a basic brute-force algorithm, spanning the ranges of parameters uniformly. In fact, despite its main disadvantage, i.e. its very low performance, especially in cases which involve many parameters, this method let us be sure we do not to fall in any local minimum of the χ^2 variable, a problem which most of non-stochastic optimization algorithms are subject to. Moreover, the data we had did not allow us to determine the parameters to a high degree of accuracy and thereby the computational time was not a real trouble.

4.3.5 Real-time graphs and integration with GNUPLOT

The visual library implemented in the code permits to have a graphical output of the simulations. In particular, the program shows a tridimensional representation of the binary system, with the pulsar at the center of the frame and the companion's gas cloud orbiting around. The track of the orbit, along with its periastron in the case of a non-zero eccentricity, is also shown. As already cited, the calculated curves can be displayed simultaneously on an additional 2D plot of a separated panel (Figure 4.7).

Not of secondary importance is the possibility of plotting the results at a later time. Among the tens of functions of the code, one is responsible for creating a GNUPLOT script through which the produced data can be displayed. According to the particular calculation the code has just made, it adjusts titles, labels, color schemes and other options in the most adequate fashion for the kind of plot. In this way the only thing the astronomer has to do is running the script in GNUPLOT with the command `load` to see the results.

4.3.6 Numerical methods

Among the functions, the code includes some routines for performing numerical estimates of definite unidimensional integrals. In particular, this comes from the need to calculate the electron column number density along the line of sight. The integration method on which we based the function is the popular Cavalieri-Simpson method that, in its simplicity, guarantees very good precisions with little computational costs.

In addition to this, we had the need of solving implicit functions, for example in passing from the mean anomaly $\mathcal{M}$ to the true anomaly A_T in eccentric orbits. For this purpose we wrote the relative routine basing it on the Newton-Raphson method which also represents a good trade-off among straightforwardness, precision and speed.
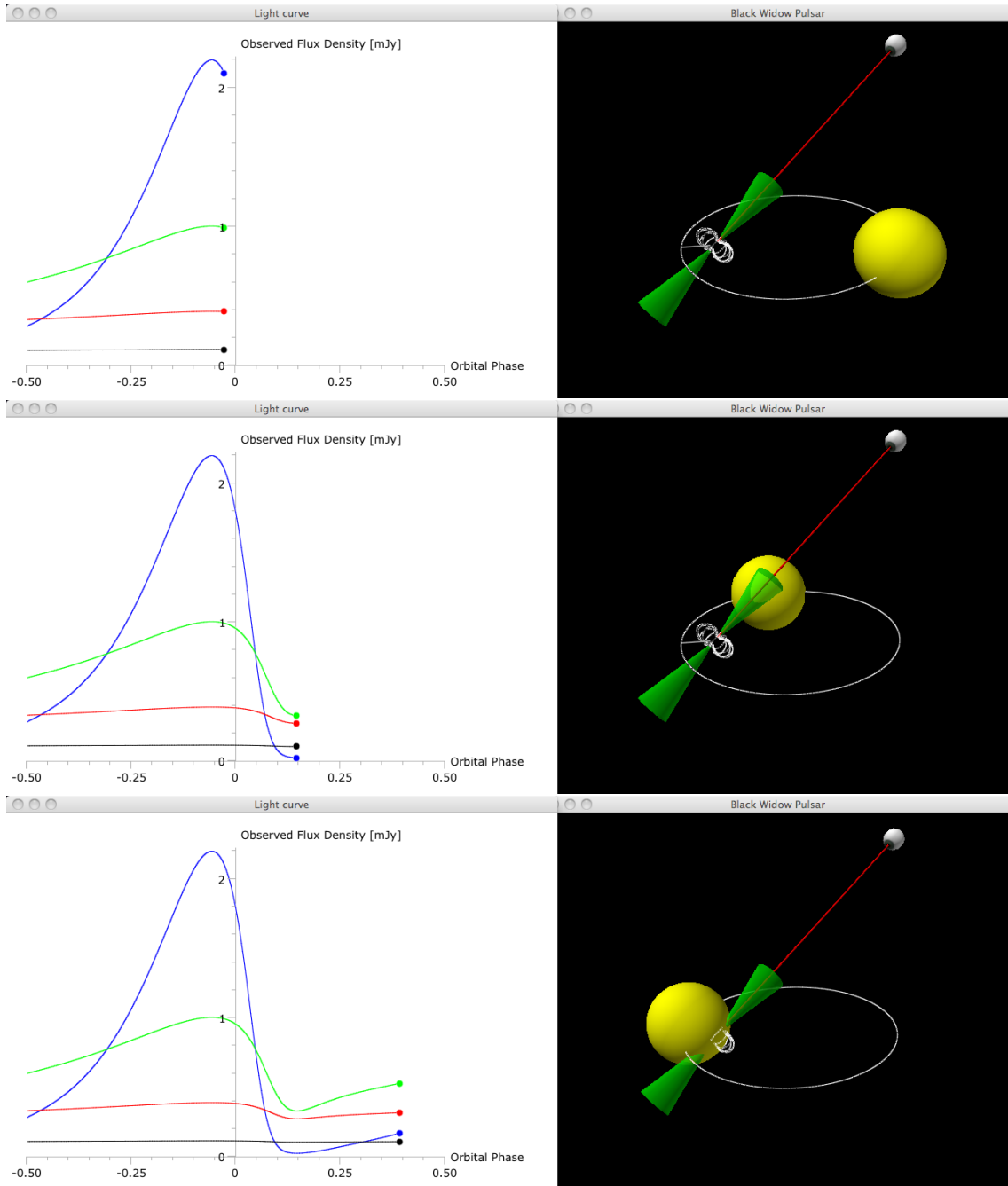
Figure 4.7: The real-time multi-frequency plotting feature: while the companion orbits the pulsar, the curves are correspondingly drawn. In the right-hand panels the red line is the line of sight of the observer, represented by the eye. In the left-hand panels the mean flux densities, at the four standard frequencies, are plotted against the fractional true anomaly. The artificial system, used for the demonstration, has $e = 0.7$ and $\omega = 230°$. Even if drawn as having a net boundary, the cloud was assumed to extend indefinitely.

4.4 Testing the code: PSR J1740-3052

In order to make sure that the code was working properly, we tested it on a well-known source, namely PSR J1740-3052.

Hosting a young pulsar along with a likely B-type main sequence star, PSR J1740-3052 is thought to be the progenitor of a HMXB [56]. Since its discovery in the late 90s, many observations were performed at different frequencies at the Green Bank, Parkes, Lovell and Westerbork telescopes, spanning 1997 to 2011, from which an accurate timing solution has been extracted. The parameters so obtained point toward a system in which the companion star ejects a strong wind, affecting the observed DM and, thus, the pulse profiles.

PSR J1740-3052 [14]		
Data Span	[MJD]	50760 - 55622
Right Ascension (J2000), RA	[hh:mm:ss.sss]	17:4050.001
Declination (J2000), DEC	[dd:mm:ss.sss]	-30:52:04. 3
Spin Period, P	[ms]	0.570313411724(3)
1st Period Derivative, $\dot{P}$	[10^{-14} s s^{-1}]	2.5504275(95)
2nd Period Derivative, $\ddot{P}$	[10^{-26} s s^{-2}]	8.8(6)
Dispersion Measure, DM	[pc cm^{-3}]	738.73(8)
Orbital Period, P_b	[days]	231.029630(2)
Eccentricity, e		0.57887011(19)
Longitude of Periastron, ω	[°]	178.646811(17)
$a \sin i$	[ls]	756.90794(14)
1600 MHz flux density	[mJy]	~ 14 mJy
Spectral Index		$\sim$ -2.8
Companion's spectral type		G
Derived Parameters		
Mass Function, $f(M_c)$	[M$_\odot$]	8.722676(3)
Inclination, i	[°]	53(7)

Table 4.1

We chose this system as a test for our code both for the plenty of information we already have and for its peculiar features, which are listed in Table 4.1. In particular, the pulsar spins with a period of 570 ms, shows a characteristic age of 0.35 Myr and orbits the companion with quite a long period of 231 days. Although it does not show any eclipses, it shows an orbital modulation in the dispersion measure, which peaks in the vicinity of periastron passage (Figure 4.8); this behavior can be easily explained by a system in which the pulsar orbits inside the companion's wind. Ultimately, its high eccentricity ($e \simeq 0.58$) is another crucial property that makes the system a valuable probe for the code we developed.

Madsen et al. [14] fitted the data shown in Figure 4.8 through an MCMC algorithm using an early B-type stellar wind model as responsible for the observed increases in DM. Assuming the wind constituted only by hydrogen, the numeric electron density has the

following expression [54]:

$$n_e(r) = \frac{\dot{M}}{v_{\text{ratio}}} \frac{1}{v_{\text{esc}}} \frac{1}{4\pi m_p} \frac{1}{\sqrt{1 - R_c/r} \cdot r^2}.$$
(4.8)

Here $\dot{M}$ is the mass loss rate of the companion due to the wind, v_{esc} is the escape velocity, v_{ratio} is the ratio of the wind velocity at infinity on the latter, R_c is the companion's radius and r is the distance from the center of the star. Given its dependance on the only radial coordinate, the geometry of the gas cloud to simulate was obviously chosen to be spherical.

In performing our fit, four parameters were made vary:

- The inclination angle i, from which, together with the mass function of the pulsar, the companion mass M_c and the orbital separation a were estimated.

- The companion's radius R_c. Although there exist a relation between mass and radius for main sequence stars, we preferred to leave it as a free parameter.

- The quantity $\dot{M}/v_{\text{ratio}}$.

- The offset Δ. The value of DM obtained from the timing solution is supposed to represent the contribution only due to the ISM and it is the baseline from which we measure deviations. However, the extracted baseline might be lower or higher than the actual value of DM due to the ISM and Δ accounts for this possibility.

The result of our fit is shown in Figure 4.9. As is visible at first glance, the agreement with Madsen's result is excellent. Quantitatively speaking, both in Madsen's and in our results the reduced chi square found was $\tilde{\chi}^2 = 1.04$, confirming the goodness of the fit. In all the calculations the pulsar mass was conventionally set to 1.4 $M_\odot$. The procedure we adopted was the brute-force fit routine on the data, over restricted ranges of the parameters. After some trials, we resolved to use the following, physically meaningful, ranges:

- $i = (45.8 \div 63.0)°$

- $R_c = (4 \div 20)$ $R_\odot$

- $\dot{M}/v_{\text{ratio}} = (1.5 \div 18.0) \cdot 10^{-10}$ $M_\odot/\text{yr}$

- $\Delta = (0.05 \div 0.80)$ pc cm^{-3}.

The best fit parameters and the relative reduced χ^2 with the 1σ uncertainties are listed in Table 4.2, along with the corresponding values obtained by Madsen.

The very close values allowed us to be confident that the code was working well also in the presence of a non-zero orbital eccentricity.

DM offset best-fit parameters			
Parameter		Madsen et al.	BWP simulation code
i	$[°]$	53 ± 7	52.1 ± 0.6
R_c	$[\mathrm{R}_\odot]$	8^a	8.0 ± 0.5
$\dot{M}/v_{\mathrm{ratio}}$	$[\mathrm{M}_\odot/\mathrm{yr}]$	$9^{+2}_{-3} \cdot 10^{-10}$	$(12.6 \pm 0.4) \cdot 10^{-10}$
Δ	$[\mathrm{pc\ cm}^{-3}]$	$0.41^{+0.15}_{-0.12}$	0.47 ± 0.04
$\tilde{\chi}^2$		1.04	1.04

^{a}The error in this parameter was not reported by Madsen,
since it was obtained interpolating over the relevant range of
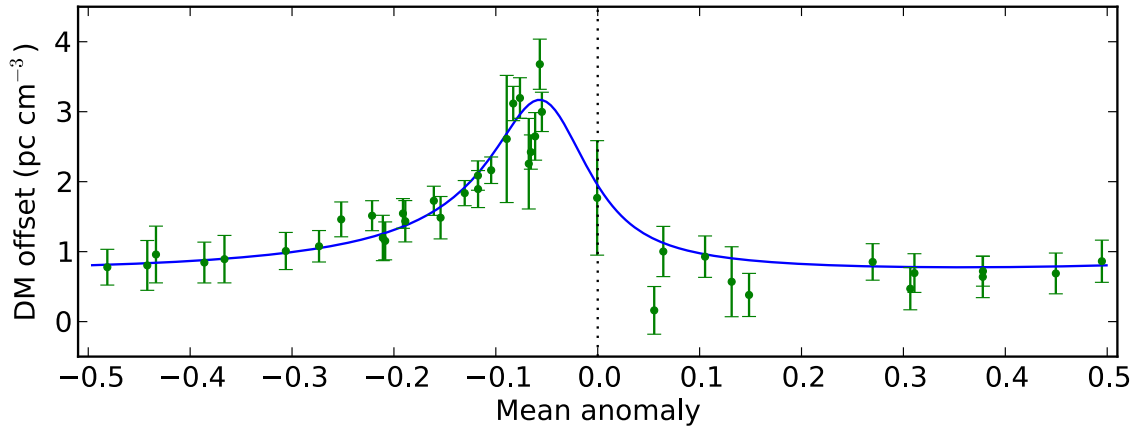main-sequence masses in Table 15.8 in Cox (2000).

Table 4.2

Figure 4.8: Observed dispersion measure offsets and best-fit curve as computed by Madsen et. al. over four orbits with a simple stellar wind model. The data come from different telescopes at different frequencies.
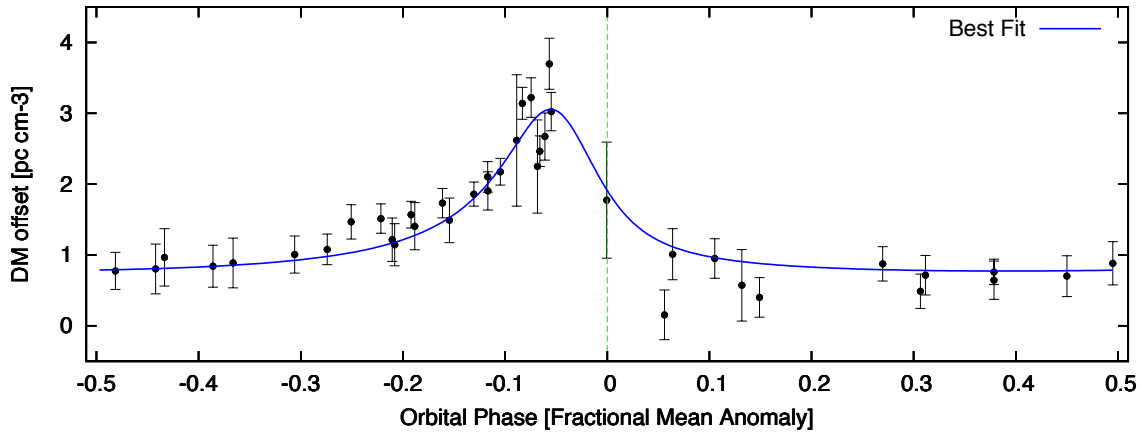

Figure 4.9: Same data as above but fitted with our simulation code using the same stellar wind model.

Chapter 5

The eclipsing binary pulsar PSR J1701-3006B

5.1 Overview

Discovered during the Parkes Globular Cluster Survey (PKSGC) in 2000 [1], it is a very puzzling object. It has been found close to the center of mass of NGC 6266, a very massive and bright ($M_V = -9.19$) globular cluster, which is also the fifth-richest of MSPs. To date, six[1] millisecond pulsars were found in it.

Like all the other five sources spotted in the cluster, the object is a millisecond pulsar, part of a short-period binary system with a very tight orbit ($a_p \sin i \simeq 0.11$ R$_\odot$). Together with PSR J1701-3006E, PSR J1701-3006B boasts a feature that makes it different from the others: the presence of irregular radio eclipses.

Over a time span of about 10 years, timing observations (typically of 30-60 minutes each in duration) performed at Parkes at the frequency of 1390 MHz, have led to the determination of a timing solution, whose parameters are shown in Table 5.1. Unfortunately, like for all the pulsars found in any globular cluster, the great distance ($d \sim 6.9$ kpc [11]) makes it an apparently faint source. We can see at a glance that the spin period derivative $\dot{P}$ is negative, suggesting an acceleration a_l toward the observer, high enough to overcome the positive intrinsic spin-down $\dot{P}_i$. The Shklovskii effect[2] and the Galactic potential cannot alone account for it and the responsible must be the globular cluster potential well[3]. This, together with its position, very close to the cluster center, are clear clues giving support to the association of the pulsar with NGC 6266.

Additional analyses, both with timing and optical data, allowed to infer many dynamical parameters of the cluster which, in turn, have put significant constraints both on the age and on the surface magnetic field of the pulsar. In fact, to be consistent with the cluster's age, the characteristic age of PSR J1701-3006B must be greater than ~ 1.3 Gyr.

---

[1]http://www.naic.edu/-pfreire/GCpsr.html

[2]The Shklovskii effect is a classical effect due to the pulsar transverse motion.

[3]Any acceleration of the pulsar along the line of sight contributes to an apparent period derivative of $\dot{P} = a_l P / c$.

PSR J1701-3006B		
Right Ascension (J2000), RA	[hh:mm:ss.sss]	17:01:12.67092(22)
Declination (J2000), DEC	[dd:mm:ss.sss]	-30:06:49.027(18)
Spin period, P	[ms]	3.59385221732417(26)
1st Period Derivative, $\dot{P}$	[10^{-19} s s^{-1}]	-3.496730(10)
2nd Period derivative, $\ddot{P}$	[10^{-31} s s^{-2}]	3.8(10)
Dispersion Measure, DM	[pc cm^{-3}]	113.44(8)
Orbital Period, P_b	[days]	0.1445454318(10)
1st Orbital Period Derivative, $\dot{P}_b$	[10^{-11} s s^{-1}]	-0.482(8)
Eccentricity, e		0^a
$a_p \sin i$	[ls]	0.252770(6)
Flux Density at 1400 MHz, S_{1400}	[mJy]	0.3(1)
Derived Parameters		
Characteristic Age, τ_c	[Gyr]	$\gtrsim 1.3$
Mass Function, $f(M_p)$	[M$_\odot$]	0.000829944(4)
Spin-Down Power, L_p	[erg/s]	$3.7 \cdot 10^{34}$
Surface Magnetic Field, B_S	[G]	$\lesssim 4.0 \cdot 10^8$

^{a} given its very small value, we fixed the eccentricity to 0 in our calculations.

Table 5.1: Physical and orbital parameters obtained by timing observations for J1701-3006B.

Correspondingly, this sets an upper limit on the magnetic field, which must necessarily be $\lesssim 4.0 \cdot 10^8$ G, a very plausible value for any millisecond pulsar.

5.1.1   Phenomenology of the pulse variations along the orbit.

The object shows strong distortions on the pulsar signal and on the times of arrival of the pulses at ~ 1.4 GHz near superior conjunction. The beginning and end of the pulse distortions usually occur at orbital phases 0.15-0.20 and $\sim$0.35, respectively, displaying a slight asymmetry with respect to the canonical center of the eclipse ($\phi = 0.25$) and exhibiting excess propagation delays (Figure 5.2a). Thus, the phenomenon covers about 20% of the orbit, with random irregularities both in the length and in the appearance (Figure 5.1). Hereafter, for simplicity, we will refer to all these effects (distortions and delays in the pulsed signal) with the word "eclipse" of the signal, even though in the vast majority of the orbit no real disappearances of the signal are occurring (see later).

As for other such objects, the excess time delays are thought to be due to the presence of outflowing gas off the companion: the increased column density would change the DM and thus the propagation speed of the signal.

Even if very useful, a frequency-dependent analysis of the behavior of the delays of the observation, by splitting the 256-MHz band, has not been possible so far because of the faintness of the signal. The low S/N could also be due to the smearing of the pulses; considering the observed delays of $\Delta t_a \lesssim 2$ ms at 1.4 GHz, the corresponding ΔDM can be responsible for a broadening of about 80% of the intrinsic pulse width over the receiver bandwidth. This also indicates us that the pulsed signal cannot disappear, after summing

the frequency channels, only because of this effect; as a confirmation of that, the pulses are usually visible all over the orbit.

The display of the eclipses itself let us guess that the inclination i cannot be small. Some simple considerations [1] related to the measured mass function, orbital inclination and the eclipsing gas region, lead to the conclusion that the radius R_E of this latter must be larger than that of the Roche lobe, R_L ($R_E \gtrsim 0.8$ R$_\odot$, whereas $R_L = 0.26 - 0.34$ R$_\odot$), no matter what mechanism one is considering. This implies that the gas must continuously be replenished by the companion itself, an unambiguous evidence in support of the fact that the companion is undergoing mass loss.
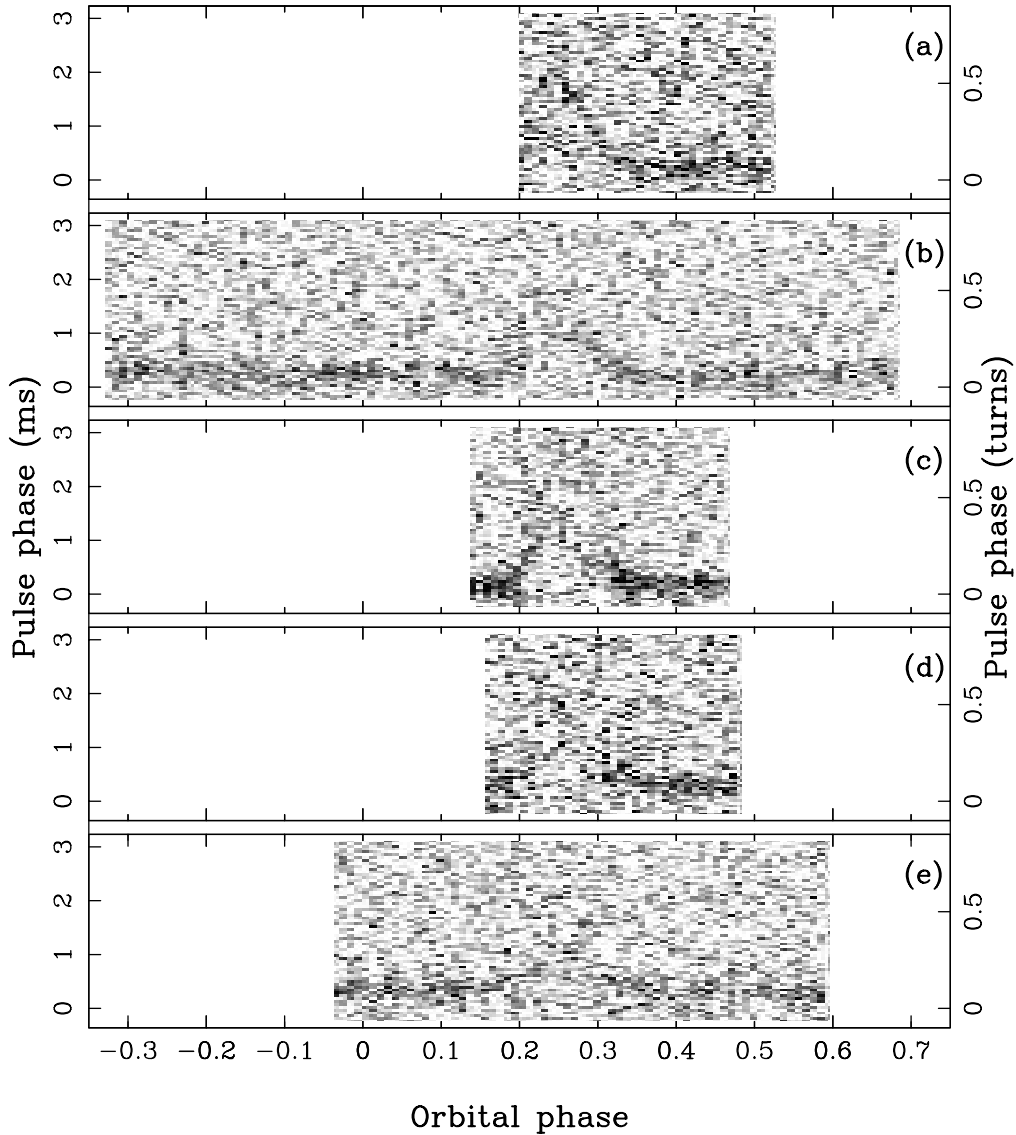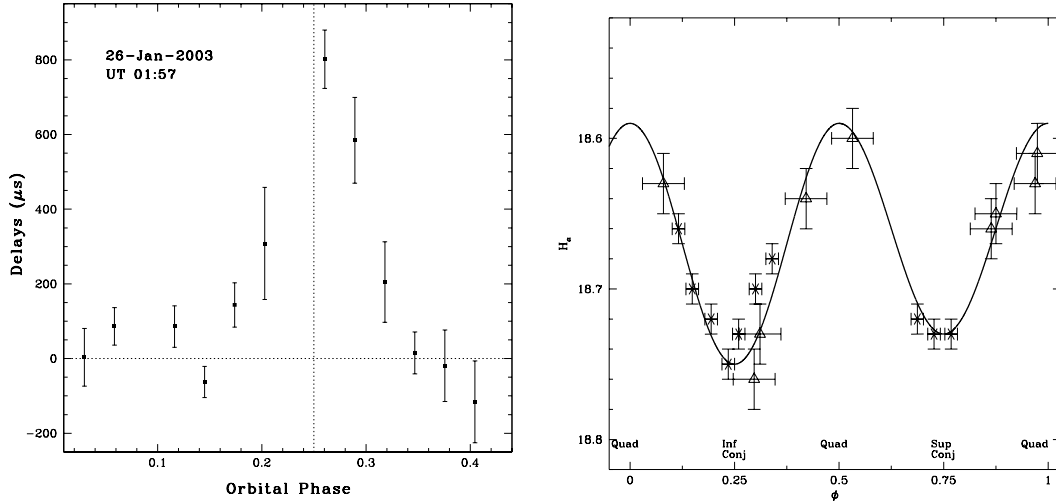

Figure 5.1: Pulse intensity as a function of both the orbital and the pulse phase for five different observations made at a central frequency of 1390 MHz. Evidently, pulse delays occur around superior conjunction $\phi = 0.25$. Note that the signal is almost always visible, suggesting that both absorption and smearing processes are normally not really significant.

(a) Grouped excess time delays around superior conjunction relative to an observation made at 1390 MHz on January 26, 2003. The error bars are twice the nominal uncertainties on the pulse arrival times [1].

(b) H-α magnitude versus orbital phase. The shape of the light curve is that typical of a deformed star, whose apparent size results larger at the two quadratures, $\phi = 0.0$ and $\phi = 0.5$ [17].

Figure 5.2

5.1.2 Optical studies: the puzzle about the Roche lobe overflow.

Observations in different parts of the electromagnetic spectrum have also been made. Indeed, nearly coincidently to the nominal position of the source, both an optical and an X-ray counterpart were found [17]. The former has then been confirmed to be associated with the low-mass companion, whereas the latter might be a consequence of the interaction between the pulsar wind and the evaporating gas from the companion itself. Data from the Hubble Space Telescope has allowed to plot the color-magnitude diagrams for all the stars of the cluster which were in the field of view of the instrument. The optical counterpart to PSR J1701-3006B has been found to have an anomalous red color, which implies that it must be out of the main sequence phase; in particular, the companion is located in the region of the color-magnitude diagram between the white dwarf sequence and the main sequence. A significant mass loss during the evolution of the system may be the origin of this peculiar location.

In addition to this, an H-α excess results, suggesting the presence of ionized gas throughout the system. The relative light curve (Figure 5.2b) displays two maxima at the two quadratures ($\phi = 0$ and $\phi = 0.5$) that is typical of tidally deformed stars.

All of these observed features point toward a tight binary system in which a non-degenerate low-mass companion is bloated by tidal forces due the neutron star, prompting a heavy mass loss.

Using the observed parameters of the cluster along with the color-magnitude diagram, one gets an effective temperature for the companion of $T_{\text{eff}} \sim 6000$ K, a bolometric luminosity of $L_{\text{bol}} \sim 1.9$ L$_\odot$ and a radius of $R_c \sim 1.2$ R$_\odot$. Under the picture described above, one should also expect the radius to be very close to Roche lobe size. However, using the

timing results, an assumed mass of the neutron star of $M_p = 1.4$ M$_\odot$ and an inclination[4] of $i \gtrsim 20°$, the inferred ranges both for the companion mass and for its Roche lobe radius turn out to be $M_c = 0.125 \div 0.41$ M$_\odot$ and $R_L = 0.26 \div 0.40$ R$_\odot$, respectively. Hence, independently of the right value of the system inclination, the optically derived stellar radius results by far larger than the expected Roche lobe radius of about a factor of 3. The only way to match the Roche lobe radius with the observed companion radius would be supposing $i \sim 3°$, but this possibility must be excluded both for the presence of eclipses and for the improbable implied companion mass of ~ 6 M$_\odot$.

The characteristics outlined so far induce us to regard PSR J1701-3006B as part of the *Redbacks* sub-class of eclipsing binary pulsars.

5.2 Data reduction and analysis

What we would like to do now is to investigate the system, with a special regard to the eclipses. To achieve that, we will basically compare observational data with theoretical plots obtained from the code we developed and make some considerations starting from our results. The aim is to put some constraints or to derive some meaningful hypotheses on the nature of both the plasma cloud and the companion. For example we would like to understand how the former might look like in its shape and density. This investigation is very important in order to plan and later analyze the data of additional observations which will be available with current and future instruments. Thanks to this well tailored observations strong constraints on the physical parameters and processes occurring in the system may be inspected.

5.2.1 Observational data

The observations we used were made with the 20-cm multibeam receiver of the Parkes radio telescope with the aid of the high-resolution filter-bank, consisting of 512 channels, each 0.5-MHz wide, for a total band pass of 256 MHz centered at the frequency of 1390 MHz. The filterbank was used to minimize pulse smearings due to dispersion [1].

The data has been acquired over a time span of about 11 years (4030 days). Thanks to our very good knowledge of the spin period and the column electron density (i.e. the DM) due to the ISM along the line of sight, we scrunched the observations in frequency[5] to increase the S/N, and found the best timing solution for our data set, based only on the off-eclipse TOAs. Then we exploited it to re-extract the residuals over all orbital phases. The result is shown in Figure 5.3. Given the extremely small eccentricity (actually negligible) which resulted from the timing solution, we decided to set it to zero in the process of re-extraction. In this way we were allowed to use perfectly circular orbits in our simulations. We can note that the pulsed signals (and, consequently, the TOA residuals) are present throughout the orbit and no significant decrease in the number of the TOAs can be appreciate around orbital phase $\phi = 0.25$ (see e.g. Figure 3.6). That means that we

---

[4]This is a conservative assumption, given that the presence of radio eclipses suggests that the inclination should not be small.

[5]That is, summing the different channels to obtain a unique time series.

cannot consider this effect as a "true" eclipses, in the sense that we do not witness a complete signal disappearance.

Re-binnig

Sometimes it is convenient to work with less but more meaningful data. As a matter of fact, when studying the residuals, we often have hundreds or thousands of values and we can assume them to follow gaussian statistics. Having a look at Figure 5.3 we can note that the points are heavily scattered all over the orbit. The cause of such an irregular behavior is to be ascribed to the fact that the TOAs are relative to a lot of different orbits occurred in different periods of time. Besides existing possible differences from one single orbit to another, we also recall the fact that our data span 11 years and in such a long time it is quite unlikely that the plasma cloud did not undergo any detectable change. Rather, its parameters have probably varied, thus causing the scatter of points we observe, especially when the signal is more deeply affected by the presence of ionized gas. An averaging process can give a reasonable way to overcome this issue.

Since, in the case of PSR J1701-3006B, we started with a very large number (4416) of TOAs, we decided to bin them in uniform orbital intervals. In this way we got a data set with a better statistics to work with. Obviously, the drawback is that the parameters we are going to get by fitting the binned data, will only be estimates of their "mean values". However, given the very poor knowledge of the properties of both the companion and the eclipsing cloud, we can be fairly happy and settle for them.
It is worth remarking the importance of choosing a proper number of bins, as a result of a trade-off between resolution in orbital phase and "smoothness" of the resulting data. For example, using a small width for the intervals, we have less points falling in each one and the consequence will be a highly jagged histogram; we will thus have no hope to reproduce the exact trend with our fairly simple model and, on the other hand, the plot itself is not probably a faithful representation of the "true" average nature of the residuals. We must therefore use wider bins, obtaining less resolution but more smoothness.

Formally, we assign to each bin a value that is an arithmetic mean of all the points falling in it:

$$\bar{y} = \frac{1}{N} \sum_{k=1}^{N} y_i \tag{5.1}$$

The use of simple arithmetic mean is justified by the above arguments, according to which we could not regard the data that fell in each bin as different measures of the same observable, given the irregular behavior and the dynamic nature of the gas cloud. The corresponding uncertainty of the bin value is the so-called *standard error of the mean*:

$$\sigma_{\bar{y}} = \frac{s}{\sqrt{N}} = \frac{\sqrt{\frac{1}{N-1} \sum_{i=1}^{N} (y_i - \bar{y})^2}}{\sqrt{N}}. \tag{5.2}$$

Here s is the standard deviation (i.e. the root mean square deviation from the mean), N is the number of residuals which fall in the bin and y_i are their values. Also, we associate a particular orbital phase with each bin that is, again, the arithmetic mean of the orbital phases of all the points that fell in that bin. It will also be used by our code to calculate the

theoretical values only at those orbital phase where an experimental measure is present, in order to save precious computational time.

After some trials, we opted to group the data in 50 intervals, therefore each representing $7.2°$ in orbital phase.

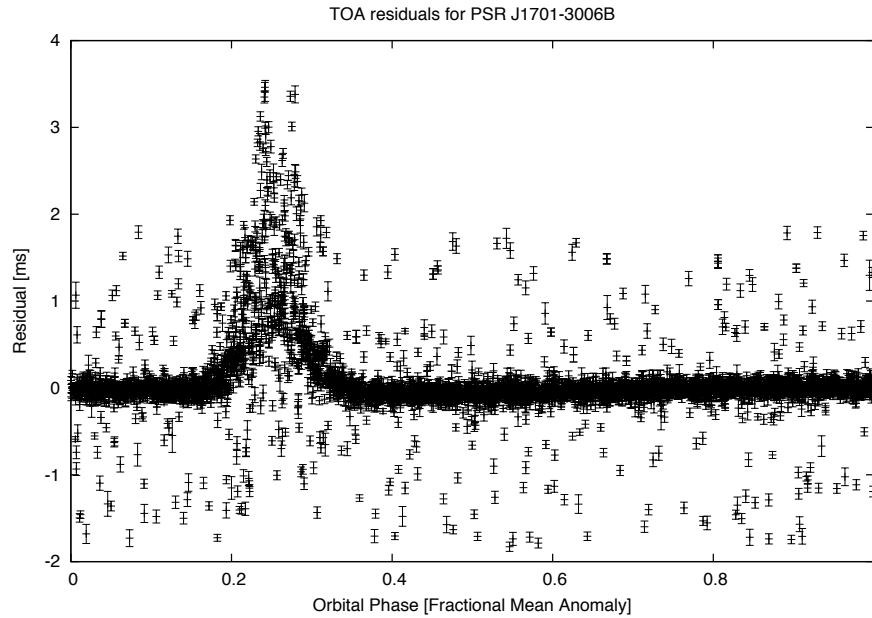Figure 5.3: Experimental TOA residuals for PSR J1701-3006B as acquired over a time span of 11 years. The increases due to the plasma cloud are evident. The observations were made at 1390 MHz, with a bandwidth of 256 MHz, 512 channels, each of 0.5 MHz.
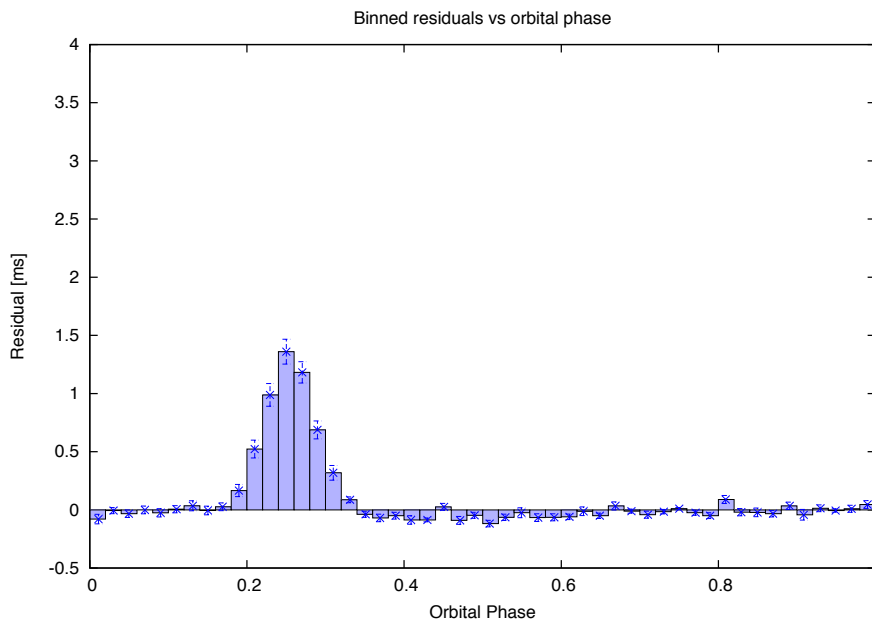

Figure 5.4: The same residuals as above but averaged in 50, equally wide, bins. The associated errors have been calculated with the simple *standard error* formula.

5.2.2   Preliminary considerations

Before running the numerical code, we can make some simple analyses based on the resulting plot of the TOA residuals versus the orbital phase, which can give us some insights into the physics of this object. This will also be helpful for understanding if the code results are compatible with our intuition and preliminary estimates. For example:

- From the fractional orbital phase interval $\Delta\phi$ defined by where excess time delays start and end, we can have an idea of the ionized cloud size by simple geometrical reasons. By making the simplifying assumption of a spherical cloud centered on the companion, the radius of the eclipsing region can be expressed as:

$$R_E = a \sin\left(\frac{\Delta\phi \cdot 2\pi}{2}\right) \qquad (5.3)$$

  In the case of PSR J1701-3006B we expect the cloud to have a cross section of the order of $\sim 1~\mathrm{R}_\odot$.

- From the magnitude of the residuals during the eclipse phases, once the size of the cloud is approximately known, we can get a direct estimate of the order of magnitude of the density of the ionized component, well inside the cloud. We can recall eq. (3.11) and make the approximation $\Delta\mathrm{DM} \sim R_E \cdot \langle n_e \rangle$. Here the $\langle \ldots \rangle$ indicates the mean value and R_E is the length scale for the size of the cloud. Solving for $\langle n_e \rangle$, we get:

$$\langle n_e \rangle \sim \Delta t_a \cdot \frac{2\pi m_e c}{e^2} \cdot f_{obs}^2 \cdot \frac{1}{R_E} \qquad (5.4)$$

  From the graph, we can find a maximum observed $\Delta t_a \simeq 1.3$ ms at $\phi \simeq 0.25$ which, combined with the other quantities ($f_{obs} = 1.4$ GHz, $R_E \sim 1~\mathrm{R}_\odot$), gives us an estimate for the electron number density of $\langle n_e \rangle \sim 10^7~\mathrm{cm}^{-3}$.

- If we see the residuals of the pulses over the whole orbit, we are sure that no significant absorption processes are occurring. Conversely, if we *do not* see any residuals in a certain interval of the orbital phases, we do not know *a priori* whether this happens because of absorption or just because of the smearing of the pulsed component of the signal[6] For PSR J1701-3006B, we can have an idea at this regard by looking at how many residuals fall in each bin over the binary orbit. Since we have a large number of data, we can safely assume to have the orbit uniformly sampled, so that a lower number of points in a particular bin has necessarily to be ascribed to some particular cause like, indeed, absorption. Having a look at Figure 5.5a we can notice that there is no evidence of substantial decreases in the number of residuals at any of the orbital phases.

These considerations give us important constraints with which we have to confront.

---

[6]Remember that the TOA residuals are extracted starting from integrated pulse profiles, obtained by folding different time series of difference frequency channels (Section 2.1.1). If the DM changes in an unpredictable way along the orbit, one cannot de-disperse the signal properly, resulting in a widening (i.e. the so-called *smearing*) of the pulses, which may even lead to their complete disappearance.

Pulse widths

Our suspicions about a possible smearing due to the extra DM, is supported by the analysis of the pulse widths against the excess time delays. In figure 5.5b we can see a fairly good linear correlation (see Section 3.6.2) between the two quantities: when the pulse is delayed by the dispersing medium the pulse itself is consequently broadened. The graph was obtained by dividing the orbit in one hundred bins and summing all the pulse profiles relative to each single bin. In this way the S/N was high enough to get a reliable pulse width. In the plot are shown only the data relative to the phase interval 0.13 - 0.37. This embraces the whole duration of eclipses at 1.4 GHz as well as including some off-eclipse data (i.e. not influenced by any excess DM) that evidently cluster in the lower-left corner.
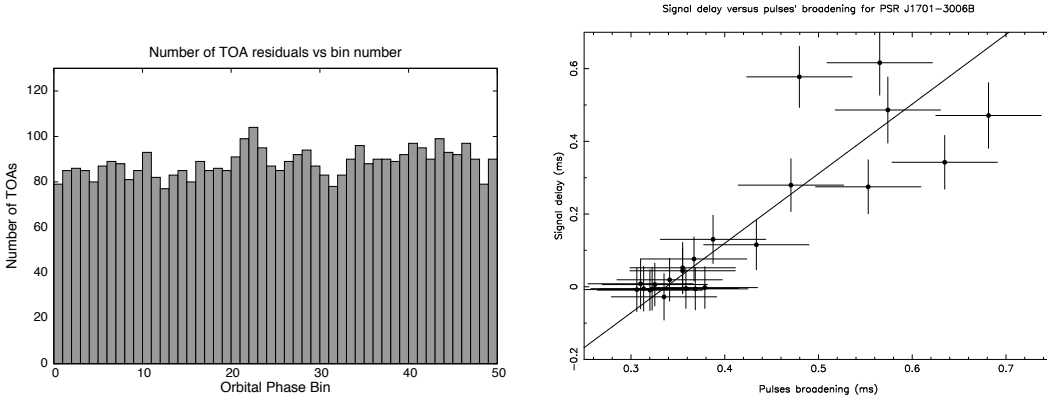
(a) Number of TOA residuals as a function of the bin number. We do not witness any substantial decrease, meaning that the pulsed signal is visible, on average, all over the orbit.

(b) Possible correlation between pulse delays and DM smearing, a clear evidence of the presence of an extra contribution to the DM due to the cloud (Corongiu et al, in preparation).

Figure 5.5

5.3 Least-squares fit strategy

In this section we illustrate the way we led our least-squares analysis.

Generally speaking, the exact processes involved in the emission of the gas off the companion are still poorly known. This is also true for this system which, as we have explained, presents apparently mysterious properties when seen at optical wavelengths. For this reason we decided to explore all the possible models which our code was endowed with.

At the lowest order of approximation, we started from the fact that the observed optical light curve does not show evidence of any asymmetry between the illuminated side and the dark side of the star. Hence, we first tested the simplest model of a perfectly spherical outflow with a density profile which naturally follows from the hypothesis of a constant mass loss: if we suppose the companion mass to be ejected at a rate of $\dot{M}_c = 4\pi r^2 \rho(r) v_{esc}$, where v_{esc} is the escape velocity from the system, by a simple balance equation we obtain

a power-law density profile with an index β that must be 2:

$$4\pi r^2 \rho(r) v_{esc} = 4\pi R_E^2 \rho(R_E) v_{esc} \qquad \Rightarrow \qquad n_e(r) = n_e(R_E) \left(\frac{R_E}{r} \right)^2 \qquad (5.5)$$

For this simulation, we fixed the power-law index and made the other physical parameters vary. This model is by far the simplest we could choose, but nothing seems to rule it out a priori. Since the real situation is very likely not that simple, with many factors highly influencing the dynamics of the gas outflow, we later relaxed the hypothesis of a fixed index and regarded it as a free parameter as well, always under the assumption of a spherical power-law density profile (eq. 4.1). On the other hand, the X-ray counterpart that has been found [17] showed a spectrum that is harder than the typical MSP population observed in globular clusters. This feature is typical of non-thermal processes and the most likely origin is indeed the pulsar/stellar wind interaction, which in turn implies a possible shocked gas cloud. The shape and density profile of the latter can anyway vary a lot, depending on various factors among which we certainly have the relative wind strength and the Coriolis forces induced by the orbital motion. Again, given our lack of knowledge about such detailed properties, we tried all the three bow-shaped geometries for the cloud that our code contemplated.

In performing our simulations, we gave the initial residual file to the code, which in turn binned it as explained above. We carried out a separate least-square fit for each model, in search for the combination of physical and geometrical parameters that best reproduced the observed delays, i.e. that minimized the reduced χ^2. We decided to calculate this latter only considering those bins which are evidently influenced by the eclipse processes, namely the bins around superior conjunction where excess time delays are evident. This choice was made because we are primarily interested in the eclipse mechanism and we didn't want any "contamination" from data which is very likely not involved in that.
In each case we set the possible ranges and the step of the free parameters values to span and proceeded iteratively, thickening the sampling around the best-fit values from the previous fit. The theoretical values of the pulse delays were obtained by calculating the extra DM due to the modeled gas cloud at each orbital phase, at the observing frequency of 1390 MHz.

Once we obtained the best-fit parameters, we accounted for the fact that the pulses are often detected throughout the eclipse, i.e. there seems not to be any significant absorption. We then explored the two main candidate absorption processes (free-free and Raman scattering). We recall that the opacity of the plasma for such mechanisms depends, apart from the frequency, on the ionized component density and temperature. Since the density profile has been univocally determined by the best-fit on the residuals, we looked for those temperatures profile which could allow us not to lose the signal completely over the whole orbit in the two most common astrophysical regimes, namely adiabatic ($\gamma = 5/3$) and isothermal ($\gamma = 1$) flows. Formally, we searched for those temperature profiles which made the optical depth always less than the arbitrary value of 3. It is important to note the different dependance of the optical depth for the two absorption mechanisms on the temperature T: while free-free absorption is less effective when T increases (eq. 3.8), the opposite is true for the Raman scattering (eq. 3.9). In this way, by assuming the occurrence of both processes in the gas cloud, we could derive the interval of temperatures for the gas at which the signal can actually pass through the eclipsing cloud without notable losses of intensity. The simulation results are shown in Tables 5.2-5.4.

Table 5.2: Best-fit parameters in the case of a spherical gas cloud. i: inclination, M_c: companion's mass. R_E: radius of cloud, $n_e(R_E)$: electron density at the eclipse radius, β: power-law density profile index, $\tilde{\chi}^2$: reduced chi square, γ: polytropic index. $T(R_E)$: temperature at the eclipse radius. The actual free parameters were: i, R_E, $n_e(R_E)$, β, $T(R_E)$.

Geometry	Density profile	i [°]	M_c [M$_\odot$]	R_E [R$_\odot$]	$n_e(R_E)$ [cm^{-3}]	β	$\tilde{\chi}^2$	Absorption effect	γ	$T(R_E)$ [K]
Sphere (S1)	eq. (4.1)	68.8	0.13	0.70	$10^{7.60}$	$2^\dagger$	3.60	Free-Free	1	$\gtrsim 10^{4.5}$
								Raman	1	$\lesssim 10^{7.5}$
								Free-Free	5/3	$\gtrsim 10^{4.5}$
								Raman	5/3	$\lesssim 10^{7.0}$
Sphere (S2)	eq. (4.1)	57.3	0.15	0.95	$10^{6.65}$	13	1.10	Free-Free	1	$\gtrsim 10^{5.0}$
								Raman	1	$\lesssim 10^{7.0}$
								Free-Free	5/3	$\gtrsim 10^{4.0}$
								Raman	5/3	$\lesssim 10^{6.0}$

† In this simulation the parameter was kept fixed, thereby it does not result from the fit.

Table 5.3: Best-fit parameters in the case of an ellipsoidal gas cloud. i, M_c, $\tilde{\chi}^2$, γ have the same meaning as in Table 5.2. n_e^{max}, θ_T, β, T^{max}: see Section 4.3.2 and eq. (4.2-4.3).

Geometry	Density profile	i [°]	M_c [M$_\odot$]	n_e^{max} [cm^{-3}]	Semi-major axes [R$_\odot$] × [R$_\odot$]	Tilt angle, θ_T [°]	β	$\tilde{\chi}^2$	Absorption effect	γ	T^{max} [K]
Ellipsoid (E1)	eq. (4.2)	68.8	0.13	$10^{8.80}$	2.10 × 3.15	5.0	14	2.91	Free-Free	1	$\gtrsim 10^{5.0}$
									Raman	1	$\lesssim 10^{7.0}$
									Free-Free	5/3	$\gtrsim 10^{5.5}$
									Raman	5/3	$\lesssim 10^{6.5}$
Ellipsoid (E2)	eq. (4.3)	74.5	0.13	$10^{8.90}$	2.10 × 3.15	5.5	8	3.03	Free-Free	1	$\gtrsim 10^{5.5}$
									Raman	1	$\lesssim 10^{6.5}$
									Free-Free	5/3	$\gtrsim 10^{6.0}$
									Raman	5/3	$\lesssim 10^{6.5}$

Table 5.4: Best-fit parameters in the case of a paraboloidal gas cloud. i, M_c, $\tilde{\chi}^2$, γ have the same meaning as in Table 5.2. n_e^{max}, θ_T, A, β, T^{max}: see Section 4.3.2 and eq. (4.4-4.5).

Geometry	Density profile	i [°]	M_c [M$_\odot$]	n_e^{max} [cm^{-3}]	Length of tail [R$_\odot$]	Tilt angle, θ_T [°]	A	β	$\tilde{\chi}^2$	Absorption effect	γ	T^{max} [K]
Paraboloid (P1)	eq. (4.4)	83.0	0.13	$10^{8.55}$	3.0	1.0	1.6	4.0	6.60	Free-Free	1	$\gtrsim 10^{4.5}$
										Raman	1	$\lesssim 10^{7.5}$
										Free-Free	5/3	$\gtrsim 10^{5.0}$
										Raman	5/3	$\lesssim 10^{8.0}$
Paraboloid (P2)	eq. (4.5)	74.5	0.13	$10^{8.90}$	4.0	6.0	2.2	1.2	11.16	Free-Free	1	$\gtrsim 10^{4.5}$
										Raman	1	$\lesssim 10^{7.5}$
										Free-Free	5/3	$\gtrsim 10^{5.5}$
										Raman	5/3	$\lesssim 10^{8.5}$

Table 5.5: Best-fit parameters in the case of a paraboloidal comet-like gas cloud. i, M_c, $\tilde{\chi}^2$, γ have the same meaning as in Table 5.2. n_e^{max}, C, A, β, T^{max}: see Section 4.3.2 and eq. (4.6).

Geometry	Density profile	i [°]	M_c [M$_\odot$]	n_e^{max} [cm^{-3}]	Length of tail [R$_\odot$]	C	A	β	$\tilde{\chi}^2$	Absorption effect	γ	T^{max} [K]
Cometary tail (C1)	eq. (4.6)	77.3	0.13	$10^{8.70}$	5	0.09	0.8	5.5	2.27	Free-Free	1	$\gtrsim 10^{5.0}$
										Free-Free	5/3	$\gtrsim 10^{5.5}$
										Raman	1	$\lesssim 10^{7.0}$
										Raman	5/3	$\lesssim 10^{7.5}$

5.4 Discussion

If we look at the simulation results, we can immediately notice how sensitive are some common parameters to the modeled geometry and density profile.

However, we can also recognize the accordance of some of the parameters with their expected values deduced from our preliminary considerations. First of all we expected an average electron density of about $\sim 10^7$ cm^{-3}. In all the cases we found values for n_e that are comparable with that estimate. We must not be deceived by the apparent higher figures that are reported in the ellipsoidal, paraboloidal and cometary-like cases: remembering their assumed density profiles, those are the very maximum values that are assumed to be at the pulsar-sided vertex of the cloud, implying lower densities in the inner regions so that the averaged values are indeed comparable with the guessed ones.

The retrieved inclinations are between $\sim 57°$ and $\sim 83°$ with a higher incidence of intermediate values. As a matter of fact, the upper-limit value has much less significance than the others, being proper of the second least probable model, featuring a $\tilde{\chi}^2 = 6.60$. The consequent companion mass has been calculated from the mass function assuming a pulsar mass of 1.4 M$_\odot$. In the whole range of inclinations it does not show any significant deviations from $M_c \simeq 0.13$M$_\odot$, confirming the hypothesis of a low-mass companion.

Regarding the absorption processes, the tests we performed showed that, in all the cases, the kinetic temperature at the edge of the cloud must be above $10^4 \div 10^6$ K, depending on the model, to avoid the signal disappearance due to free-free. Such temperatures are not so unlikely for the gas spilling off an ablated star. By considering the escape velocity v_{esc} from the system and the fact the star is losing mass, it is quite probable that very high temperatures are attained so that the mean square velocity due to thermal motion is comparable to v_{esc}, thus justifying a mass loss from the companion. On the other hand, the possible Raman scattering poses a upper limit for the same temperatures which are most often very difficult to reach.

5.4.1 Best-fit analysis

Let us finally compare the single models to one another. Interestingly, the one that results to be the less adequate in reproducing the data, is the paraboloidal geometry. Of the two assumed density profiles for the paraboloidal shape, the smaller reduced χ^2 is about twice the worst value that can be found in all the other cases.
On the contrary, we find the best accordance with the simplest geometry we proposed. While the inclination, the size of the eclipsing cloud and the electron density at its edge are absolutely consistent with all our previous analyses, some questions could be raised about the very high value of the power-law index. The reasons for that are a lot: the value of 13 is by far much higher than any physically consistent conceivable mechanism to make the density vary so rapidly. More importantly, extrapolating the temperature of the gas at the Roche lobe radius ($\simeq 0.28$ R$_\odot$) in the case of adiabatic flow, one gets a value of $T > 10^{10}$ K, which is obviously absurd. We could consider an isothermal rather than adiabatic flow for the gas, thus avoiding this inconvenient issue. Still, we should justify a uniform temperature by appealing to some efficient mechanism which would constantly redistribute the heat across the cloud.

In the light of our discussion, we can consider of true significance, from a statistical viewpoint, only the simulation S2, corresponding to the spherical geometry. Despite the very high power-law index (which calls for a physical acceptable explanation that, at present, we are not able to give) and the impossibility of accounting for the slight asymmetry in the TOA residuals, it is formally the only case in which the reduced χ^2 approaches the value of 1. It is thus possible to exploit this fact to retrieve some statistically interesting information, like the confidence intervals. We used the χ^2 grid that our code produced to search for the 3σ uncertainties associated with the best-fit parameters. To achieve that, we moved in the neighborhood of the best-fit value of a single parameter keeping fixed all the others, looking for the higher and lower values which caused the *non-reduced* χ^2 to increase by a quantity $\Delta\chi^2 = 9.21$. These values set the 99%-confidence level uncertainty. We repeated this procedure for each parameter of the fit and the result is shown in Table 5.6. Again, the extremely small intervals are a clear evidence of how the accordance with data is sensitive to small variations of the model.

i [°]	$n_e(R_E)$ [cm^{-3}]	R_E [R$_\odot$]	β	$\tilde{\chi}^2$
$57.3^{+0.6}_{-0.6}$	$10^{6.65^{+0.04}_{-0.06}}$	$0.95^{+0.01}_{-0.01}$	$13.0^{+0.5}_{-0.7}$	1.10

Table 5.6: Best-fit parameters and associated 3σ uncertainties in the case of a spherical gas cloud.
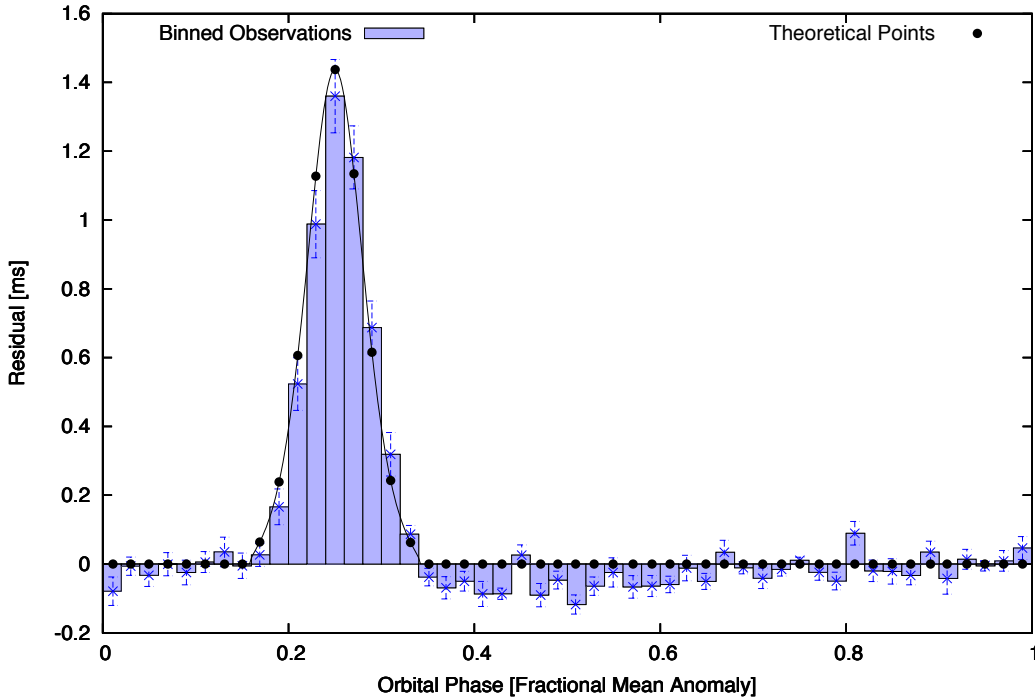

Figure 5.6: Theoretical curve (solid line) of the predicted excess time delays as a function of the orbital phase with the best-fit parameters relative to a spherical gas cloud. The filled circles are the highlighted points of the curve which have to be compared with the experimental binned residuals.

5.5   Future observations

From all that we said in the previous sections, it is easy to realize the importance of constraining the physically meaningful ranges of the involved variables. The primary way to achieve that is by using and combining data from different parts of the spectrum. In the specific case of PSR J1701-3006B, of particular usefulness to shed some light on its riddles, would be:

- A phase-resolved optical spectroscopic analysis: from the optical spectral lines we could measure the companion's radial velocity v_c^{rad}. In the case of circular orbits, the mass function of the companion can be expressed in term of this latter quantity and of the (easily measured) orbital period:

$$f(M_c) \doteq \frac{M_p^3}{(M_p + M_c)^2} = \frac{P_b}{2\pi G}(v_c^{rad})^3 \tag{5.6}$$

  Hence, we would just have to combine the mass function of the pulsar with that of the companion in order to calculate the mass ratio of the system:

$$\frac{M_p}{M_c} = \left[\frac{f(M_c)}{f(M_p)}\right]^{1/3} \tag{5.7}$$

  Given the small range of the possible masses for the neutron star, the inclination of the binary system would thus be constrained.
  Moreover, if led with high-resolution instruments, optical spectroscopy might reveal the single absorption lines and the surface gravity (GM_c/Rc^2) and hence the radius of the companion. In addition, we could also investigate the nature of the star from a chemical point of view, thus giving us other relevant clues about the dynamics of the eclipsing gas.

- New radio observations at lower frequencies: currently, we have wealth of data at 1390 MHz. This is good for timing purposes but not very much for studying the eclipse mechanism. At different frequencies we would probably witness visible changes, with respect to what we saw so far, around superior conjunction. At longer wavelengths the absorption processes become more efficient and we could see an actual disappearance of the signal. If not absorbed, we would then see higher excess time delays. At any rate, studying the behavior of the pulses at more than one frequency (even better would be performing multi-frequency observations simultaneously) can help us a lot to discriminate among possible mechanisms.

- Interferometric observations of the continuum radio signal component: especially in the case of true eclipses, which occasionally occur also in our data, the study of the non-pulsed flux could ultimately confirm our suspicion about the origin of the pulse disappearance related to the smearing. If the smearing is the cause of the phenomenon we should not see any change in the continuum flux of the source along the orbit. This kind of studies are more easily performed using an interferometer rather than a single dish.

Chapter 6

The eclipsing binary pulsar PSR J1023+0038

6.1 Overview

The second target of our study is a very peculiar one, since no other similar sources have been discovered so far. PSR J1023+0038, as explained below, could in fact represent the link between low-mass X-ray binaries (LMXBs) and radio millisecond pulsars (MSPs). It was suggested that the intermediate stage between a LMXB and a MSP is represented by a Soft X-ray Transient (SXRT) [44]. Such an object has a very erratic behavior, since it is quiescent and undetectable for most of the time but sometimes undergoes outbursts, usually lasting for days or months, during which its X-ray flux is very high. During the outburst phase the system is supposed to undergo accretion of matter onto the compact star which prevent the radio signal from being observed. On the contrary, during the quiescent phase the conditions can be suitable for the infalling material to be kept outside the light cylinder by the pressure of the neutron star's magnetic field, allowing the pulsar radio emission to be activated. In the light of these features, this class of objects is the most promising in giving us the ultimate validation of the of the *recycling model* of a neutron star in a LMXB system up to the formation of a radio millisecond pulsar. Unfortunately, until a few years ago, none of the observed SXRTs had ever been showed both signs of accretion and and pulsed radio emission.

What makes the J1023+0038 system unique is that the aforementioned bimodal behavior has been likely detected in it. In fact it first displayed in the early 2000s clear signs of accretion which, a few years later, completely disappeared. More specifically, optical studies [48, 24] showed typical behaviors of an accretion flow, such as rapid flickering in magnitude and prominent emission lines in its blue spectrum. As of 2002 such features have not been observed anymore. Rather, J1023+0038 was discovered as a millisecond pulsar in 2007 by means of the Green Bank Telescope (GBT) during a 350-MHz pulsar survey.

Timing analysis of the successive data acquired at GBT, Arecibo and Parkes, allowed the determination of the binary parameters with a very high degree of accuracy. The so obtained parameters are shown in Table 6.1. It is worth underlining the very low

PSR J1023+0038		
Right Ascension (J2000), RA	[hh:mm:ss.sss]	10:23:47.687(3)
Declination (J2000), DEC	[dd:mm:ss.sss]	00:38:41.15(7)
Spin period, P	[ms]	1.6879874440059(4)
1st Period Derivative, $\dot{P}$	[10^{-19} s s^{-1}]	1.2(8) $\cdot 10^{-20}$
Dispersion Measure, DM	[pc cm^{-3}]	14.325(10)
Orbital Period, P_b	[days]	0.1980962019(6)
1st Orbital Period Derivative, $\dot{P}_b$	[10^{-10} s s^{-1}]	2.5(4)
2nd Orbital Period Derivative, $\ddot{P}_b$	[10^{-11} s s^{-2}]	-5.21(14)
Eccentricity, e		0^a
$a_p \sin i$	[ls]	0.3433494(3)
Flux density at 1600 MHz, S_{1600}	[mJy]	~ 14 mJy
Spectral Index		$\sim$ -2.8
Companion's spectral type		G
Derived Parameters		
Mass Function, $f(M_p)$	[M$_\odot$]	0.001107
Spin-Down Power, L_p	[erg/s]	$< 3 \cdot 10^{35}$
Surface Magnetic Field, B_S	[G]	$< 3 \cdot 10^8$

^{a}again, the very small value allowed us to fixed the eccentricity to 0 in our calculations.

Table 6.1: Physical and orbital parameters obtained by timing observations for J1023+0038 [3].

eccentricity which suggests that the binary underwent classical tidal effects. Also the fairly high value ($\sim 3 \cdot 10^{-10}$) of the orbital period derivative $\dot{P}_b$ is probably to be ascribed to classical tidal torquing from the gas motion in the extended envelope of the companion star. This is not strange in the picture of a very tight system, like J1023+0038 is.

To summarize, the PSR J1023+0038 system represents the very first case in which both radio emission and accretion have been observed to occur at different times and this makes the binary particularly worthy of close investigation.

6.1.1   Eclipses

The evidence of accretion over the first years after the discovery indicates that the companion probably fills its Roche lobe [3]. This hypothesis is strongly supported by the observed regular eclipses in the radio band. The eclipse duration, as recorded at the Westerbork Syntesis Radio Telescope (WSRT) largely depends on the frequency, ranging from very brief at 3000 MHz to most of the orbit at 150 MHz. This is clearly visible in Figure 6.1. Variations in DM are also measured on short time scales of the order of minutes.

Optical spectroscopy [50] let astronomers measure the radial velocity of the companion. This allowed to estimate the system mass ratio which turned out to be $M_p/M_c = 7.1 \pm 0.1$. For a pulsar mass of $1.0 \div 3.0$ M$_\odot$, the inclination of the system was constrained to the range $53° \div 34°$. These values for the inclination implies that the line of sight will never cross the Roche lobe of the companion at any orbital phase. Hence, the eclipsing gas must be present also quite far from the orbital plane. For a Roche-lobe-filling star, one can think
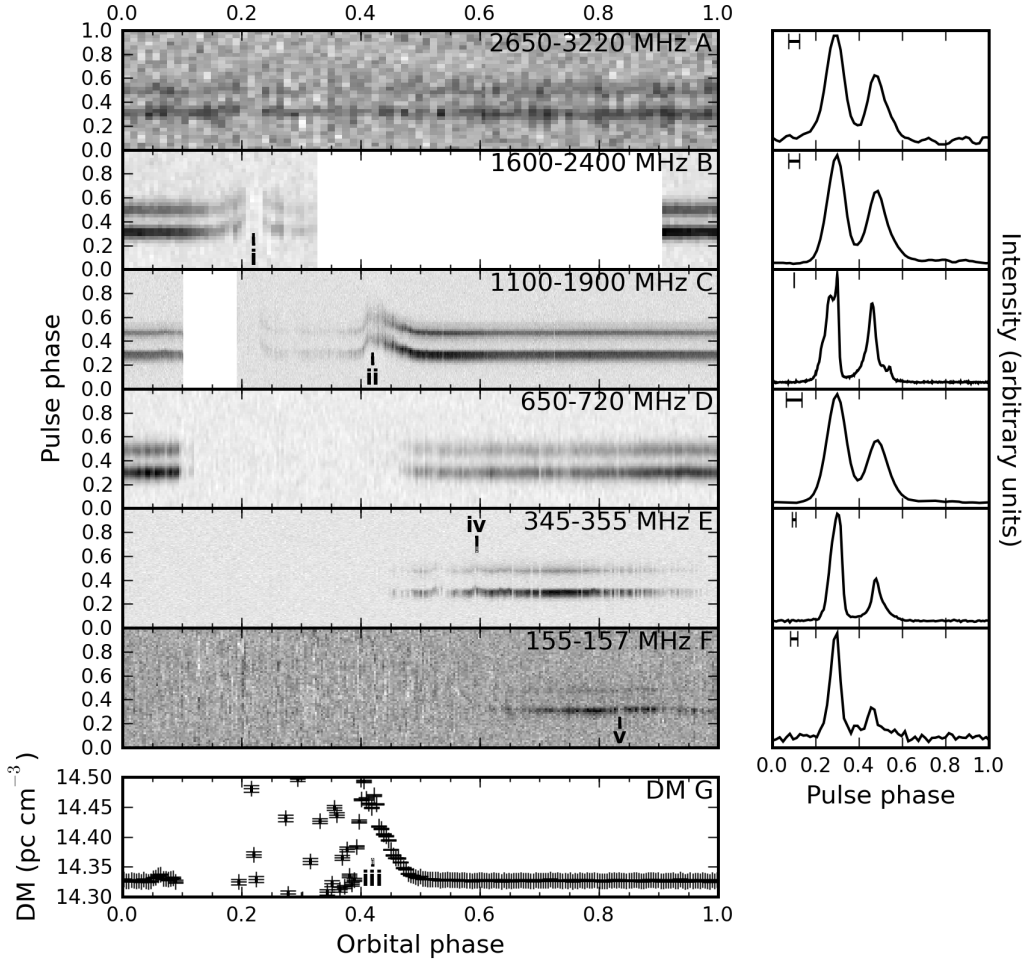
Figure 6.1: Frequency dependance of eclipses, DM variations and pulse profiles.

that the mass is lost both from inner Lagrangian point and across its whole equipotential surface, through a wind, thus allowing the gas to diffuse also far from the plane.

Recent radio astrometric observations using very long baseline interferometry (VLBI) led to the measurement of the parallax of the system, from which a very precise value for its distance was obtained, namely $d = 1368^{+42}_{-39}$ pc [2]. Combining this information with the mass ratio, the mass of the pulsar is constrained within the interval $M_p = 1.71 \pm 0.16$ M$_\odot$ directly shrinking the possible values for the inclination to the small range of $44° \div 40°$.

6.1.2 Nature and origin of the system

From the distinctive traits we have depicted so far, J1023+0038 can be classified as a *Redback* (Section 3.2.2). In this respect we could be tempted to regard it as similar to other objects, such as 47 Tuc W and PSR J1740-5340, fully recycled MSPs which show large although irregular eclipses and companions of masses in the range of $0.1 \div 0.3$M$_\odot$. The aforementioned objects are found in globular clusters and they probably coupled with their current companions in dynamical events after being spun up by a different partner.

Someone could think of a globular cluster origin for J1023+0038 too, but its great distance from even the nearest cluster actually makes unlikely the hypothesis that it was ejected from a globular cluster. Given its location in the field of the Galaxy (the short distance of ~ 1.3 kpc also allows the pulsar to be a bright source) it is very likely that the recycling phase involved its current companion, a star that has not yet been turned into a white dwarf by the process. These considerations represent the possible explanation for the connection between LMXBs and MSPs. J1023+0038 might in fact be in a bistable state [3]: according to how much the Roche lobe is filled, the source might appear as either an X-ray binary or a radio pulsar and we cannot exclude the possibility for the system to undergo a new episode of disk formation in the future.

6.2 Data reduction and analysis

6.2.1 Observational data

For J1023+0038 we started from two datasets coming from two different telescopes, namely the Lovell Telescope at Jodrell Bank, UK, and the Westerbork Synthesis Radio Telescope, Netherlands. The central observing frequencies were 1395.5 MHz and 350 MHz, respectively.

The data we had was relative to a single observation session that was made simultaneously at the two telescopes on March 13, 2009. Unfortunately, even if the two observations started at the very same instant, the Westerbork data covered two orbital periods, whereas those of Jodrell actually covered only one (Figures 6.2 and 6.3). The Westerbork original data consisted of 600 1-min long sub-integrations (for a total 10-h observation), over a bandwidth of 70 MHz split into 7 frequency channels, each 10-MHz wide. The Jodrell data was instead made up of 1841 sub-integrations, each of 10 seconds in duration (for a total 5.11-h observation) over a 73-MHz bandwidth divided into 220 sub-channels. At first glance we can immediately notice two features: at lower frequencies, the eclipses are longer and the S/N is higher, as expected according to Section 1.2.4. Once the data have been reduced[1] we extracted the timing solution with the software TEMPO2 from the off-eclipse only orbital phase data. From it, we obtained new ephemeris and installed it on the very same data. We then did the timing once again and extracted the final TOA residuals as a function of *all* the orbital phases at both frequencies. The trustworthiness of the residuals around the eclipse is very important for our analysis and hence we first summed all the frequency channels of both the datasets. Moreover, since the pulsar still resulted rather faint at 1395.5 MHz, we were compelled to sum also the relative time series in groups of 30, obtaining new sub-integrations ~ 5-min long. In this way we obviously had less orbital resolution at that frequency. Conversely, at 350 MHz the signal resulted strong and we did not need to scrunch adjacent time series; from that, we were able to extract a reliable TOA from each 1-min sub-integration. The extracted residuals as a function of the orbital phase are shown in Figure 6.4 and Figure 6.5.

Despite the overall shortage of points, the multi-frequency nature of the dataset is crucial for present and future investigations. However, for the above reasons, a meaningful multi-frequency analysis is only applicable to the first orbit.

---

[1]We removed those frequency channels in the data which were evidently affected by interferences.
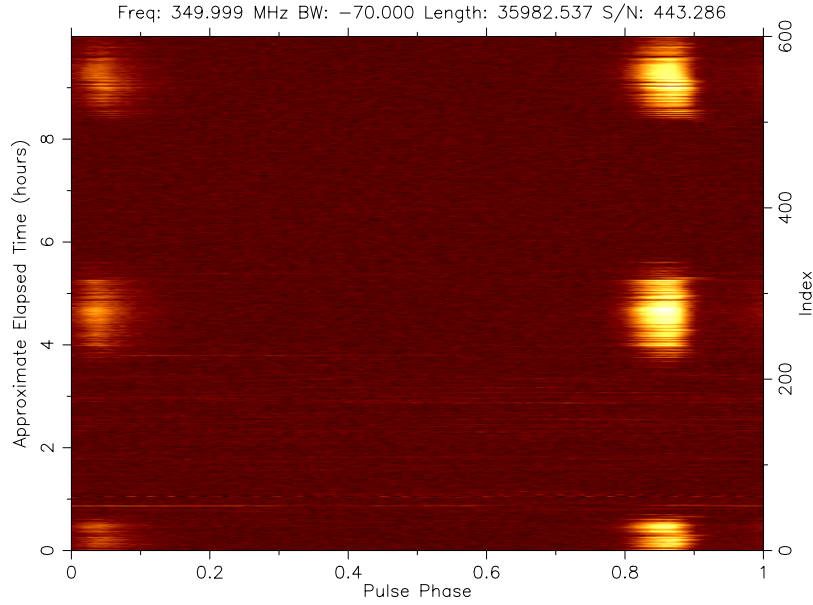
Figure 6.2: Pulse intensity against sub-integrations and pulse phase of PSR J1023+0038 at 350 MHz with a bandwidth of 70 MHz, as acquired by the Westerbork Synthesis Radio Telescope in a 10-h observation (600 × 1-min sub-integrations) which covered about two orbits. The brightest yellowish regions represent the pulsed radio signal. The eclipses are clearly visible as vertical gaps between these regions and cover more than half an orbital period.
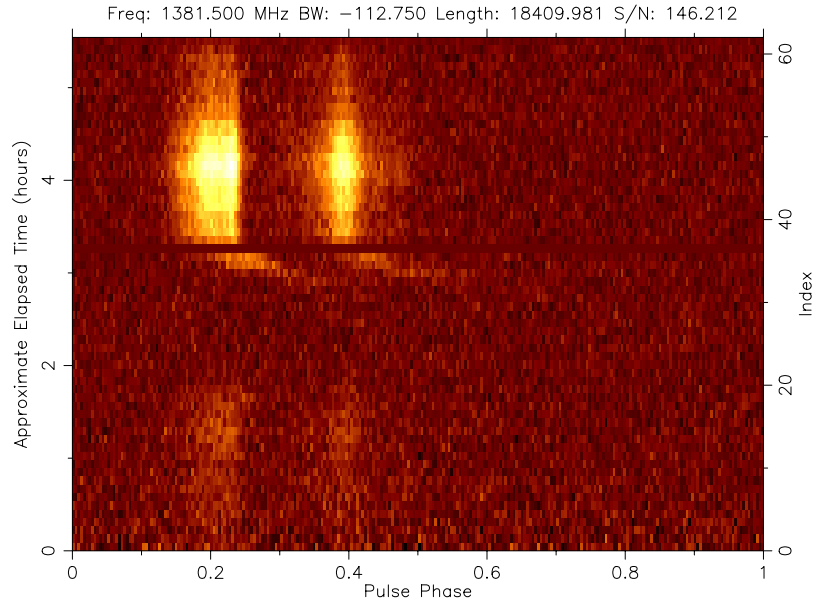

Figure 6.3: Pulse intensity against sub-integrations and pulse phase of PSR J1023+0038 at central frequency of 1395.5 MHz with a bandwidth of 73 MHz, as acquired by the Jodrell Bank Lovell Radio Telescope in a ∼ 5.1-h observation. Given the faintness of the signal at this frequency, we scrunched the sub-integrations in groups of 30, in order to increase the S/N. As expected, the eclipse duration is shorter than at 350 MHz. The gap that is visible soon after the third hour of observation corresponds to a few minutes in which the telescope had to stop tracking the source.
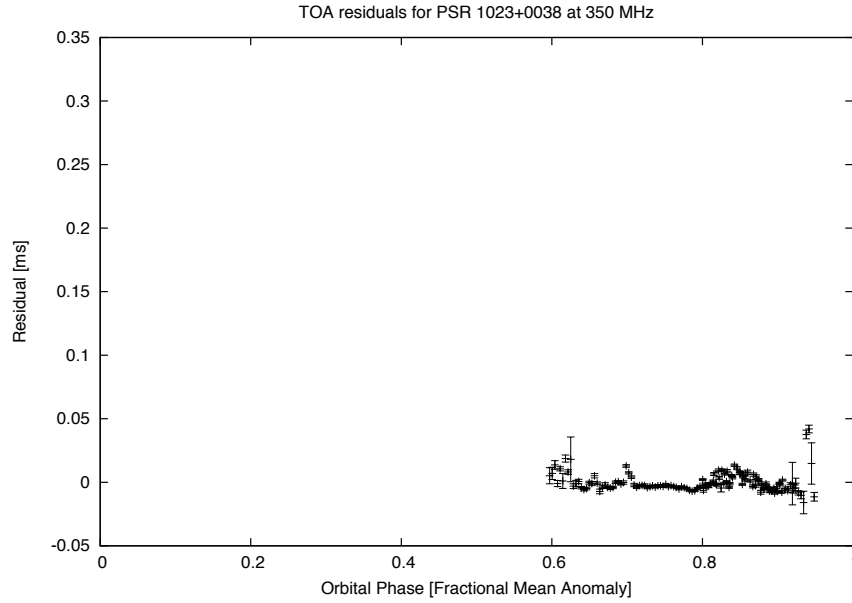
Figure 6.4: TOA residuals for PSR J1023+0038 at 350 MHz. The pulses are visible in the phase interval $\phi = 0.56 \div 0.95$. This means that the pulsed signal at 350 MHz is eclipsed for about 60% of the orbit. Its sudden disappearance suggests strong absorption as the radio wave crosses the edge of the gas cloud.
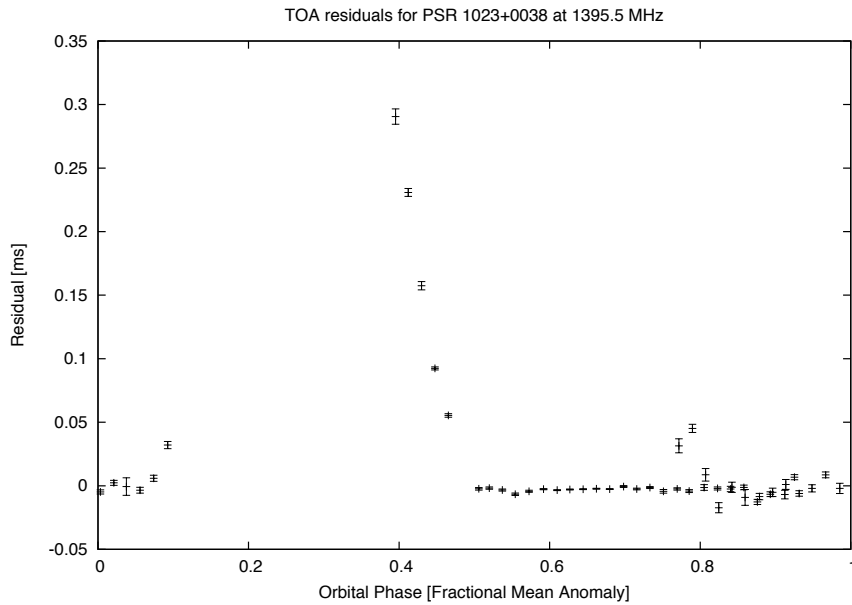

Figure 6.5: Same as above but at 1395.5 MHz. At this frequency the pulsed signal is lost at phases $\phi = 0.10 \div 0.39$, that is for 29% of the orbit. Note the evident asymmetry between ingress and egress that mimics that seen in PSR 1957+20, suggesting a corresponding asymmetry in the eclipsing plasma cloud.
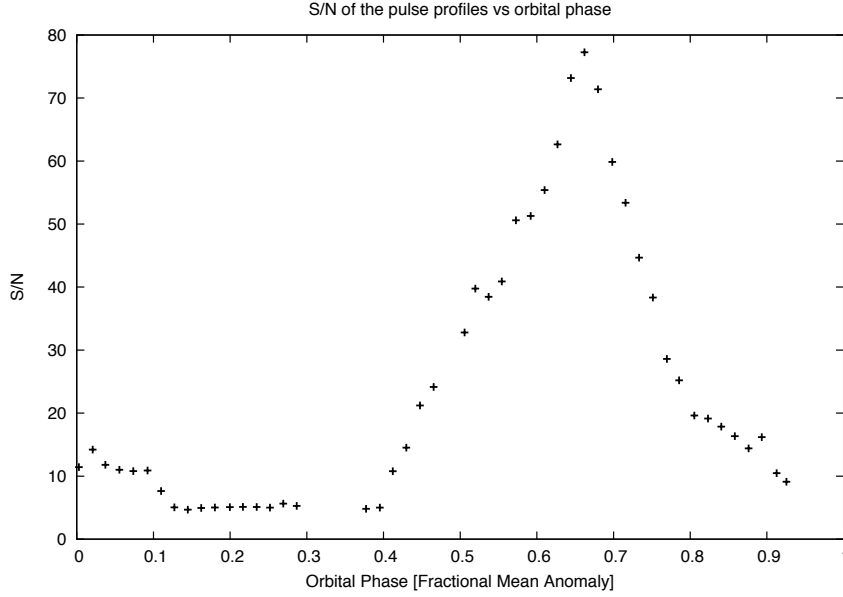
Figure 6.6: Signal-to-Noise ratio (S/N) of the pulse profiles as a function of the orbital phase. Since our data was not calibrated, we could not retrieve the absolute values of the mean flux density, S_{mean}. However, we are only interested in its relative trend. Because of the linear proportionality $S_{\mathrm{mean}} \propto$ S/N [35] we used the S/N of the folded profiles as a measure of the relative fluxes over the whole orbit.

6.2.2 Preliminary considerations

Similarly to the case of PSR J1701-3006B, we can extract some information directly from the data. As we are going to see, the most interesting characteristics are proper of the higher-frequency dataset.

- The first evidence that is worth discussing is the asymmetry in the observed TOA residuals around the eclipse at ~ 1.4 GHz. The signal disappears at phase $\phi \simeq 0.10$ to then emerge again at $\phi \simeq 0.39$. The eclipse is thus almost perfectly centered around superior conjunction. However, the excess time delays behave quite differently at ingress and egress: while they increase in an orbital phase interval of about $\Delta\phi \simeq 0.04$ before vanishing, they decrease from their reappearance in approximately $\Delta\phi \simeq 0.11$, as well as exhibiting much higher values. The first argument seems to indicate that the obscuring material might have an approximately symmetrical shape: we can think of a spherical cloud as a lowest-order degree of modeling. On the other hand, the residuals themselves suggest an asymmetry in the gas density between the leading and trailing component of the cloud, with respect to the orbital motion direction.

- Again, by using eq. (5.4) and the observed residuals at ingress ad egress at 1.4 GHz, we can give an estimate for the average densities of the gas at the edges of the cloud, soon before and after the disappearance of the signal. Given the range of possible orbital separations and assuming the eclipsing gas to be spherical in shape, we exploit eq. (5.3) to get the rough size of the cloud of $R_E \sim 1.3$ R$_\odot$. Choosing the extreme measured TOA residual values (i.e. $\Delta t_{ingr}^{\max} \sim 0.032$ ms and $\Delta t_{egr}^{\max} \sim 0.291$

ms at ingress and egress, respectively) the average electron densities turn out to be:

$$\langle n_e \rangle_{ing} \sim 5 \cdot 10^5 \text{ cm}^{-3}$$
$$\langle n_e \rangle_{egr} \sim 5 \cdot 10^6 \text{ cm}^{-3}$$

- Another apparently odd feature that can be seen in the Jodrell data is the distinct discrepancy in the registered flux of the signal before and after the eclipse. Even after our data reduction (i.e. summing adjacent sub-integrations in groups of 30), for approximately half of the orbit the pulses are barely visible. As a measure of the relative flux density as a function of the orbital phase, we extracted the S/N of the single folded profiles of our dataset; the resulting light curve is shown in Figure 6.6. Evidently, soon after the eclipse the signal results significantly brighter (see also Figure 6.3). Such a behavior can have different origins as well as being the result of a superposition of various effects.

  As a basic way to probe the possible underlying mechanism, we studied the pulse profiles in the low- and high-flux parts of the orbit. If their shape had resulted visibly different, we could have suspected of some smearing effect. However, as can be seen in Figure 6.7, this was not the case: despite the obvious increased noise in the low-flux profile[2], both its shape and the width of the two sub-pulses show little or no changes with respect to the high-flux profile. This fact induces us to invoke absorption effects as the most probable physical processes which could account for the observed phenomenon.

  Another consideration that can be made is that, in order to have a complete smearing of the 1.69-ms pulsed signal at 1.4 GHz over the 73-MHz bandwidth, we should have an increase in the DM of as much as $\Delta\text{DM} \simeq 7.5$ pc cm^{-3}; we should thus explain a sudden variation from $\Delta\text{DM} \simeq 7.5$ pc cm^{-3} to a value that is ~ 50 times lower, namely $\Delta\text{DM} \simeq 0.14$ pc cm^{-3}, that is the deduced excess DM from the first visible residual after the eclipse at that frequency ($\Delta t_a = \Delta t_{egr}^{\max} \simeq 0.291$). At the eclipse ingress and egress the excess DM deduced from the observed maximum delays $\Delta t_{ingr}^{\max} \simeq 0.032$ ms and $\Delta t_{egr}^{\max} \simeq 0.291$ are $\Delta\text{DM} \simeq 0.02$ pc cm^{-3} and $\Delta\text{DM} \simeq 0.14$ pc cm^{-3}, respectively. Hence, in order to explain the disappearance of the signal because of the smearing, one should invoke a very steep change of the DM at the edges of the eclipse . Such an enormous variation does not seem to follow the visible trend of the observed residual the eclipse egress. Therefore, this represents another clue in support of a true absorption process as responsible for the observed signal.

- The different eclipse duration at the two frequencies rules out the possibility of a plasma frequency cut-off as the mechanism provoking the eclipses. In fact, we recall the fact that such a process cannot depend on the radiation wavelength (eq. 3.10).

---

[2]the normalized average S/N in this low-flux profile is about seven times lower than in the bright part of the orbit
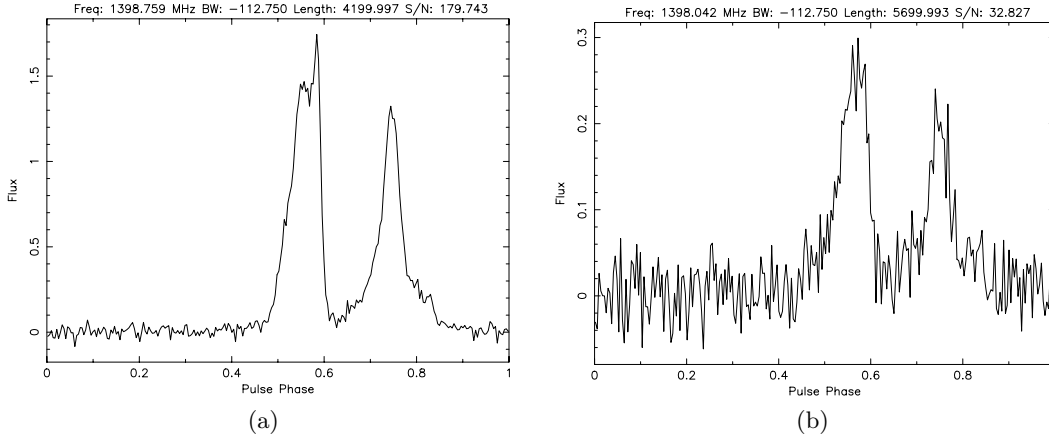
Figure 6.7: Pulse profiles for PSR J1023+0038 at 1.4 GHz relative to the "high-flux" (a) and "low-flux" (b) part of the orbit. Despite the much lower S/N, the latter does not seem to show any evident change in its shape and width, suggesting an absorption nature for the lower flux density.

6.3   Least-squares fit strategy

In the case of this source our analysis had to be necessarily different from that we did for PSR J1701-3006B. This is basically due to the larger number of observational constraints we had. In fact, every model that aims at reproducing the properties of PSR J1023+0038 coming out from our datasets, must account for the three main visible behaviors, namely:

- The excess time delays before and after the eclipse at 1.4 GHz.

- The different eclipse durations at the two frequencies.

- The peculiar light curve at 1.4 GHz.

Our ultimate goal would obviously be finding a perfect combination of the cloud geometrical and physical parameters that nicely fits the three features at the same time. As a first step in our investigation, we started trying to fit the three features separately. By studying the distinctive traits that emerge from the simulation results, we can lay the foundations for future works, hopefully arriving to a physically consistent final solution accounting for all the observed characteristics.

We recall here the small interval into which the inclination of the system was constrained thanks to interferometric parallax measures, namely $i \sim 40 \div 44°$. After some trials, we saw that the differences in the fit results obtained by varying the inclination i in that range were absolutely negligible. Hence, we decided not to leave the inclination as a free parameter and fix it to its mean value of $i = 42°$.

Since, from the previous analysis, we ruled out the hypothesis of a significant smearing in DM or a plasma frequency cut-off as responsible for the eclipses, we focused on the two absorption mechanisms that we have presented in the previous sections: free-free absorption and Raman scattering. For both, we considered the case of an isothermal ($\gamma = 1$) as well as an adiabatic ($\gamma = 5/3$) outflow for the streaming gas.
Moreover, our preliminary tests showed that all the geometries, with the exception of the

spherical one, did not allow to obtain meaningful results. As we will see, this fact is also related to the strict constraints which the fixed inclination sets. Consequently, in our final analysis, we explored only the spherical model.

6.3.1   Excess time delays

In trying to model the observed TOA residuals at the frequency of 1395.5 MHz, we followed an analogue procedure with respect to that we did for PSR J1701-3006B. The main differences from that case stem from the much smaller sample of data and the sudden disappearance of the signal.

The shortage of data has its first evident consequence in the fact that, this time, we could not bin the residuals in orbital intervals, which would have been good both for describing an *average* behavior of the system and for assigning more adequate error bars to the points we tried to fit. In particular, the uncertainties we had were those associated with the single residuals and which resulted from the previous timing analysis; clearly, they have nothing to do with the uncertainties associated with the differences from one eclipse occurrence to another, which are typically much larger. Given the smallness of the errors we had no reasonable hope, with our simple model, to obtain an acceptable fit to the data. For this reason we regarded the reduced $\tilde{\chi}^2$ just as a quality factor for comparing various models produced varying the parameters.

Just as in the case of the previous pulsar, we calculated the $\tilde{\chi}^2$ only from those points who showed evident delays between $\phi = 0.10$ and $\phi = 0.39$. However, the orbital phases of the disappearance of the pulsed signal are not of secondary importance with respect to the excess time delays trends and, in searching for the best solution, we could not neglect them. For this reason, not only did our code compute the theoretical delays due to the extra DM, but also the optical depth Γ, at each orbital phase, due to the particular absorption process we were considering. Technically, every time the optical depth overcame the arbitrary threshold $\Gamma = 3$, the code conventionally assigned the value -1 to the theoretical TOA residual. Correspondingly, we added fictitious "observed" delays with the value -1 in the data file in the phase interval where the signal was not present. As it's easy to understand, the fictitious points give a null contribution to the chi-square only when the absorption mechanism makes the signal effectively disappear in the observed orbital phase range. Thanks to this computational "trick" we were able to include the absorption as a feature to take into account in searching for the best-fit solution.

The best-fit parameter values for all the explored possibilities are listed in Table 6.2. In Figure 6.8 we show the best theoretical curve, namely the one relative to a Raman scattering, with $\gamma = 1$.

We can already note that the reduced chi squares for the examined model are all quite similar, indicating that we cannot easily disentangle the absorption processes.

Geometry	Absorption Process	$n_e(R_E)$ [cm^{-3}]	R_E [R$_\odot$]	β	$T(R_E)$ [K]	$\tilde{\chi}^2$
	Free-Free, $\gamma = 1$	$10^{6.0}$	2.1	11	$10^{4.0}$	244.92
	Free-Free, $\gamma = 5/3$	$10^{6.6}$	1.9	10	$10^{3.5}$	246.28
Sphere	Raman, $\gamma = 1$	$10^{6.4}$	2.1	7	$10^{8.0}$	239.84
	Raman, $\gamma = 5/3$	$10^{6.8}$	1.9	7	$10^{7.5}$	245.77

Table 6.2: Best-fit parameters for the excess time delays at the eclipse ingress and egress at 1.4 GHz.
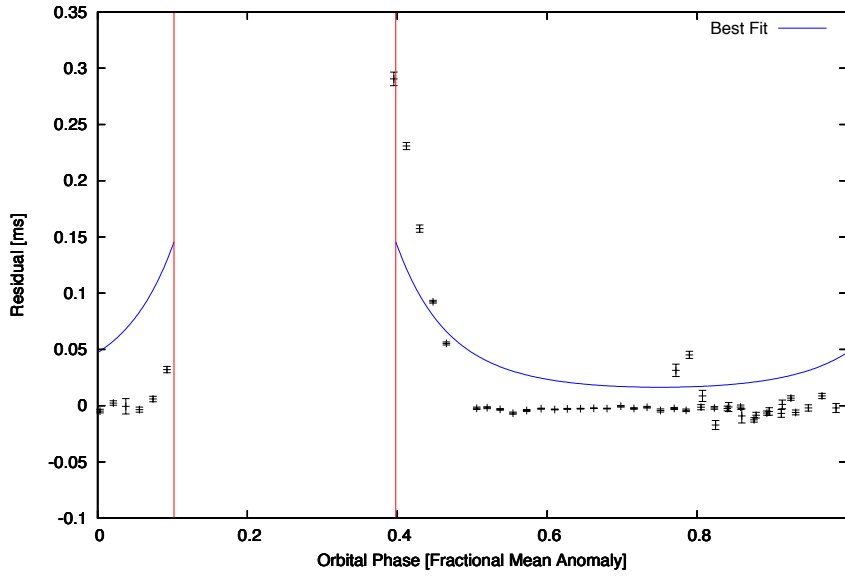

Figure 6.8: Best-fit excess time delays over the observed values, corresponding to a Raman scattering process with in an isothermal ($\gamma = 1$) spherical gas cloud with parameters: $n_e(R_E) = 10^{6.4}$cm^{-3}, $R_E = 2.1$ R$_\odot$, $\beta = 7$, $T(R_E) = 10^{8.0}$ K. The two vertical lines define the theoretical orbital interval in which the signal would completely be absorbed and hence we would not see any residual.

6.3.2   Eclipse duration at different frequencies

For the eclipse durations we exploited the simultaneous data we had at 350 MHz and 1.4 GHz. As also indicated in Figure 6.4 and 6.5, the eclipse manifested at orbital phases ϕ in the following ranges:

$$\phi \in [0.10, 0.39] \qquad \text{at 1395.5 MHz}$$
$$\phi \in [0, 0.56] \wedge [0.95, 1] \qquad \text{at 350 MHz}$$

We thus looked for the combination of geometrical and physical parameters which, simultaneously at the two frequencies, best reproduced the orbital phase intervals in which the signal was not visible. Again, we set the absorption threshold at $\Gamma = 3$, exactly as we did for the TOA residuals.

Because we needed to quantify how well a parameter set was able to fit the observed eclipse intervals, we operated as follows: we prepared two fictitious data files which represented

the flux density as a function of the orbital phase at the two frequencies. Both the files contained a conventional flux density of 1 at all the arbitrary chosen 100 equally spaced orbital phases, with the exception of the eclipse interval $\phi \in [0.10, 0.39]$ for the 1.4 GHz file and for $\phi \in [0, 0.56] \wedge [0.95, 1]$ for the 350 MHz file, where it took a null value. We then ran the code making it calculate the light curves at the two frequencies, imposing a theoretical maximum flux density of 1 and a null spectral index. The reason why we worked in this apparently weird fashion is this time strictly tied to the quantity we used to quantify the goodness of the fit: since we had no experimental errors (given the fictitious nature of our "experimental" data) we defined our quality factor $\mathcal{Q}$ as the simple inverse of the sum of the squared residuals for both the frequencies:

$$\mathcal{Q} \doteq \left[\sum_{350 \text{ MHz}} (\mathcal{Y}_i - y_i)^2 + \sum_{1.4 \text{ GHz}} (\mathcal{Y}_i - y_i)^2 \right]^{-1} \tag{6.1}$$

where $\mathcal{Y}_i$ are the theoretical flux densities calculated by the code and y_i are the fictitious experimental values. The reason why we chose an identical maximum flux density for the two frequencies (setting the spectral index to zero) with a value of 1 is related to the definition we gave for $\mathcal{Q}$: in this way the two frequencies had exactly the same weight in the evaluation of the overall goodness of the fit.

Table 6.3 shows the best-fit parameters for the different cases.

Geometry	Absorption Process	$n_e(R_E)$ [cm^{-3}]	R_E [R$_\odot$]	β	$T(R_E)$ [K]	$\mathcal{Q}$
	Free-Free, $\gamma = 1$	$10^{5.3}$	1.8	9	$10^{2.0}$	16.96
	Free-Free, $\gamma = 5/3$	$10^{6.8}$	1.8	7	$10^{4.0}$	15.37
Sphere	Raman, $\gamma = 1$	$10^{6.5}$	1.8	9	$10^{8.0}$	15.03
	Raman, $\gamma = 5/3$	$10^{6.5}$	1.8	7	$10^{8.0}$	15.16

Table 6.3: Best-fit parameters for the observed eclipse duration as a function of the frequency.

Even in the case of the eclipse duration, the values of the quality factors are very close to each other, presenting the same difficulties in discerning the favorite mechanism as we experienced in the previous case.

Another interesting fact that emerges is the very low values of the temperature in the case of free-free absorption in case of an adiabatic but, even more, in the case of an isothermal flow. For the latter we register a theoretical temperature of only 100 K, definitely too low a value to make the gas completely ionized, as we supposed a priori. Moreover, in the isothermal case, it is physically very unlikely to have such a low temperature throughout the cloud. In this case we should not even be allowed to consider the free-free interaction as we did. If free-free were indeed the true responsible for the eclipse mechanism, one should at least suppose that the gas is only partially ionized in the eclipse edge regions. Similar, but less stringent argument can be applied to the case of $\gamma = 5/3$, for which a temperature of 10000 K should not anyway be able to fully ionize an hydrogen gas cloud. This consideration holds true even more for heavier elements like helium.

6.3.3 Radio light curve

The last information we could exploit to get some insight into the physics of the gas cloud, was the observed pulsed flux density as a function of the orbital phase at 1.4 GHz. As already stated, we could not retrieve the exact values of the measured flux densities because our data were not calibrated. However, that was a not a big issue, since we were not interested in the absolute values but rather in their trend over the whole orbit. We thus took advantage of the linear proportionality between the mean flux density and the S/N of a folded profile [35]. We extracted the S/N values from all the sub-integrations of the only complete orbit present in the 1.4-GHz dataset, and plotted them as a function of the orbital phase. The data file was given to the code, which in turn searched for a best-fit solution by calculating the theoretical light curves at the varying parameter values. In order to compare the experimental and the calculated light curves in a meaningful way, we considered the maximum observed S/N value in our data, and used it to normalize the theoretical values.

Again, given the lack of relative uncertainties in the data, we used the same variable $\mathcal{Q}$ defined in eq. (6.1) as a measure of the goodness of the fit. The resulting best-fit parameters for the light curve are shown in Table 6.4. The best-fit curve, relative to a free-free absorption mechanism in the case of an adiabatic flow, is also shown in Figure 6.9.

Very similar considerations concerning the temperature values can be made with respect to the results of the case of eclipse duration. The same is valid for the quality factors, which are very close to one another and do not let us discriminate among the four physical configurations.
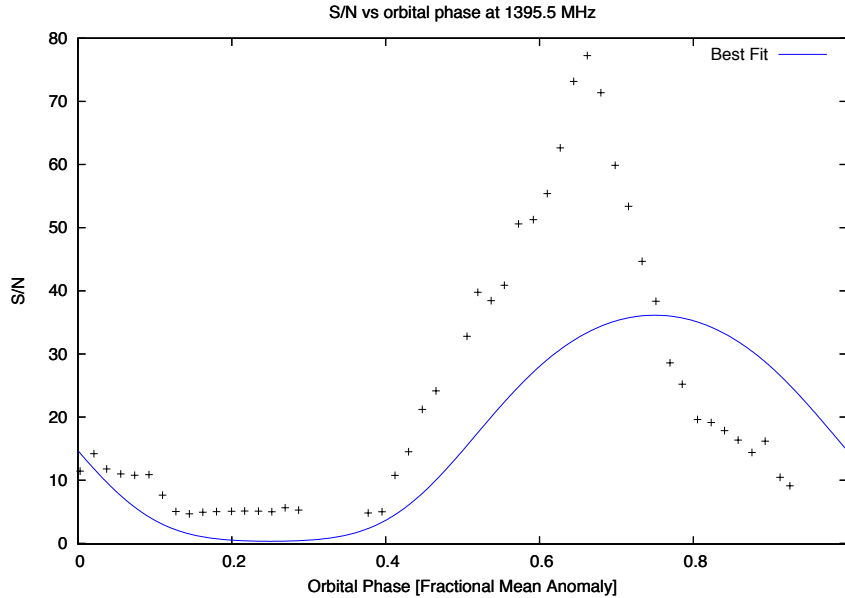

Figure 6.9: Best-fit S/N as function of the orbital phase, corresponding to the case of a Free-Free absorption process with an adiabatic ($\gamma = 5/3$) spherical gas cloud with parameters: $n_e(R_E) = 10^{6.8}$cm$^-$, $R_E = 2.3$ R$_\odot$, $\beta= 2$, $T(R_E) = 10^{3.5}$ K.

Geometry	Absorption Process	$n_e(R_E)$ $[\text{cm}^{-3}]$	R_E $[\text{R}_\odot]$	β	$T(R_E)$ $[\text{K}]$	$\mathcal{Q}$
	Free-Free, $\gamma = 1$	$10^{5.9}$	2.4	3	$10^{2.5}$	$3.84 \cdot 10^{-3}$
	Free-Free, $\gamma = 5/3$	$10^{6.8}$	2.3	2	$10^{3.5}$	$4.07 \cdot 10^{-3}$
Sphere	Raman, $\gamma = 1$	$10^{7.0}$	2.5	8	$10^{7.0}$	$2.89 \cdot 10^{-3}$
	Raman, $\gamma = 5/3$	$10^{6.8}$	2.5	6	$10^{7.0}$	$3.06 \cdot 10^{-3}$

Table 6.4: Best-fit parameters for the S/N as a function of the orbital phase.

6.4   Discussion

The first thing that can be noticed at a glance is that, in all the cases, the radius of the eclipsing cloud results larger than the orbital separation ($a \simeq 1.7$ R$_\odot$). This obviously translates into the fact that the gas is modeled as completely engulfing the neutron star, The reason for this result has to be sought in the fairly small value of the inclination that we set. At $i = 42°$, it is inevitable for the eclipsing region to extend far beyond the neighborhoods of the companion to let the system display eclipses. For a spherical geometry centered on the companion this implies a large radius which makes the cloud surround the compact object in order to account for the observations.

The first consequence of this fact is that we have non-negligible contributions from the ionized cloud to the observed properties that the code calculates at all the orbital phases. On the other hand, for some parts of the data, we can distinctly see that the effects of the cloud are barely, if not at all, visible. For instance, there is a large fraction of the orbit, at both the observing frequencies, in which the TOA residuals are visible and do not show any excess time delays at the off-eclipse phases, suggesting very little influence by the outflowing matter. The fitting procedure evidently compensate for this "flaw" with a high index of the power-law density profile, which always turns out to be higher than 6 with the only exception of the values taken in the case of the light-curve fit under the hypothesis of a free-free absorption process.

The electron density at the eclipse radius is very often found to be above 10^6 cm^{-3} and never exceeds 10^7 cm^{-3}, in agreement with our preliminary analysis derived for the TOA residuals at the eclipse edges.

Much different is the behavior of the temperature at the same eclipse radius. We can notice a striking division in its orders of magnitude between the case of free-free absorption and Raman scattering. This is not surprising if one remembers the different dependance of the optical depth on the temperature for the two processes.

6.5   Future observations

In the previous sections we have discussed the possible effects that could be invoked for explaining the eclipses that our data exhibited. We also performed several calculations with our code with different configurations, from whose preliminary results we resolved to focus on the only promising geometry, namely the sphere. However, even this latter did show distinct difficulties in reproducing the data.

The odd behaviors spotted in the data, as well as the simulations themselves, indicate that PSR J1023+0038 very likely features a complex dynamics governing the eclipsing plasma cloud and which determines a probably very irregular shape and density profile for this latter. The fact that this peculiar system recently left an accretion phase, is in all probability linked to the anomalies that are visible in its light curve as well as in other observables.

The lack of data also prevented us from trying to model the *average* properties and behaviors of the binary. Being restricted to one single orbit, we were obviously subject to the normal fluctuations that one must expect from such an unstable source. A significant example, in this regard, is the light-curve at 1.4 GHz: while our data exhibited large variations over the orbit, other observations made at similar frequencies, like the one visible in Figure 6.1, do not seem to show such an erratic behavior.

In the light of this considerations, we strongly suggest for this system:

- An extensive monitoring at the radio wavelengths: the large variations that can be seen even on short time scales can give important clues about the dynamics of both the gas and the system as a whole.

- New simultaneous multifrequency radio observations: it is important to have new simultaneous data from various telescopes or from a multi-wavelength receiver, since they could allow us to spot new peculiar behaviors which displays at the different frequencies at the very same time. This could in turn help us to put more stringent constraints to the eclipse mechanisms, thanks to their distinctive dependance on the frequency, making sure that the possible dissimilarities are not due to the potential physical variations that the cloud can easily undergo over time.

- X-ray observations: this band of the electromagnetic spectrum could give us important hints about the interaction between the pulsar radiation with its environment and, in particular, with the outflowing matter; hence, it could also reveal crucial information about the dynamics of the gas cloud. The latter can also suggest precious details which could be then implemented in our code, allowing new models to be explored.

Concluding remarks

In the present thesis we have studied a specific class of binary millisecond pulsars which have the peculiarity of showing periodical eclipses in their pulsed radio signals. This class of objects deserve particular attention because they represent the primary candidates for explaining the connection between low-mass X-ray binaries (LMXBs), visible in the X-ray band of electromagnetic spectrum, and millisecond pulsars (MSPs), which are rather observed in the radio band.

We first reviewed the main features of the two categories into which eclipsing binary pulsars can be further divided, namely Black Widow Pulsars and Redbacks. Many new systems belonging to the two aforementioned groups have been discovered in the last two years, almost tripling the total known sample. The additional wealth of the available data opened the possibility of addressing new relevant physical and astrophysical problems the study of which was, until recently, hampered by the poor statistics of the detected sample of objects. One of the longest-pending issue is the underlying mechanism which could explain the observed eclipses and, related to that, the geometrical and thermodynamical properties of the gaseous cloud responsible for them.

As part of a large observational and theoretical effort aimed at tackling these problems, in this thesis we first developed a powerful and versatile code which, with the aid of a 3D graphical output, allowed us to numerically simulate such processes in the most variegate geometrical and physical configurations, as well as to compare them with observational data. More specifically, the code contemplates four main mechanisms thanks to which the pulsed signal can disappear: they are the *plasma-frequency cut-off*, the *pulse smearing* due to a varying dispersion measure, the *free-free absorption* and the *Raman scattering*.

The code was tested on a system (PSR J1740-3052) which had been previously deeply examined, and it reproduced the already known results with a high degree of accuracy. This enabled us to apply it to two previously unexplored systems, with the goal of getting new insights into their physics and of tracing the direction toward which their future observations should point.

The first object that we investigated, PSR J1701-3006, is a binary millisecond pulsar found to belong to the globular cluster NGC 6266. This system is interesting because it does not actually show a complete signal disappearance, but only delays in the arrival times of the pulsed signal. A preliminary analysis indicated the path we had to follow in the application of the code; in particular, the never-disappearing signal, along with an apparent linear correlation between pulse delays and pulse profile widths, pointed toward a dispersion smearing mechanism as the primary actor, while absorption effects did not seem to play any significant role. We then used our 1.4-GHz data and tried to model, with

our code, the excess time delays as a function of the orbital phase through a least-squares fit procedure; in doing this, we assumed different geometries and density profiles for the ionized gas cloud. Despite its apparent simplicity, the spherical geometry (with a steep power-law density profile) resulted the most adequate in representing the data. Once we found the best-fit parameters for each configurations, we exploited the above discussed observational evidence to put some constraints on the temperature of the gas cloud. For the spherical case, we constrained the temperature at the edge of the eclipse (considering both the Raman scattering and Free-Free absorption effectively acting) in the $10^5 \div 10^7$ K range for an isothermal matter flow, and in the $10^4 \div 10^6$ K range for an adiabatic flow. We finally stressed the importance of optical observations for this system, and in particular how crucial would be a phase-resolved spectroscopy, which would allow us to heavily constrain the currently unknown system inclination.

The second object of our study was PSR J1023+0038, a system that shows all the features we would expect from a typical Redback, including true eclipses in which the signal completely disappears. Moreover, it is thought that PSR J1023+0038 could be in the very intermediate stage between a LMXB and a MSP. For this binary we exploited the multi-frequency nature of the data we had, as well as the knowledge of the inclination angle. We used our code to try to fit for the eclipse duration at the two frequencies, for the observed excess time delays and for the strange trend of the radio light-curve, all as a function of the orbital phase. Despite our efforts, the system resulted very difficult to model with the current version of our code. While the more complicated geometries directly failed in reproducing the data, the spherical geometry returned more meaningful but often conflicting results. We adduced these difficulties to the complexity of the dynamical processes which the outflowing matter from the companion is probably undergoing. For this source we remarked the importance of future extensive (possibly multi-frequency) monitoring in the radio band in order to have more data to work with. Also X-ray observations would help us to get some insights into the interaction between the pulsar radiation and the outflowing matter.

In conclusion, we have built a flexible and well-tested tool through which we will hopefully continue to investigate these interesting and puzzling objects. The addition of more realistic geometries and gas density distributions to the simulated trends, as well as the availability of further theoretical and observational data for constraining the parameters of these systems, are the ingredients of the future planned work. In fact, a lot of efforts are yet to be made. However, in the light of the very high rate at which these system are now being discovered, we are confident that many of the mysteries in which these latter are currently shrouded will be unraveled in the near future.

Appendix A

The Cavalieri-Simpson integration method

As it was evident in our discussion so far, we often had to compute simple unidimensional definite integrals numerically. The easiest way to do so is by using the Cavalieri-Simpson method, also known as the parabola method. The idea is to sample the integration domain into a finite number of intervals in which we replace the integrand function with a branch of a parabola. Let us consider the definite integral:

$$I = \int_a^b f(x)dx \tag{A.1}$$

We can substitute the integrand with a second-order rational polynomial function:

$$f(x) \qquad \rightarrow \qquad y(x) = Ax^2 + Bx + C \tag{A.2}$$

As well-known, this is the equation of a parabola with the symmetry axis parallel to the y-axis. In order to determine the coefficients A, B, C for each sampling interval we just need to know three points of the parabola.

We thus split the integration domain $[a; b]$ in n sub-intervals each of size:

$$h = \frac{b-a}{n} \tag{A.3}$$

Let us take the interval extremes of the first two sub-intervals and compute the corresponding values of the original integrand, $f(x)$:

$$\begin{aligned}
x_0 = a & \Rightarrow & y_0 = f(x_0) \\
x_1 = x_0 + h & \Rightarrow & y_0 = f(x_2) \\
x_2 = x_0 + 2h & \Rightarrow & y_0 = f(x_2)
\end{aligned} \tag{A.4}$$

Let us compute the integral of $y(x)$ in such an interval:

$$J = \int_{x_0}^{x_2} (Ax^2 + Bx + C)dx = \left[\frac{Ax^3}{3} + \frac{Bx^2}{2} + Cx \right]_{x_0}^{x_2} =$$

$$= \frac{2A(x_2 - x_0)(x_2^2 + x_2 x_0 + x_0^2) + 3B(x_2 - x_0)(x_2 + x_0) + 6C(x_2 - x_0)}{6} = \tag{A.5}$$

$$= \frac{h}{3} \left[2A(x_2^2 + x_2 x_0 + x_0^2) + 3B(x_2 + x_0) + 6C \right]$$

where we have made simplifications and have used the fact that $(x_2 - x_0) = 2h$.

By imposing that the points $(x_0, y_0), (x_1, y_1), (x_2, y_2)$ belong to the parabola and remembering that $x_1 = (x_0 + x_2)/2$ we get the following system of equations:

$$\begin{aligned} y_0 &= Ax_0^2 + Bx_0 + C \\ y_1 &= \frac{A(x_0 + x_2)^2}{4} + \frac{B(x_0 + x_2)}{2} + C \\ y_2 &= Ax_2^2 + Bx_2 + C \end{aligned}$$ (A.6)

Multiplying the second equation by 4 and summing to the others, we find:

$$y_0 + 4y_1 + y_2 = 2A(x_2^2 + x_2x_0 + x_0^2) + 3B(x_2 + x_0) + 6C \tag{A.7}$$

That is exactly the last member of eq. (A.5), so that we can write:

$$J = \frac{h}{3}(y_0 + 4y_1 + y_2) \tag{A.8}$$

Since $y(x)$ in the interval $[x_0, x_2]$ approximates the "true" function $f(x)$ by construction, we conclude that:

$$\int_{x_0}^{x_2} f(x)dx \simeq \frac{h}{3}(y_0 + 4y_1 + y_2) \tag{A.9}$$

Reiterating the procedure for each of the following couples of intervals, we trivially get:

$$\begin{aligned} \int_{x_0}^{x_2} f(x)dx &\simeq \frac{h}{3}(y_0 + 4y_1 + y_2) \\ &\vdots \\ \int_{x_{n-2}}^{x_n} f(x)dx &\simeq \frac{h}{3}(y_{n-2} + 4y_{n-1} + y_n) \end{aligned} \tag{A.10}$$

Hence:

$$\begin{aligned} \int_b^a f(x)dx &= \int_{x_0}^{x_2} f(x)dx + \int_{x_2}^{x_4} f(x)dx + \ldots + \int_{x_{n-2}}^{x_n} f(x)dx \\ &= \sum_{k=1}^{n/2} \int_{x_{2k-2}}^{x_{2k}} f(x)dx \simeq \frac{h}{3}\sum_{k=1}^{n/2}(y_{2k-2} + 4y_{2k-1} + y_{2k}) \end{aligned} \tag{A.11}$$

Summarizing:

$$\boxed{\int_a^b f(x)dx \simeq \frac{h}{3}\sum_{k=1}^{n/2}(y_{2k-2} + 4y_{2k-1} + y_{2k})} \tag{A.12}$$

that is the formula we used to evaluate the optical depth in the program.

Acknowledgements

Beyond the scientific issues which we have discussed all along, I would like to remark the "human" content which this thesis is made of. Behind the formulas important values hide: they are love, passion, friendship and faith.

My first and biggest thanks is to my parents, Fabio and Myriam. Ever since I was a child, they have always supported me in my most difficult choices. They have always encouraged me to pursue my passions. This thesis is indeed one of my dreams that came true and I regard it as a result of the love of my mother and father. Thanks to my little sister, Elena, for her love and patience demonstrated during my most nervous days. Thanks to my grandmother, Gemma, for hosting me and treating me as a "king" when studying. Thanks to all my family for supporting me over my entire career.

A great thanks is to my advisor, Prof. Valeria Ferrari which, with her fascinating lectures about General Relativity, conveyed her passion for astrophysics to me, making me ultimately understand the path that I had to follow.

A special thanks is owed to Prof. Luigi Stella. He believed in me and gave me my first concrete possibility to get in touch with the wonderful world of research. I will always be grateful to him for the incredible opportunities he gave me, which enriched me both on scientific and human grounds. Without his faith, none of all the wonderful things that has happened to me over this last year would have happened.

Among these things, is Cagliari. The people that I met there were among the best I have ever known in my life. It is very difficult for me to express how incredible this experience was.

A great thanks to my supervisor, Dott. Andrea Possenti for his kindness, his professionalism, for making me feel as a true member of the "Pulsar Group", for the magic experience he made me have at the Parkes radio telescope.

Thanks to Alessandro Corongiu, for his dedication, his patience, his daily support. A few rows does not do justice to all that he has made and to his important contribution to this thesis work.

Thanks to Marta Burgay, for her help in all that concerned timing and data analysis.

Thanks to Noemi Iacolina and Sabrina Milia, colleagues but, much more, true friends. Thank you for making my stay at the observatory, and generally in Sardinia, so wonderful. ;)

Thanks to Caterina Tiburzi, for everything. Especially for waiting me in the nighttime at the Parkes lodge the day of my arrival. :D

Thanks to Paolo Esposito, for his advices and the nice trip to the Sardinian dunes of Piscinas.

Thanks to all the administration staff of the Cagliari Observatory for the morning lifts up to the top of the hill, where the observatory was. Thank to Antonio Poddighe and Antonietta Fara, for their help in computer issues. Thanks to Matteo Murgia for his advices. Thanks to Silvia Casu, for making me realize the importance of outreach. And thanks to all the other people which made me enjoy my stay at the Observatory of Cagliari at best: Valentina Vacca, Delphine Perrodin, Andrea Tarchi, Paola Castangia, Alessio Trois, Sergio Poppi, Alberto Pellizzoni, Cesare Cecchi-Pestellini.

There are many other people outside the observatory that contributed to make my Sardinian "adventure" so magic: thanks to Mariano, Barbara, Angelo, Sandra, Elise. Thanks to my flatmate, Pierpaolo.

Alessandro a.k.a. "aridolfi" :)

Bibliography

[1] R. N. Manchester A. Possenti, N. D'Amico. Three binary millisecond pulsars in ngc 6266. *The Astrophysical Journal*, 599:475–484, 2003.

[2] W. F. Brisken S. Chatterjee G. H. Janssen V. M. Kaspi D. Lorimer A. G. Lyne M. A. McLaughlin S. Ransom I. H. Stairs B. Stappers A. T. Deller, A.M. Archibald. A parallax distance and mass estimate for the transitional millisecond pulsar system j1023+0038. *The Astrophysical Journal Letters*, 2012.

[3] I. H. Stairs Anne M. Archibald. A radio pulsar/x-ray binary link. 2009.

[4] S. P.; Brown J. C. Antokhin, I. I.; Owocki. A steady, radiative-shock method for computing x-ray emission from colliding stellar winds in close, massive-star binaries. *The Astrophysical Journal*, 611(1):434–451.

[5] M.B. Davies A.R. King and M.E. Beer. Black widow pulsars: the price of promiscuity. *MNRAS*, 2008.

[6] J. Arons and M. Tavani. High-energy emission from the eclipsing millisecond pulsar psr 1957+20. *The Astrophysical Journal*, 403:249–255, 1993.

[7] A. G. Lyne F. Camilo R. N. Manchester J. S. Sandhu M. Toscano B. W. Stappers, M. Bailes and J. F. Bell. The nature of the psr j205120827 eclipses. *MNRAS*, 321:576–584, 2001.

[8] Matthew Bailes. Transformation of a star into a planet in a millisecond pulsar binary. *Science*, 2011.

[9] C. R. Evans C. Thompson, R. D. Blandford and E. S. Phinney. Physical processes in eclipsing pulsars: eclipse mechanisms and diagnostic. *The Astrophysical Journal*, 422:304–335, 1994.

[10] A. C.; Wilkin F. P Canto, J.; Raga. Exact, algebraic solutions of the thin-shell two-wind interaction problem. *The Astrophysical Journal*, 469:729.

[11] William F. van Altena Dana I. Dinescu, Terrence M. Girard and Carlos E. Lopez. Space velocities of southern globular clusters. iv. first results for inner galaxy clusters. *The Astronomical Journal*, 125:1373–1382, 2003.

[12] M. B. Davies and B. M. S. Hansen. Neutron star retention and millisecond pulsar production in globular clusters. *MNRAS*, 301:15–24, 1998.

[13] R. W. Hellings D.C. Backer. Pulsar timing and general relativity. *Annual review of astronomy and astrophysics*, 24:537–575, 1986.

[14] M. Kramer F. Camilo G. B. Hobbs G. H. Janssen A. G. Lyne R. N. Manchester A. Possenti E. C. Madsen, I. H. Stairs and B. W. Stappers. Timing the main-sequence-star binary pulsar j1740-3052. *MNRAS*, 2012.

[15] V. Eichler, D.; Usov. Particle acceleration and nonthermal radio emission in binaries of early-type stars. *The Astrophysical Journal*, 402(1):271–279, 1993.

[16] A. S. Fruchter et al. The eclipsing millisecond pulsar 1957+20. *The Astrophysical Journal*, 351, 1990.

[17] Cocozza et al. A puzzling millisecond pulsar companion in ngc 6266. *The Astrophysical Journal*, 679:L105–L108, 2008 June 1.

[18] S. L. Shapiro F. A. Rasio and S. A. Teukolsky. What is causing the eclipse in the millisecond binary pulsar? *The Astrophysical Journal*, 342:934–939, July 1989.

[19] S. L. Shapiro F. A. Rasio and S. A. Teukolsky. Eclipse mechanisms for binary pulsars. *Astronomy and Astrophysics*, 241:L25–L28, 1991.

[20] P. C. C. Freire. Eclipsing binary pulsars. *ASP Conference Series, Vol 328*, 2005.

[21] A. S. Fruchter, D. R. Stinebring, and J. H. Taylor. A millisecond pulsar in an eclipsing binary. 333:237–239, 1988.

[22] Eichler D. Gedalin M. Nonlinear plasma mechanisms of pulsar eclipse in binary systems. *The Astrophysical Journal*, 406(2):629–637, 1993.

[23] P. Goldreich and W. H. Julian. Pulsar electrodynamics. *The Astrophysical Journal*, 157:869–880, August 1969.

[24] R. H. Becker M. S. O'Brien H. E. Bond, R. L. White. First j102347.6+003841: The first radio-selected cataclysmic variable. *PASP*, 114:1359, 2002.

[25] IAU Symposium. *Binary pulsar evolution: unveiled links and new species*, 2012.

[26] IAU Symposium. *The pulsar population in Globular Clusters and in the Galaxy*, number 291, August 2012.

[27] IAU Symposium. *Surrounded by spiders! New black widows and redbacks in the Galactic field*, volume 291, August 2012.

[28] K. S. Cheng J. Takata and R. E. Taam. On the transition from accretion-powered to rotation powered millisecond pulsars. *The Astrophysical Journal Letters*, 723:L68–L72, 2010.

[29] Jackson. *Classical Electrodynamics*. 1962.

[30] W. H Julian. Pulsar electrodynamics ii. *The Astrophysical Journal*, 183:967–971, August 1973.

[31] A.R. King and M. E. Beer. Evolution of black widow pulsars. *ASP Conference Series*, 328, 2005.

[32] B. Chen A. Henden G. Schmidt S. F. Anderson N. M. Silvestri L. Homer, P. Szkody and J. Brinkman. Xmm-newton and optical follow-up observations of sdss j093249.57+472523.0 and sdss j102347.67+003841.2. *The Astronomical Journal*, 131:562–570, 2006.

[33] V. M. Lipunov and M. E. Prokhorov. Ejection from pulsars in binary systems. *Astrophysics and Space Science*, 98:221–236, 1984.

[34] D. R. Lorimer. Binary and millisecond pulsars. *Living Reviews in Relativity*, 11(8), 2008.

[35] D. R. Lorimer and M. Kramer. *Handbook of Pulsar Astronomy*. Cambridge University Press, 2005.

[36] J. H. Taylor M. F. Ryba. High-precision timing of millisecond pulsars. ii - astrometry, orbital evolution, and eclipses of psr 1957+20. *The Astrophysical Journal*, 380(557-563), October 1991.

[37] A. S. Fruchter M. A. P. Torres M. E. Beer M. T. Reynolds, P. J. Callana and R. A. Gibbons. The light curve of the companion to psr 1957+20. *MNRAS*, 379:117–1122, 2007.

[38] R. N. Manchester J. Sarkissian A. G. Lyne N. D'Amico, A. Possenti and F. Camilo. An eclipsing millisecond pulsar with a possible main-sequence companion in ngc 6397. *The Astrophysical Journal*, 561:L89–L92, 2001.

[39] B. Warner P. A. Woudt and M. L. Pretorius. High-speed photometry of faint cataclysmic variables - iv. v356 aql, aqr1, first j1023+0038, h-alpha 0242-2802, gi mon, ao oct, v972 oph, sdss 0155+00, sdss 0233+00, sdss 1240-01, sdss 1556-00, sdss 2050-05, fh ser. *MNRAS*, 351:1015–1025, 2004.

[40] J. Takata C. Y. Hui L. C. C. Lin R. H. H. Huang, A. K. H. Kong and K. S. Cheng. X-ray studies of the black widow pulsar psr b1957+20. *arXive pre-print*, 2012.

[41] V. Radhakrishnan and D. J. Cooke. Magnetic poles and the polarization structure of pulsar radiation. *Astrophysical Letters*, 3:225, 1969.

[42] Mallory S.E. Roberts. New black widows and redbacks in the galactic field. *arXive pre-print*, 2011.

[43] George B. Rybicki and Alan P. Lightman. *Radiative Processes in Astrophysics*. Wiley, 1979.

[44] S. Mereghetti L. Stella S. Campana, M. Colpi and M. Tavani. The neutron stars of soft x-ray transient. *Astronomy and Astrophysics*, 8:279, 1998.

[45] S. L. Shapiro and S. A. Teukolsky. *Black Holes, White Dwarfs and Neutron Stars: The Physics of Compact Objects*. Wiley-VCH, 1983.

[46] J. Jeff Hester Shrinivas R. Kulkarni. Discovery of a nebula around psr 1957+20. *Nature*, 335:801–803, 1988.

[47] I. H. Stairs. Pulsars in binary systems: Probing binary stellar evolution and general relativity. *Science*, 304:547–552, April 2004.

[48] P. Szkody. *The Astrophysical Journal*, 126:1499, 2003.

[49] N. Langer T. M. Tauris and M. Kramer. Formation of millisecond pulsars with co white dwarf companions – ii. accretion, spin-up, true ages and comparison to msps with he white dwarf companions. *MNRAS*, 2012.

[50] J. R. Thorstensen and E. Armstrong. Is first j102347.6+003841 really a cataclysmic binary? *The Astronomical Journal*, 130:759–766, 2005.

[51] V. N. Tsytovich. *Theory of Turbulent Plasma*. : Consultants Bureau, 1977.

[52] Nicola Urbinati. Meccanismi di eclisse di pulsar al millisecondo in sistemi binari: il caso di psr j1740-5340. Master's thesis, Università degli Studi di Bologna, 2001.

[53] D. Khangulyan V. Bosch-Ramon, M.V. Barkov and M. Perucho. Simulations of stellar/pulsar-wind interaction along one full orbit. *Astronomy and Astrophysics*, 2012.

[54] T. M. Tauris V. M. Kaspi and R. N. Manchester. On the wind from the small magellanic cloud b1 v companion to psr j0045-7319. *The Astrophysical Journal*, 459:717–720, March 1996.

[55] E. Yu. Osminkin V. M. Lipunov, S. N. Nazin and M. E. Prokhorov. Binary radiopulsar with optical companion. *Astronomy and Astrophysics*, 282:61–72, 1993.

[56] E. P. J. van den Heuvel. *Physics of Relativistic Objects in Compact Binaries: From Birth to Coalescence*. Springer, 2008.

[57] Mario Vietri. *Astrofisica delle Alte Energie*. Bollati Boringhieri, 2006.

[58] F. P. Wilkin. Exact analytic solutions for stellar wind bow shocks. *The Astrophysical Journal*, 459:L31–L34, 1996.

[59] J. R. Thorstensen V. M. Kaspi D. R. Lorimer I. Stairs Z. Wang, A. M. Archibald and S. M. Ransom. Sdss j102347.6+003841: A millisecond radio pulsar binary that had a hot disk during 2000-2001. *The Astrophysical Journal*, 703:2017–2023, 2009.